

# 学位論文

A Frequency-Division Multiplexing Readout System  
for Large-Format TES X-Ray Microcalorimeter Arrays  
towards Future Space Missions

(将来の宇宙ミッションをめざした  
TES型X線マイクロカロリメータ大規模アレイの  
周波数分割型信号多重化システム)

平成26年12月博士(理学)申請  
東京大学大学院理学系研究科  
物理学専攻 酒井 和広



# Acknowledgments

My 5 years in ISAS/JAXA just flew by. I have been supported by my people during the years. Without their help, I would never be able to finish my thesis.

I would like to express special appreciation to my advisor Professor Kazuhisa Mitsuda. He has patiently guided me throughout the journey of my thesis with his depth and breadth of knowledge. It has been a great pleasure and honor to learn from him. I would also thank Professor Noriko Y. Yamasaki for her support and encouragement. In addition, a thank you to Dr. Yoh Takei for enormous valuable discussions.

I would like to thank my thesis committee members, Professor Masatake Ohashi, Professor Kazuaki Kuroda, Professor Takao Nakagawa, Professor Yasuhiro Iye, and Professor Yasushi Sutoh for valuable comments and suggestions that improved the contents of this thesis dramatically.

Dr. Toshiyuki Miyazaki taught me all about SQUID, and those SQUID were fabricated in the CRAVITY at AIST with a great help from Dr. Mutsuo Hidaka, Dr. Shuichi Nagasawa, and Dr. Satoshi Kohjiro.

If I should mention a second author, Ryo Yamamoto would definitely be the one. He helped me to conduct the entire research in this thesis. Without his help, I could never be able to finish my thesis. I should also mention Akira Chiba, who measured many SQUID for these two years. The TES used in this thesis was fabricated by Kenichiro Nagayoshi, Tasuku Hayashi and Haruka Muramatsu. A special thanks to my fellow labmates: Dr. Norio Sekiya, Takahiro Kikuchi, Yuki Tsurugasaki, and Masatoshi Hoshino. I would also like to thank Secretary Akiko Yokoyama for all about the daily life in the lab.

Last but not the least, I would like to thank my family. Words can not express how grateful I am to my mother-in-law and father-in-law for their great support. I am also grateful to my mother, father, and brother. Finally, and most importantly, I would like to thank my lovely wife Tomoko. Without her support, encouragement, patience, and enduring love, this journey would not have been possible.

This work was supported by Grant-in-Aid for JSPS Fellows (2611200).



# Abstract

In future space missions X-ray transition edge sensor (TES) microcalorimeters are promising detectors achieving high energy resolution and high spatial resolution at the same time. It is however still difficult to realize a large format array on account of the absence of a well-established multiplexing readout technique, which is essential to suppress the heat input to a cryogenic stage with a limited cooling power by reducing the required number of wires. In this thesis, we developed the new frequency-division multiplexing (FDM) readout system aimed to realize the 400-pixel TES microcalorimeter array for the DIOS mission, as well as large format arrays with more than a thousand of TES for future space missions like ATHENA. The developed system consists of the low-power superconducting quantum interference device (SQUID), the digital flux-locked loop (FLL) electronics, and the analog front-end to bridge the SQUID and the FLL electronics. The developed SQUID has very small heat dissipation and can be placed at the same cryogenic stage as TES. We also developed a multi-input FDM SQUID chip using the low-power SQUID. With the digital FLL electronics that provides the high-density signal multiplexing, the cryogenic stage becomes significantly simple even for multiplexing hundreds of TES. The digital electronics can multiplex more than 16 signals without deteriorating the required signal-to-noise ratio (SNR). Moreover, it properly reduces the data rate and keeps the required system data transfer rate to a practical number even for thousands of signal multiplexing. Using the developed readout system, we performed a TES readout experiment, and succeeded to multiplex four TES with the single-staged cryogenic setup for the first time. Although two new issues, an excess noise and a crosstalk, have been clarified during the experiment, the contribution of the developed readout system to the energy resolution is already small enough to realize the TES array for the DIOS mission, and the feasibility of the large format TES array with the developed readout system has therefore been demonstrated.



# Contents

Acknowledgment	i
Abstract	iii
Chapter 1 Introduction	1
Chapter 2 Review	3
2.1 Missing Baryon Problem and Next Generation X-ray Space Missions . . . . .	3
2.1.1 Mission Baryon Problem . . . . .	3
2.1.2 Next Generation X-ray Space Missions . . . . .	4
X-ray Microcalorimeters . . . . .	4
DIOS Mission . . . . .	5
ATHENA Mission . . . . .	5
2.2 X-ray Microcalorimeters . . . . .	7
2.2.1 Principles of X-ray Microcalorimeters . . . . .	7
2.2.2 Transition Edge Sensors . . . . .	8
2.2.3 Electrothermal Feedback (ETF) . . . . .	9
General Formalization of ETF and Current Responsivity . . . . .	11
2.2.4 Intrinsic Noises . . . . .	14
2.2.5 Energy Resolution . . . . .	17
2.2.6 Optimal Filtering . . . . .	17
2.3 Superconducting Quantum Interference Devices . . . . .	20
2.3.1 Josephson Junctions . . . . .	20
2.3.2 RCSJ Model . . . . .	20
2.3.3 Johnson-Nyquist Noise . . . . .	22
2.3.4 dc SQUID . . . . .	23
2.3.5 Principles of dc SQUID . . . . .	24
2.3.6 Johnson-Nyquist Noise . . . . .	28
2.3.7 Optimization . . . . .	28
2.3.8 Numerical Analysis and Approximate Solutions for dc SQUID . . . . .	29
2.3.9 TES Readout with SQUID . . . . .	30
2.3.10 Flux-Locked Loop . . . . .	31
2.3.11 SQUID Array . . . . .	31
2.3.12 Joule Heating . . . . .	33
2.3.13 Bandwidth . . . . .	33
2.3.14 SQUID Noise Contribution to Energy Resolution . . . . .	33
2.3.15 SQUID Multiplexing . . . . .	34

	Time-Division Multiplexing . . . . .	34
	Code-Division Multiplexing . . . . .	35
	Frequency-Division Multiplexing . . . . .	35
	Comparison of Multiplexing Types . . . . .	36
<b>Chapter 3</b>	<b>Development of Low-Power SQUIDs</b>	<b>37</b>
3.1	Requirements for SQUIDs . . . . .	37
3.2	Parameter Optimizations and SQUID Designs . . . . .	38
	3.2.1 Parameter Optimizations . . . . .	38
	3.2.2 SQUID Designs . . . . .	39
	3.2.3 Multi-Input Current-Summing SQUID . . . . .	39
3.3	Measurements . . . . .	42
	3.3.1 Setups . . . . .	46
	3.3.2 $\Phi$ - $V$ Measurements . . . . .	47
	3.3.3 Noise Measurements . . . . .	49
	3.3.4 Filter Measurements . . . . .	50
	3.3.5 Working Points . . . . .	51
	3.3.6 Measurement Summary . . . . .	51
3.4	Summary . . . . .	51
<b>Chapter 4</b>	<b>Development of Digital Electronics for Frequency-Division Multiplexing</b>	<b>53</b>
4.1	Principles of Frequency-Division Multiplexing and Baseband Feedback . . . . .	53
	4.1.1 Preparation . . . . .	53
	4.1.2 Principles of AC-biased Microcalorimeter . . . . .	53
	4.1.3 Noise of AC-biased microcalorimeters . . . . .	57
	4.1.4 Principles of Baseband Feedback . . . . .	59
4.2	Requirements for Digital Electronics . . . . .	60
4.3	System Overview . . . . .	61
	4.3.1 ADC/DAC Board . . . . .	61
	4.3.2 FPGA Board . . . . .	61
4.4	Design and Implementation . . . . .	62
	4.4.1 Core Logic . . . . .	62
	I/Q Demodulator and Modulator . . . . .	62
	CIC Decimator and Interpolator . . . . .	63
	Discrete-Time Integrator and Gain Control . . . . .	64
	CORDIC . . . . .	65
	3rd-order LPF for Baseband . . . . .	65
	Trigger, Baseband Decimation and Waveform Extract . . . . .	66
	4.4.2 System Overall Gain . . . . .	68
	4.4.3 Interface . . . . .	69
	4.4.4 Resource Utilization . . . . .	70
4.5	Loopback Test . . . . .	73
	4.5.1 SNR Evaluation . . . . .	73
	4.5.2 Loopgain Evaluation . . . . .	74
	4.5.3 Crosstalk Evaluation . . . . .	75

4.6	Development of Analog Front-End . . . . .	76
4.6.1	Requirements for Analog Front-End . . . . .	76
4.6.2	Design and Implementation . . . . .	77
	Low-Noise Amp (LNA) . . . . .	78
	V/I Converter . . . . .	78
	Other Features . . . . .	79
	PCB Layout . . . . .	79
4.6.3	Measurements . . . . .	79
4.7	Summary . . . . .	81
Chapter 5	Experiment of TES Readout . . . . .	83
5.1	Objective . . . . .	83
5.2	Setups . . . . .	83
5.2.1	Refrigerator . . . . .	83
5.2.2	Cryogenic Stage . . . . .	84
	TES . . . . .	84
	SQUID and LC Filter . . . . .	84
	X-Ray Source . . . . .	85
	Mounting to the Refrigerator . . . . .	85
5.2.3	Room-Temperature Front-End . . . . .	85
5.2.4	SQUID Setup . . . . .	85
5.3	Results . . . . .	87
5.3.1	LC Filter Characteristics . . . . .	87
5.3.2	$R$ - $T$ Measurements . . . . .	88
5.3.3	Non-multiplexing $I$ - $V$ Measurements . . . . .	89
5.3.4	Non-multiplexing Pulse Collections . . . . .	90
5.3.5	Simultaneous $I$ - $V$ Measurements . . . . .	92
5.3.6	Simultaneous Pulse Collections . . . . .	92
5.4	Summary . . . . .	94
Chapter 6	Discussion . . . . .	97
6.1	Energy Resolution Degradation due to Readout System . . . . .	97
6.2	Excess Noise . . . . .	100
6.3	Crosstalks . . . . .	100
6.4	Summary . . . . .	102
Chapter 7	Summary . . . . .	103
7.1	Summary . . . . .	103
A	CRAVITY . . . . .	105
A.1	AIST Nb Standard Process (STD3) . . . . .	105
B	Hardware Registers and Addresses for Digital Electronics . . . . .	109
C	Design of Analog Front-End . . . . .	113



# List of Figures

2.1	The ion fraction distributions represented as column densities for a total gas column of $10^{19} \text{ cm}^{-2}$ and metallicities of $0.1 Z_{\odot}$ . . . . .	3
2.2	The simulated X-ray spectra of an optically-thin thermal plasma with $kT = 3 \text{ keV}$ for various energy resolutions . . . . .	4
2.3	The comparison of $S\Omega$ for DIOS and other space missions . . . . .	5
2.4	A schematic view of an X-ray microcalorimeter . . . . .	7
2.5	Transition edge . . . . .	8
2.6	Constant voltage biasing with a shunt resistor . . . . .	9
2.7	Electrothermal feedback . . . . .	12
2.8	Electrothermal feedback with intrinsic noises . . . . .	14
2.9	Noise current power spectral density . . . . .	16
2.10	RCSJ model . . . . .	20
2.11	Calculated $I-V$ characteristic for various values of $\beta_C$ and the return critical current vs. $\beta_C$ . . . . .	22
2.12	Calculated $I-V$ characteristic for various values of $\Gamma$ for negligible capacitance and finite capacitance . . . . .	23
2.13	The dc SQUID . . . . .	23
2.14	The integral path on the superconducting ring of dc SQUID . . . . .	24
2.15	Critical current of the dc SQUID vs. applied magnetic flux for various values of $\beta_L$ and the modulation depth vs. $\beta_L$ . . . . .	26
2.16	$\Phi-V$ characteristics for $\beta_C = 0$ and $\beta_C = 1$ . . . . .	26
2.17	$\beta_L$ optimization . . . . .	29
2.18	TES readout using SQUID . . . . .	30
2.19	The schematic diagram of Flux-Locked Loop (FLL) . . . . .	31
2.20	The TES readout using the SQUID array . . . . .	32
2.21	The schematic diagram of the SQUID TDM architecture . . . . .	34
2.22	Signal summing methods in FDM . . . . .	35
3.1	The design of the junction and shunt resistor part . . . . .	39
3.2	The design of ISAS-G . . . . .	40
3.3	The design of ISAS-G15 . . . . .	41
3.4	The design of the ISAS-G15 chip . . . . .	42
3.5	The designs of the 4-input ISAS-G15 chip with inductors and the 4-input extension chip with inductors . . . . .	43
3.6	Equivalent circuits for the 4-input SQUID chip with inductors and the 4-input extension chip with inductors . . . . .	43
3.7	The designs of the 4-input ISAS-G15 chip with built-in LC filters and the 4-input extension chip . . . . .	44

3.8	Equivalent circuits for the 4-input SQUID chip with built-in LC filters and the 4-input extension chip . . . . .	44
3.9	Photomicrographs of the fabricated ISAS-G15 . . . . .	45
3.10	Photomicrographs of the 4-input ISAS-G15 with inductors . . . . .	45
3.11	Photomicrographs of the 4-input ISAS-G15 with inductors and capacitors . . . . .	46
3.12	Photomicrographs of the 4-input extension chips . . . . .	46
3.13	Experimental setups for $\Phi$ - $V$ measurements and noise measurements . . . . .	47
3.14	4 K probe . . . . .	47
3.15	The stage of the 4 K probe . . . . .	47
3.16	The $\Phi$ - $V$ characteristics of ISAS-G15 for various values of bias current . . . . .	48
3.17	$\partial V/\partial\Phi_{in}$ and the dynamic resistance in $0-0.5\Phi_0$ of ISAS-G15 for various values of bias current . . . . .	48
3.18	Equivalent input current noises of ISAS-G15 in the open loop for various $\Phi_{in}$ offsets . . . . .	49
3.19	The measured LC bandpass filter characteristic at 4K . . . . .	50
4.1	TES biasing . . . . .	54
4.2	The signal power spectrum of DC-biased TES . . . . .	55
4.3	The signal power spectrum of AC-biased TES . . . . .	55
4.4	The demodulated signal power spectrum using the phase detection method . . . . .	56
4.5	Equivalent noise circuit for AC-biased microcalorimeter . . . . .	57
4.6	The schematic diagram of the baseband feedback architecture . . . . .	59
4.7	Digital BBFB diagram . . . . .	62
4.8	CIC Decimator . . . . .	63
4.9	Frequency responses of 3rd-order 1/64 CIC decimation filter . . . . .	64
4.10	Frequency responses of discrete-time integrator for various gains . . . . .	65
4.11	Biquad filter implementations . . . . .	65
4.12	Frequency responses of biquad low-pass filter for various fraction bits . . . . .	66
4.13	Frequency response of 3rd-order low-pass filter . . . . .	67
4.14	Dispersion of pulse heights (PHA) vs. sampling rates for various pulse rise times . . . . .	68
4.15	Overall gain in the digital electronics for various gain parameters . . . . .	69
4.16	SoC design with LEON3 microprocessor . . . . .	70
4.17	The BBFB controller attached to the APB . . . . .	70
4.18	Application stack on the SoC . . . . .	71
4.19	TES Workbench . . . . .	72
4.20	Resource utilization for various number of channels . . . . .	72
4.21	Loopback mode . . . . .	73
4.22	Dummy pulse used to modulate in the loopback test . . . . .	73
4.23	The obtained signal-to-noise ratio in the loopback test . . . . .	74
4.24	The measured and theoretical frequency responses in the single channel loopback mode for various gain parameters . . . . .	74
4.25	The averaged pulses and the averaged noises for various spacing frequencies . . . . .	75
4.26	The averaged pulses and the averaged noises for various gain parameters . . . . .	76
4.27	A typical experimental setup for a TES multiplexed readout . . . . .	76
4.28	The circuit schematic of typical FET differential amplifier . . . . .	77
4.29	The circuit schematic of the V/I converter based on the op-amp differential amplifier . . . . .	78
4.30	The analog front-end measurement setup . . . . .	79

4.31	The measured gain and phase of the analog front-end . . . . .	80
4.32	The measured noises for various configurations . . . . .	80
5.1	The dry $^3\text{He}$ - $^4\text{He}$ dilution reffridgerator . . . . .	83
5.2	The cryostage setup . . . . .	84
5.3	The equivalent circuit for the cryostage setup . . . . .	84
5.4	$8 \times 8$ TES array . . . . .	85
5.5	Mouting to the refrigerator . . . . .	86
5.6	The analog front-end directly mounted to the refrigerator port . . . . .	86
5.7	The $\Phi$ - $V$ curve ( $I_{\text{SB}} = 17 \mu\text{A}$ ) at 200 mK and the operating point during the measurements . . . . .	87
5.8	The LC filter characteristics at 150 mK (TES super) and 250 mK (TES normal) . . . . .	87
5.9	The measured $R$ - $T$ characteristics and the TES current during the $R$ - $T$ measurement . . . . .	88
5.10	The TES shunt resistor adjusted $R$ - $T$ and the TES bias level adjusted $R$ - $T$ . . . . .	89
5.11	The measured $I$ - $V$ characteristics of each channel in non-multiplexing . . . . .	90
5.12	The averaged pulses in each channel at 150 mK for various TES bias currents . . . . .	91
5.13	The averaged pulses in channel 1 at 180 mK and 190 mK for various TES bias currents . . . . .	92
5.14	The pulse collection result in channel 1 at 180 mK . . . . .	93
5.15	The simultaneously measured $I$ - $V$ characteristics multiplexing all channels . . . . .	94
5.16	The averaged pulses in each channel at 170 mK for various TES bias currents . . . . .	95
5.17	The 4-channel simultaneous pulse collection result in channel 1 at 170 mK . . . . .	96
6.1	A typical experimental setup for a FDM TES readout . . . . .	97
6.2	The current noise due to the readout system and the contribution to energy resolution for various number of multiplexing channels . . . . .	99
6.3	The contribution of the readout system to the energy resolution when the system noise is reduced by half . . . . .	99
6.4	The current noise when the TES is in the normal state at 240 mK . . . . .	100
6.5	The current noises for various TES states . . . . .	101
6.6	The observed crosstalks . . . . .	101
A.1	The device structure of SRL Nb Standard Process (STD3) . . . . .	105
B.1	The hardware registers and addresses for configuration parameters of the digital electronics (part 1 of 2) . . . . .	110
B.2	The hardware registers and addresses for configuration parameters of the digital electronics (part 2 of 2) . . . . .	111
C.1	The circuit schematic of BBFB analog front-end . . . . .	114
C.2	Full-scale PCB layouts of BBFB analog front-end . . . . .	115



# List of Tables

3.1	Design targets of low-power SQUIDs	37
3.2	Design parameters of ISAS-A10, ISAS-B10, ISAS-C10, and new ISAS-G15	38
3.3	Design targets and actual results of ISAS-A10, ISAS-B10 and ISAS-C10	38
3.4	Inductances, capacitances and resonance frequencies of the LC filters on the 4-input current-summing SQUID and the 4-input extension chips	40
3.5	Noise characteristics of ISAS-G15 at 4 K	49
3.6	The measured resonance frequencies of the LC filters on the 4-input current-summing SQUID and the 4-input extension chips	50
3.7	ISAS-G15 working point	51
3.8	Design targets and measurement results of ISAS-G15	51
4.1	Requirements for digital electronics	60
4.2	FMC150 specifications	61
4.3	Baseband LPF design parameters	66
4.4	Gains at each FLL stage	69
4.5	Excerpted hardware configuration parameters	71
4.6	The FPGA resource usage by the LEON3 SoC	71
4.7	FMC150 delay caused by the internal interpolation	74
4.8	Requirements for analog front-end	77
5.1	LC filter setups	84
5.2	The measured resonance frequencies of the LC filter	88
5.3	The obtained correction factors for each channel	89
5.4	The obtained energy resolutions in non-multiplexing pulse collections	91
5.5	The obtained energy resolutions in multiplexing pulse collections for all the channels	92
6.1	A readout system noise estimation	97
A.1	The layer structure of SRL Nb Standard Process (STD3)	106
A.2	STD3 alignment margins	107
A.3	STD3 minimum spacing between layers	107
A.4	STD3 minimum line width	107



# Nomenclature

ADR	Adiabatic Demagnetization Refrigerator
ATHENA	Advanced Telescope for High ENergy Astrophysics
BBFB	Baseband Feedback
CDM	Code-Division Multiplexing
CIC	Cascaded Integrator-Comb
CORDIC	Coordinate Rotation Digital Computer
DDS	Direct Digital Synthesizer
DIOS	Diffuse Intergalactic Oxygen Surveyor
ENOB	Effective Number of Bits
FDM	Frequency-Division Multiplexing
FLL	Flux-Locked Loop
FWHM	Full-Width at Half Maximum
GM	Gifford-McMahon
IIR	Infinite Impulse Response
LSB	Least Significant Bit
MACC	Multiply Accumulator
MSB	Most Significant Bit
NEP	Noise Equivalent Power
PHA	Pulse Height
RCSJ	Resistively- and Capacitively-Shunted Junction
SFDR	Spurious Free Dynamic Range
SNR	Signal-to-Noise Ratio
SQUID	Superconducting Quantum Interference Device
SXS	Soft X-ray Spectrometer
TDM	Time-Division Multiplexing
TES	Transition Edge Sensor
WHIM	Warm-Hot Intergalactic Medium



# Chapter 1

## Introduction

In future space missions X-ray transition-edge sensor (TES) microcalorimeters are most promising detectors achieving high spectral resolution and high spatial resolution *at the same time*. The theoretical energy resolution of TES can be 2 eV full-width at half maximum (FWHM) at 5.9 keV (Mn  $K\alpha$ ) or better, which is an enhancement by more than a order of magnitude compared with ordinary X-ray CCD image sensors. Microcalorimeters with semiconductor thermistors, such as the Soft X-ray Spectrometer (SXS) aboard Astro-H, a next generation JAXA X-ray satellite, also provide the capability of high energy resolution ( $\leq 7$  eV FWHM @ 5.9 keV) yet the capability of high spatial resolution on account of a difficulty of multiplexing because of high-impedance inputs and parasitic capacitances of thermistors. On the other hand, a TES has a low input impedance, and is well suited for signal multiplexing that is indispensable for high spatial resolution, or a large format array, being placed at a cryogenic stage below 100 mK.

Frequency-division multiplexing (FDM) is a key technique among other methods, such as time-division multiplexing (TDM) and code-division multiplexing (CDM), for TES signal multiplexing in space missions, and is largely adopted to readout TES bolometers for not only space missions such as SAFARI (SpicA FAR-infrared Instrument) in SPICA but also ground missions such as the multi-color TES bolometer camera in Atacama Sub-millimeter Telescope Experiment (ASTE). It is, however, still transient and has not yet well-established for X-ray TES microcalorimeters, since the signal bandwidth of X-ray TES is much larger than that of TES bolometers. So far our research group and a research group at SRON have succeeded to multiplex signals from X-ray TES microcalorimeters.

In this thesis, we freshly developed an entire readout system including a low-power superconducting quantum interference device (SQUID), a low-noise preamplifier, and a high-frequency flux-locked loop (FLL) electronics, for large-format TES X-ray microcalorimeter arrays toward the Diffuse Intergalactic Oxygen Surveyor (DIOS) space mission as well as future space missions like ATHENA, the largest X-ray observatory proposed by the European Space Agency (ESA). Those missions are planned to carry large-format TES arrays (400 pixels for DIOS, and 3,840 pixels for ATHENA), and the FDM is a must in successful science missions. Unlike the multi-staged cryogenic setups that other groups adopt, our cryogenic stage is the simple single-staged setup that all the cryoelectronics including TES and SQUIDs are placed at the very same stage. It reduces complexities of the cryogenic stage, making the required resource, the lead-time, the chance of error, and even the cost also reduced greatly. To achieve it, we developed the low-power SQUID optimized for the FDM readout, which is described in Chapter 3, and the high-frequency digital FLL electronics for FDM including the analog front-end optimized for our low-power SQUID and the digital electronics, which is described in Chapter 4. Using the developed system, we succeeded to multiplex and readout TES signals, which is described in Chapter 5. We discuss the issues clarified in the multiplexing experiment in Chapter 6, and we finally summarize and conclude our system in Chapter 7.



## Chapter 2

### Review

#### 2.1 Missing Baryon Problem and Next Generation X-ray Space Missions

##### 2.1.1 Missing Baryon Problem

The observation of the cosmic microwave background by WMAP and Planck has revealed the Universe’s precise ingredients. Under the  $\Lambda$ CDM model, atoms, or baryons, is only about 5% of the Universe. So far we have seen some of those baryons in the form of stars, galaxies, clusters of galaxies, and intercluster medium in various wavelengths. However, we have identified only 50% of them [e.g. 30]. The other half has not yet observed in any wavelengths. This is called “missing baryon problem.”

According to the cosmological hydrodynamic simulation by Cen and Ostriker [3], it is indicated that some of missing baryons are distributed as a rarefied gas in a temperature of  $10^5$ – $10^7$  K along the filaments interconnecting clusters of galaxies. It is called the warm-hot intergalactic medium (WHIM).

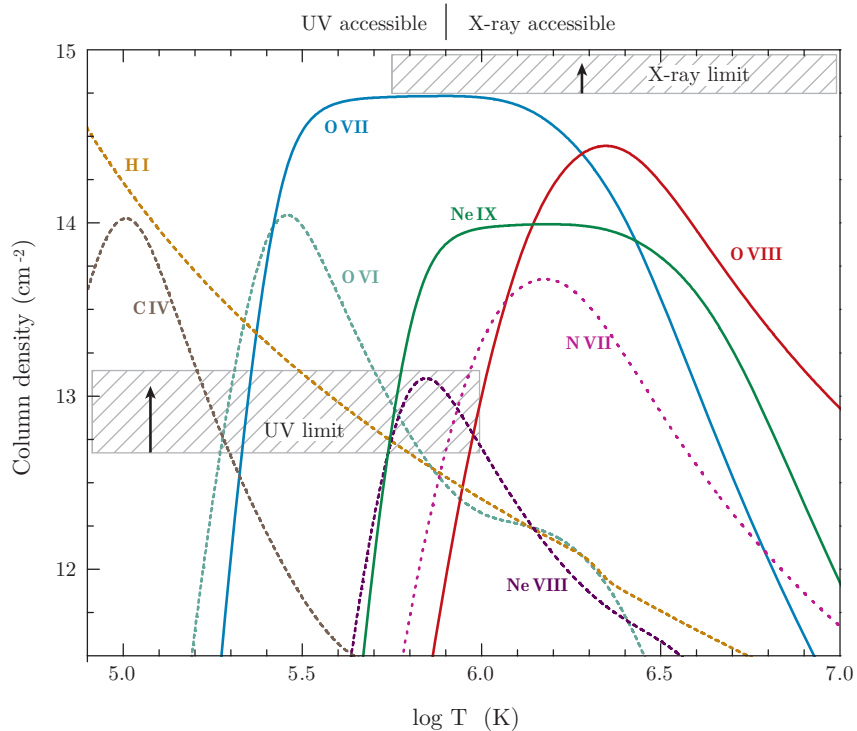


Fig. 2.1 The ion fraction distributions represented as column densities for a total gas column of  $10^{19} \text{ cm}^{-2}$  and metallicities of  $0.1 Z_{\odot}$ . Adapted from Figure 5 of Bregman [2].

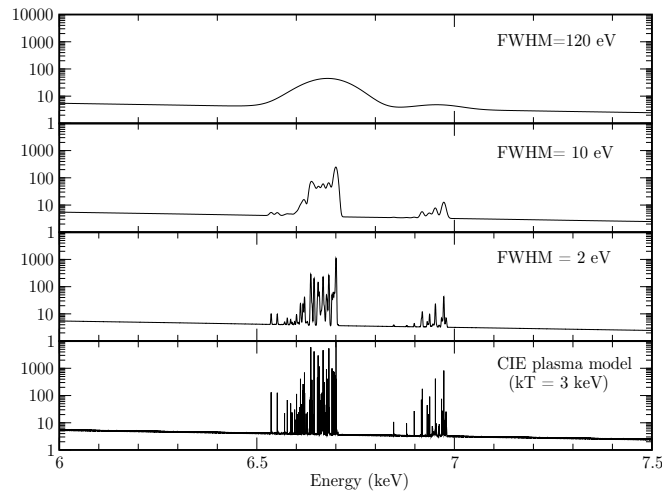


Fig. 2.2 The simulated X-ray spectra of an optically-thin thermal plasma with  $kT = 3$  keV for various energy resolutions

As we see in Figure 2.1, the fraction of highly ionized oxygen is the largest component in the  $10^5$ – $10^7$  K gas, which makes the emission/absorption lines of highly ionized oxygen, OVI, OVII and OVIII, dominated in the spectrum. Consequently, the WHIM has been searched in the UV and X-ray bands. To observe the absorption lines of OVI Ly $\alpha$ , we need a bright X-ray point source at the back. This makes the observable region very limited. On the other hand, the X-ray detectors in orbits are lack of the energy resolution and field of view to observe the oxygen emission lines from the WHIM. To solve the mystery of the missing baryon, a telescope with a better spatial resolution and a detector with a better energy resolution are demanded.

### 2.1.2 Next Generation X-ray Space Missions

#### X-ray Microcalorimeters

The X-ray microcalorimeter is a detector to determine the energy of an incident X-ray photon by precisely measuring a temperature increase of an absorber (or the detector itself) hit by the photon. Being placed at a cryogenic stage below 100 mK, it can achieve a very high energy resolution ( $\Delta E < 10$  eV). It is the only detector that has a sufficient energy resolution for the most important energy range of the iron  $K\alpha$ . X-ray CCD detectors are simply lack of the required energy resolution, and energy-dispersive X-ray spectrometers, such as gratings, are not suited for diffuse X-ray sources. For this reason, they are promising detectors in future X-ray space missions.

The microcalorimeter is, in other words, a thermometer, and semiconductor thermistors have been used, but they are not suited for signal multiplexing due to the high impedance input and the high input capacitance, making it difficult to realize a large-format microcalorimeter array. The transition-edge sensor is another form of thermometer that has a higher sensitivity and a very small input impedance, and recently it has been intensively studied towards the realization of the large-format microcalorimeter array. In principle, TES can achieve  $\Delta E < 2$  eV for the iron  $K\alpha$ , which makes it possible to observe the detailed fine structures of the iron  $K\alpha$  line (Figure 2.2). In our joint research group of ISAS/JAXA and Tokyo Metropolitan University, we have achieved the energy resolution of 2.8 eV FWHM for 5.9 keV X-rays [1].

For energy resolution we are achieving the requirement, yet a method to readout thousands of TES is still transient. The Soft X-ray Spectrometer of Astro-H is a  $6 \times 6$  X-ray microcalorimeter with thermistors, and each pixel is read out individually. However, it is impossible to readout thousands of TES individually on account of the heat flow to the cryogenic stage through the wires. The TES signals therefore need to be multiplexed to

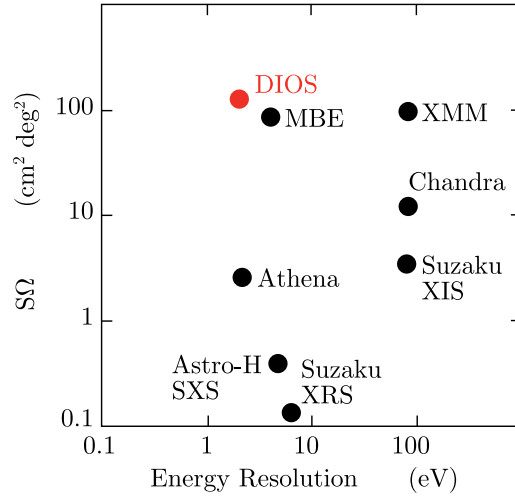


Fig. 2.3 The comparison of  $S\Omega$  for DIOS and other space missions

reduce the required number of wires. The frequency-division multiplexing will be used to multiplex TES signals in orbits, but the method has not been well-established yet.

#### DIOS Mission

DIOS, the Diffuse Intergalactic Oxygen Surveyor, is a small class science satellite, proposed by the joint research group of Tokyo Metropolitan University, Nagoya University, ISAS/JAXA and the DIOS working group, aimed at unveiling the mystery of missing baryons by the direct observation of WHIM [e.g. 25]. It has been developed for a launch around 2020. It is aimed to directly detect the WHIM as well as to map the distribution of  $10^5$ – $10^7$  K WHIM within  $0 < z < 0.3$  by observing the oxygen lines, OVII (561, 568 and 574 eV) and OVIII (653 eV), precisely. It is also aimed to reveal the chemical evolution in the intergalactic medium, the gas heating mechanism, and the gas dynamics from the emission/absorption line ratio of OVII and OVIII as well as the width and fine structure of the lines.

According to the simulation result by Yoshikawa et al. [37], 20–30% of all the baryons can be detectable if a detector has a sensitivity of  $\sim 10^{11}$  erg<sup>-1</sup> cm<sup>-2</sup> ster<sup>-1</sup> to emission lines. It means that the required  $S\Omega$ , which is the detector effective area  $\times$  the field of view, is  $\sim 100$  cm<sup>2</sup> deg<sup>2</sup> assuming the  $\sim 1$  Msec exposure. Figure 2.3 shows the comparison of  $S\Omega$  of DIOS with other space missions. Although it is a small class satellite, it has the large  $S\Omega$  ( $\sim 150$  cm<sup>2</sup> deg<sup>2</sup>). Moreover, with the excellent energy resolution it outperforms Suzaku in the sensitivity to the diffuse X-ray emission by more than 40 times.

To achieve the science mission, the use of a TES microcalorimeter array as the detector is crucial. The required energy resolution is  $\Delta E < 2$  eV @ 2 keV, which makes TES is the only option. DIOS is planned to carry a 256- to 400-pixel TES array covering an area of  $\sim 1$  cm<sup>2</sup>. The corresponding field of view is  $\sim 50$  arcmin. To cool the TES array and the cold front-end electronics to 50 mK, a 2-stage adiabatic demagnetization refrigerator, which is precooled by a 2-stage Stirling cooler and a <sup>3</sup>He Joule-Thomson cooler, is used. They are all cryogen-free, thus the observing life in the orbit is unlimited.

#### ATHENA Mission

ATHENA, the Advanced Telescope for High ENergy Astrophysics, is a X-ray science satellite proposed by European Space Agency, scheduled for launch in 2028, and is another future satellite mission planning to use a TES array for its main detector. Two main science themes of ATHENA are the hot universe and the energetic universe. The former is to answer the question of “how does ordinary matter assemble into the large scale structures that

we see today,” and the latter is to answer the question of “how do black holes grow and influence the Universe [24].” The X-ray Integral Field Unit (X-IFU), one of the detectors aboard ATHENA, is a large-format X-ray TES microcalorimeter array, which is the key detector for the proposed science [e.g. 26].

The X-IFU covers the wide energy range of 0.2–12 keV with the excellent energy resolution of 2.5eV ( $E < 7$  keV). The size of array is 3,840, which will be multiplexed for 40 channels each, using the FDM [e.g. 27].

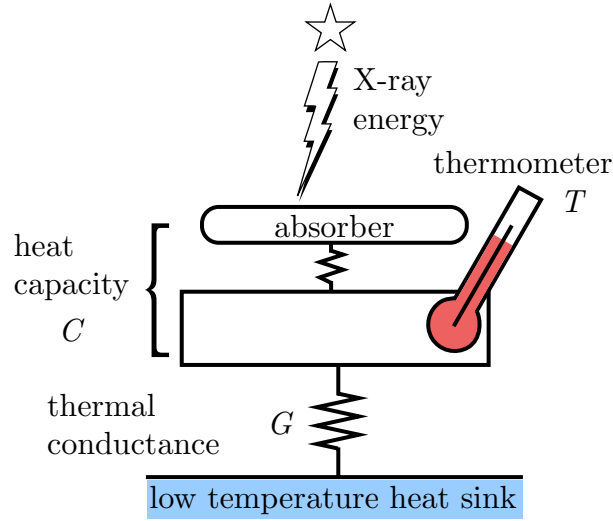


Fig. 2.4 A schematic view of an X-ray microcalorimeter

## 2.2 X-ray Microcalorimeters

### 2.2.1 Principles of X-ray Microcalorimeters

X-ray microcalorimeters are detectors to determine the energy of an incident X-ray photon by measuring the temperature rise caused by the absorption of the photon into an absorber. A simple microcalorimeter consists of three parts: an absorber to absorb X-ray photons and convert to heat, a thermometer to measure the temperature rise of the absorber, and a thermal link to a heat sink to allow the absorbed heat to escape from the absorber (Figure 2.4). The temperature rise can be given by

$$\Delta T = \frac{E}{C}, \quad (2.1)$$

where  $E$  is the energy of incident X-ray photon, and  $C$  is the heat capacity of the detector. The heat converted from the energy in the absorber escapes to the heat sink, and the detector gradually returns back to the equilibrium point. This thermal response can be given by

$$C \frac{d\Delta T}{dt} = -G\Delta T, \quad (2.2)$$

where  $G$  is the thermal conductivity of the link to the sink. Therefore, the temperature of the detector falls exponentially with a time constant given by

$$\tau_0 = \frac{C}{G}. \quad (2.3)$$

The energy resolution of a X-ray microcalorimeter is limited by a thermal fluctuation in the detector. The number of phonons in a detector is  $N \sim CT/k_{\text{B}}T = C/k_{\text{B}}$ , and the thermal fluctuation of the detector will then be

$$\Delta U \sim \sqrt{N}k_{\text{B}}T = \sqrt{k_{\text{B}}T^2C}. \quad (2.4)$$

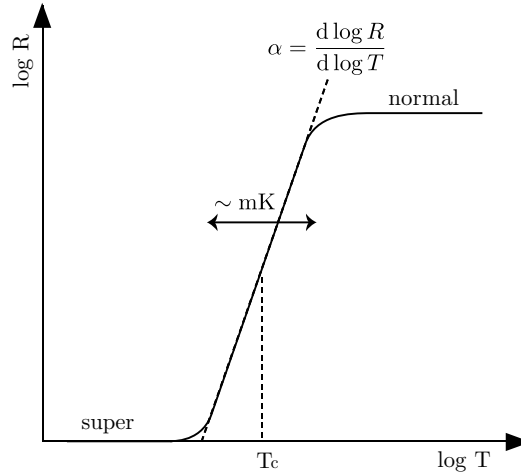


Fig. 2.5 Transition edge

Generally the intrinsic energy resolution of a X-ray microcalorimeter is

$$\Delta E_{\text{FWHM}} = 2.35\xi\sqrt{k_{\text{B}}T^2C}, \quad (2.5)$$

as we derive in Section 2.2.5.  $\xi$  is a parameter determined by a thermometer sensitivity and the like.

## 2.2.2 Transition Edge Sensors

Thermometers used for measuring the temperature rise of microcalorimeters are usually resistance thermometers. The sensitivity of thermometer  $\alpha$  is defined as

$$\alpha \equiv \frac{d \log R}{d \log T} = \frac{T}{R} \frac{dR}{dT}, \quad (2.6)$$

where  $T$  is temperature of the thermometer, and  $R$  is resistance of the thermometer. Historically, semiconductor thermistors have been used for microcalorimeters; however, the sensitivity of semiconductor thermistors may not be very high. For instance, a sensitivity of semiconductor thermistor used for Suzaku's X-ray microcalorimeter (XRS) is  $|\alpha| \sim 6$ .

A Transition Edge Sensor (TES) is a thermometer to archive a very high sensitivity (typically  $|\alpha| > 100$ ) utilizing a very steep resistivity change at a transition edge between its super conducting and normal state. The range of the transition is typically a few mK (Figure 2.5), which makes the sensitivity even higher than 1000. This high sensitivity allows a better energy resolution by more than a order of magnitude if compared with microcalorimeters using semiconductor thermistors. It also allows more selectability of absorber materials and shapes.

As the TES uses the transition edge, the operating temperature of TES microcalorimeter is limited to the transition temperature. By making a TES bilayer with a normal metal such as AU, the transition temperature can however be controlled using a proximity effect.

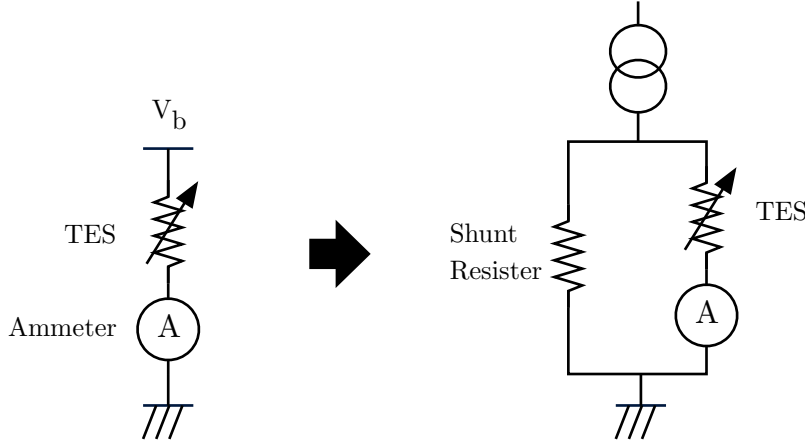


Fig. 2.6 Constant voltage biasing (left), and constant voltage biasing using a shunt resistor (right)

### 2.2.3 Electrothermal Feedback (ETF)

TES may have the very high sensitivity, but the temperature range that keeps the high sensitivity is quite small ( $\sim$  mK), and therefore the operating point needs to be kept within the transition edge. It can be realized by biasing TES with a constant voltage and applying a strong negative feedback, called an Electro-Thermal Feedback (ETF) [17].

Suppose a TES is biased with a constant voltage as shown in Figure 2.6 (left). The resistance of the TES rapidly increases as the temperature rises due to an incident photon, making the current flow as well as the Joule heat smaller under the voltage bias. The operating temperature is then kept in a stable. In reality constant voltage biasing is realized by using a shunt resistor inserted in parallel with the TES due to a non-negligible resistance in wirings between room temperature and a cryostage (Figure 2.6 right). For now we assume ideal constant voltage biasing.

Thermal conductivity is defined as

$$G \equiv dP/dT. \quad (2.7)$$

Generally thermal conductivity has a temperature dependence and  $G$  is represented as

$$G = G_0 T^{n-1}. \quad (2.8)$$

When a heat is carried by electrons, then  $n = 2$ , and when it is carried by phonons, then  $n = 4$ .

Let us consider a thermal conductivity between a TES and a heat sink (heat bath). A heat flow from the TES to the sink can be given by

$$P = \int_{T_{\text{bath}}}^T G dT = \frac{G_0}{n} (T^n - T_{\text{bath}}^n), \quad (2.9)$$

by integrating (2.7).

In thermal equilibrium the Joule heating of the TES,  $P_b \equiv V_b^2/R_0$ , and the heat flow from the TES to the sink is balanced, then gives

$$P_b = \frac{G_0}{n} (T_0^n - T_{\text{bath}}^n), \quad (2.10)$$

where  $T_0$  is the TES temperature,  $V_b$  is the bias voltage,  $R_0$  is the TES resistance, and  $T_{\text{bath}}$  is the temperature of the heat sink.

When the TES temperature becomes  $T$  with a small temperature rise  $\Delta T \equiv T - T_0$ , the change of internal energy is the same as the change of heat, so

$$C \frac{dT}{dt} = \frac{V_b^2}{R(T)} - \frac{G_0}{n} (T^n - T_{\text{bath}}^n) \quad (2.11)$$

is given. In the first order approximation, (2.11) becomes

$$C \frac{d\Delta T}{dt} \simeq -\frac{V_b^2}{R_0^2} \Delta R - G_0 T^{n-1} \Delta T \quad (2.12)$$

$$= \frac{P_b \alpha}{T} \Delta T - G \Delta T. \quad (2.13)$$

$G$  is the thermal conductivity of TES at the temperature  $T$ . The solution of (2.12) is

$$\Delta T = \Delta T_0 \exp\left(-\frac{t}{\tau_{\text{eff}}}\right), \quad (2.14)$$

where

$$\tau_{\text{eff}} \equiv \frac{C/G}{1 + \frac{P_b \alpha}{GT}} \quad (2.15)$$

$$= \frac{\tau_0}{1 + \frac{P_b \alpha}{GT}} \quad (2.16)$$

is an effective time constant. With (2.10) and (2.16),  $\tau_{\text{eff}}$  can be expressed as

$$\tau_{\text{eff}} = \frac{\tau_0}{1 + \frac{\alpha}{n} \left(1 - \left(\frac{T_{\text{bath}}}{T}\right)^n\right)}. \quad (2.17)$$

Moreover, when the temperature of the sink is far less than the temperature of TES ( $T_{\text{bath}}^n \ll T^n$ ),  $\tau_{\text{eff}}$  can be approximated as

$$\tau_{\text{eff}} = \frac{\tau_0}{1 + \frac{\alpha}{n}} \quad (2.18)$$

$$\approx \frac{n}{\alpha} \tau_0. \quad (2.19)$$

(2.19) is, however, only when  $\alpha/n \gg 1$ . As seen in this equation, the TES response time is significantly shortened due to the ETF when  $\alpha$  is large. The energy of incident X-ray photon can be sensed as a current change

$$\Delta I = \frac{V_b}{R(T_0 + \Delta T)} - \frac{V_b}{R(T_0)} \quad (2.20)$$

$$\simeq -\frac{\Delta R}{R} I \quad (2.21)$$

$$\simeq -\alpha \frac{E}{CT} I. \quad (2.22)$$

### General Formalization of ETF and Current Responsivity

Let us consider the response of the voltage-biased microcalorimeter to an externally applied time-dependent microscopic power  $\delta P e^{i\omega t}$ . The response is assumed to be linear, and the temperature change can then be given by  $\delta T e^{i\omega t}$ . Without the feedback, we have

$$P_{\text{bgd}} + \delta P e^{i\omega t} = \bar{G}(T - T_{\text{bath}}) + G\delta T e^{i\omega t} + i\omega C\delta T e^{i\omega t}, \quad (2.23)$$

where  $P_{\text{bgd}}$  is a background power, and  $\bar{G}$  is an averaged thermal conductivity. In thermal equilibrium, the background power is

$$P_{\text{bgd}} = \bar{G}(T - T_{\text{bath}}). \quad (2.24)$$

With (2.23) and (2.24),  $\delta T$  is

$$\delta T = \frac{1}{G} \frac{1}{1 + i\omega\tau_0} \delta P, \quad (2.25)$$

using  $\delta P$ , where  $\tau_0 \equiv C/G$  is the intrinsic time constant.

With the ETF, the equation of energy conservation is given by

$$P_{\text{bgd}} + \delta P e^{i\omega t} + P_b + \delta P_b e^{i\omega t} = \bar{G}(T - T_{\text{bath}}) + G\delta T e^{i\omega t} + i\omega C\delta T e^{i\omega t}. \quad (2.26)$$

With voltage biasing, we have

$$\delta P_b e^{i\omega t} = \frac{dP_b}{dI} \delta I e^{i\omega t} = V_b \delta I e^{i\omega t}, \quad (2.27)$$

$$\delta I e^{i\omega t} = \frac{dI}{dR} \delta R e^{i\omega t} = \frac{d}{dR} \left( \frac{V_b}{R} \right) \delta R e^{i\omega t} = -\frac{V_b}{R^2} \delta R e^{i\omega t}, \quad (2.28)$$

$$\delta R e^{i\omega t} = \frac{dR}{dT} \delta T e^{i\omega t} = \alpha \frac{R}{T} \delta T e^{i\omega t}. \quad (2.29)$$

Using these, (2.26) becomes

$$P_{\text{bgd}} + \delta P e^{i\omega t} + \frac{V_b^2}{R} - \frac{V_b^2}{R^2} \frac{dR}{dT} \delta T e^{i\omega t} = \bar{G}(T - T_{\text{bath}}) + G\delta T e^{i\omega t} + i\omega C\delta T e^{i\omega t}. \quad (2.30)$$

The solution to (2.30) is then

$$\delta T e^{i\omega t} = \frac{1}{\alpha \frac{P_b}{T} + G + i\omega C} \delta P e^{i\omega t} \quad (2.31)$$

$$= \frac{1}{G} \frac{1}{1 + \frac{\alpha P_b}{GT}} \frac{1}{1 + i\omega\tau_{\text{eff}}} \delta P e^{i\omega t}, \quad (2.32)$$

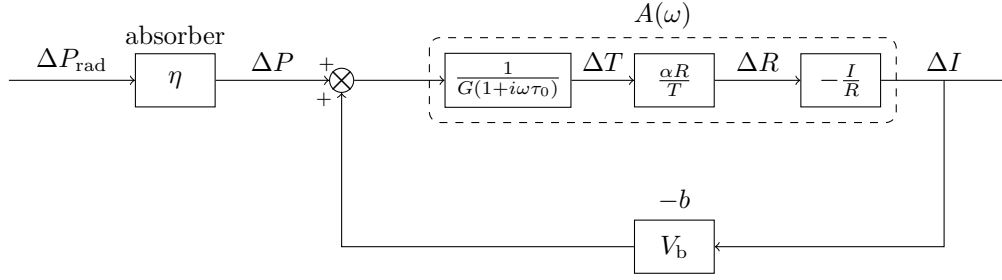


Fig. 2.7 Electrothermal feedback

where

$$\tau_{\text{eff}} \equiv \frac{1}{1 + \frac{\alpha P_b}{GT}} \frac{C}{G} \quad (2.33)$$

is the effective time constant under the ETF.

According to the general feedback theory, the ETF system can be described as Figure 2.7. The feedback  $b$  and the loopgain  $\mathcal{L}(\omega)$  are

$$b = -V_b, \quad (2.34)$$

$$\mathcal{L}(\omega) = \frac{1}{G(1+i\omega\tau_0)} \times \alpha \frac{R}{T} \times \left(-\frac{I}{R}\right) \times (-V_b) = \frac{\alpha P_b}{GT} \frac{1}{1+i\omega\tau_0} \equiv \frac{\mathcal{L}_0}{1+i\omega\tau_0}, \quad (2.35)$$

where

$$\mathcal{L}_0 \equiv \frac{\alpha P_b}{GT} \quad (2.36)$$

is the loopgain at DC. The closed-loop transfer function, or the current responsivity

$$S_I(\omega) \equiv \frac{\delta I}{\delta P} \quad (2.37)$$

can be expressed as

$$S_I(\omega) = \frac{1}{b} \frac{\mathcal{L}(\omega)}{1 + \mathcal{L}(\omega)} \quad (2.38)$$

$$= -\frac{1}{V_b} \frac{\mathcal{L}_0}{\mathcal{L}_0 + 1 + i\omega\tau_0} \quad (2.39)$$

$$= -\frac{1}{V_b} \frac{\mathcal{L}_0}{\mathcal{L}_0 + 1} \frac{1}{1 + i\omega\tau_{\text{eff}}} \quad (2.40)$$

using  $\mathcal{L}(\omega)$ , where

$$\tau_{\text{eff}} \equiv \frac{\tau}{\mathcal{L}_0 + 1}. \quad (2.41)$$

With a large loopgain ( $\mathcal{L}_0 \gg 1$ ), the transfer function becomes

$$S_I(\omega) = -\frac{1}{V_b} \frac{1}{1 + i\omega\tau_{\text{eff}}}. \quad (2.42)$$

In the frequency range  $\omega \ll 1/\tau_{\text{eff}}$  we have

$$S_I = -\frac{1}{V_b}. \quad (2.43)$$

A response to an input  $P(t) = E\delta(t)$  can be calculated as

$$P(\omega) = \frac{1}{2\pi} \int_{-\infty}^{\infty} E\delta(t)e^{i\omega t} dt \quad (2.44)$$

$$= \frac{E}{2\pi}, \quad (2.45)$$

and the output becomes

$$I(\omega) = S_I(\omega)P(\omega) \quad (2.46)$$

$$= -\frac{E}{2\pi V_b} \frac{\mathcal{L}_0}{\mathcal{L}_0 + 1} \frac{1}{1 + i\omega\tau_{\text{eff}}}. \quad (2.47)$$

By an inverse Fourier transform, the current output in the time domain becomes

$$I(t) = \int_{-\infty}^{\infty} I(\omega)e^{-i\omega t} d\omega \quad (2.48)$$

$$= -\frac{1}{2\pi} \frac{E}{V_b} \frac{\mathcal{L}_0}{\mathcal{L}_0 + 1} \int_{-\infty}^{\infty} \frac{e^{-i\omega t}}{1 + i\omega\tau_{\text{eff}}} d\omega \quad (2.49)$$

$$= -\frac{E}{V_b\tau_{\text{eff}}} \frac{\mathcal{L}_0}{\mathcal{L}_0 + 1} \exp\left(-\frac{t}{\tau_{\text{eff}}}\right) \quad (2.50)$$

$$= -\frac{\alpha E}{CT} I_0 \exp\left(-\frac{t}{\tau_{\text{eff}}}\right), \quad (2.51)$$

where  $I_0$  is the current through the TES in the steady state. On the other hand, the temperature rise due to the input  $P(t) = E\delta(t)$  can be expressed as

$$\Delta T(\omega) = \frac{1}{G(1 + i\omega\tau_0)} \frac{1}{1 + \mathcal{L}(\omega)} P(\omega) \quad (2.52)$$

$$= \frac{1}{2\pi} \frac{E}{G} \frac{1}{1 + \mathcal{L}_0} \frac{1}{1 + i\omega\tau_{\text{eff}}} \quad (2.53)$$

in the frequency domain, and converting back to the time domain we have

$$\Delta T(t) = \int_{-\infty}^{\infty} \Delta T(\omega)e^{-i\omega t} d\omega \quad (2.54)$$

$$= \frac{1}{2\pi} \frac{E}{G} \frac{1}{\mathcal{L}_0 + 1} \int_{-\infty}^{\infty} \frac{e^{-i\omega t}}{1 + i\omega\tau_{\text{eff}}} d\omega \quad (2.55)$$

$$= \frac{E}{G\tau_{\text{eff}}} \frac{1}{\mathcal{L}_0 + 1} \exp\left(-\frac{t}{\tau_{\text{eff}}}\right) \quad (2.56)$$

$$= \frac{E}{C} \exp\left(-\frac{t}{\tau_{\text{eff}}}\right). \quad (2.57)$$

When  $\mathcal{L}_0$  is considered to be constant, (2.50) gives

$$\int V_b I(t) dt = -\frac{\mathcal{L}_0}{\mathcal{L}_0 + 1} E. \quad (2.58)$$

Thus, the integration of Joule heating due to an incident X-ray photon is proportional to the incident energy  $E$ . For the energy,  $\mathcal{L}_0/(\mathcal{L}_0 + 1)$  is compensated by the change of Joule heating, and  $1/(\mathcal{L}_0 + 1)$  escapes to the heat sink. When  $\mathcal{L}_0 \gg 1$ , the integration of Joule heating is equivalent to the incident energy.

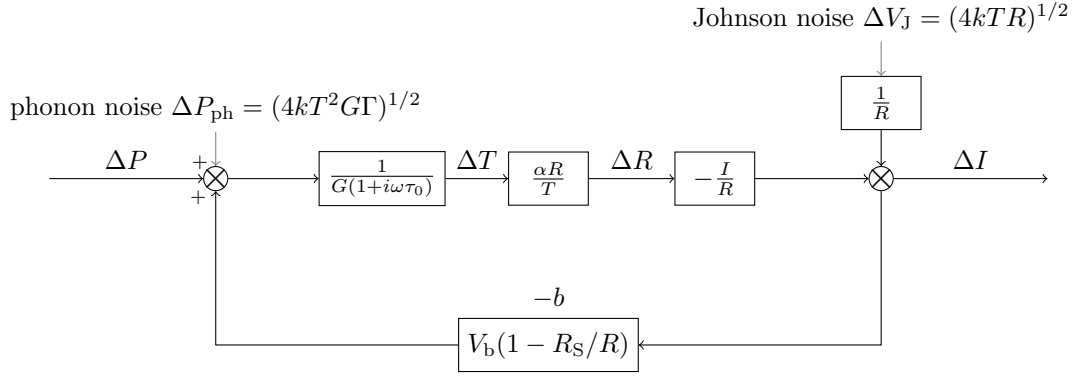


Fig. 2.8 Electrothermal feedback with intrinsic noises

## 2.2.4 Intrinsic Noises

TES suffers from two intrinsic noises. One is Johnson noise arisen from the TES resistance, and the other is phonon noise arisen from the exchange of energy between the TES and the heat sink. Figure 2.8 shows the ETF diagram with these intrinsic noises. Because of their origins, the positions where those noises are input are slightly different. The current fluctuation due to a small thermal fluctuation  $\delta P_{\text{ph}}$  is

$$\delta I_{\text{ph}} = -\frac{1}{V_b} \frac{\mathcal{L}(\omega)}{1 + \mathcal{L}(\omega)} \delta P_{\text{ph}} \quad (2.59)$$

$$= S_I \delta P_{\text{ph}}. \quad (2.60)$$

Thus, the current spectral density of phonon noise is given by

$$\delta I_{\text{ph}}^2 = |S_I|^2 \delta P_{\text{ph}}^2 \quad (2.61)$$

$$= \frac{1}{V_b^2} \left( \frac{\mathcal{L}_0}{\mathcal{L}_0 + 1} \right)^2 \frac{1}{1 + \omega^2 \tau_{\text{eff}}^2} \delta P_{\text{ph}}^2. \quad (2.62)$$

According to Mather [21], the power spectral density of phonon noise in  $0 \leq f < \infty$  can be given by

$$\delta P_n^2 = 4k_B G T^2 \frac{\int_{T_{\text{bath}}}^T \left( \frac{t\kappa(t)}{T\kappa(T)} \right)^2 dt}{\int_{T_{\text{bath}}}^T \left( \frac{\kappa(t)}{\kappa(T)} \right) dt} \quad (2.63)$$

$$\equiv 4k_B G T^2 \Gamma, \quad (2.64)$$

where  $\kappa(T)$  is a thermal conductivity of thermal link. Assuming  $\theta \equiv T_{\text{bath}}/T$  and  $\kappa(T) = \kappa(T_{\text{bath}})\theta^{-(n-1)}$ ,  $\Gamma$  can be written as

$$\Gamma = \frac{n}{2n+1} \frac{1 - \theta^{(2n+1)}}{1 - \theta^n}. \quad (2.65)$$

Using (2.64) and (2.62), the current spectral density of phonon noise can be expressed as

$$\delta I_{\text{ph}}^2 = 4k_{\text{B}}GT^2\Gamma|S_I|^2 \quad (2.66)$$

$$= \frac{4k_{\text{B}}GT^2\Gamma}{b^2} \left( \frac{\mathcal{L}_0}{\mathcal{L}_0 + 1} \right)^2 \frac{1}{1 + \omega^2\tau_{\text{eff}}^2} \quad (2.67)$$

$$= \frac{4k_{\text{B}}GT^2\Gamma}{V_{\text{b}}^2} \left( \frac{\mathcal{L}_0}{\mathcal{L}_0 + 1} \right)^2 \frac{1}{1 + \omega^2\tau_{\text{eff}}^2}. \quad (2.68)$$

On the other hand, the current fluctuation  $\delta I_{\text{J}}^0$  due to Johnson noise  $\delta V_{\text{J}}$  is

$$\delta I_{\text{J}}^0 = \frac{\delta V_{\text{J}}}{R}, \quad (2.69)$$

and the output fluctuation becomes

$$\delta I_{\text{J}} = \frac{1}{1 + \mathcal{L}(\omega)} \delta I_{\text{J}}^0 \quad (2.70)$$

$$= \frac{1}{\mathcal{L}_0 + 1 + i\omega\tau_{\text{eff}}} \frac{\delta V_{\text{J}}}{R} \quad (2.71)$$

$$= \frac{1}{\mathcal{L}_0 + 1} \frac{1 + i\omega\tau_0}{1 + i\omega\tau_{\text{eff}}} \frac{\delta V_{\text{J}}}{R}. \quad (2.72)$$

The current spectral density of Johnson noise is given by  $\delta V_{\text{J}}^2 = 4k_{\text{B}}RT$  in  $0 \leq f < \infty$ , the output current spectral density then becomes

$$\delta I_{\text{J}}^2 = \frac{4k_{\text{B}}T}{R} \left( \frac{1}{\mathcal{L}_0 + 1} \right)^2 \left| \frac{1 + i\omega\tau_0}{1 + i\omega\tau_{\text{eff}}} \right|^2 \quad (2.73)$$

$$= \frac{4k_{\text{B}}T}{R} \left( \frac{1}{\mathcal{L}_0 + 1} \right)^2 \frac{1 + \omega^2\tau_0^2}{1 + \omega^2\tau_{\text{eff}}^2} \quad (2.74)$$

$$= \begin{cases} \frac{4k_{\text{B}}T}{R} \left( \frac{1}{\mathcal{L}_0 + 1} \right)^2 & \text{if } \omega \ll \tau_0^{-1} \\ \frac{4k_{\text{B}}T}{R} & \text{if } \omega \gg \tau_{\text{eff}}^{-1} \end{cases}. \quad (2.75)$$

Note that in the frequency range  $\omega \ll \tau_0^{-1}$ , the Johnson noise is suppressed by the ETF, while in the frequency range  $\omega \gg \tau_{\text{eff}}^{-1}$ , it becomes the original value.

The total noise current spectral density is given by the sum of squares of the phonon noise and the Johnson noise as

$$\delta I^2 = \delta I_{\text{J}}^2 + \delta I_{\text{ph}}^2 \quad (2.76)$$

$$= \frac{4k_{\text{B}}T}{R} \left( \frac{1}{\mathcal{L}_0 + 1} \right)^2 \frac{1 + \omega^2\tau_0^2}{1 + \omega^2\tau_{\text{eff}}^2} + 4k_{\text{B}}GT^2\Gamma \frac{1}{V_{\text{b}}^2} \left( \frac{\mathcal{L}_0}{\mathcal{L}_0 + 1} \right)^2 \frac{1}{1 + \omega^2\tau_{\text{eff}}^2} \quad (2.77)$$

$$= \frac{4k_{\text{B}}T}{R} \frac{1 + \Gamma\alpha\mathcal{L}_0}{(\mathcal{L}_0 + 1)^2 + \omega^2\tau_{\text{eff}}^2} \quad (2.78)$$

in  $0 \leq f < \infty$ . In the limit of strong ETF, it becomes

$$\delta I^2 = \frac{4k_{\text{B}}T}{R} \frac{n/2 + \omega^2\tau_{\text{eff}}^2}{1 + \omega^2\tau_{\text{eff}}^2}. \quad (2.79)$$

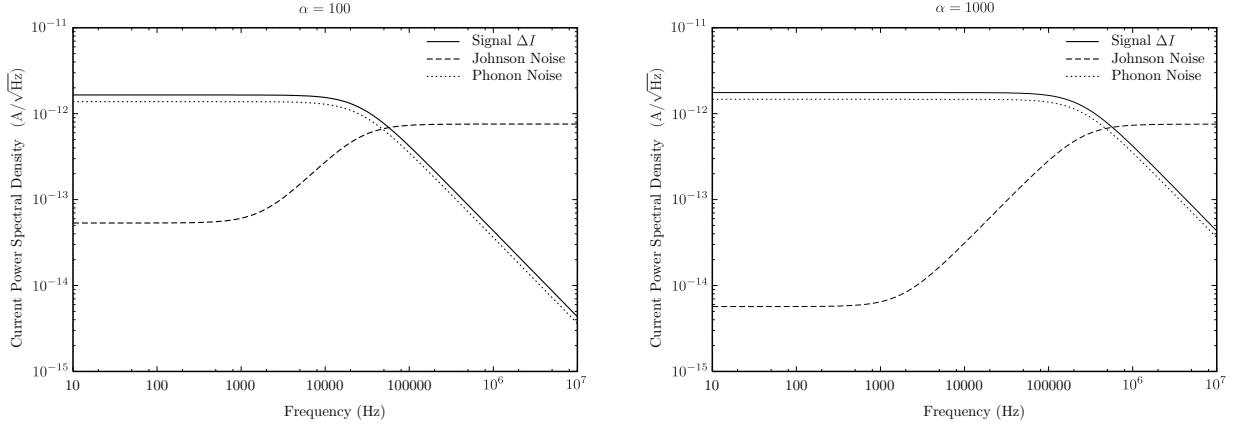


Fig. 2.9 Examples of noise current power spectral density. The left plot shows when  $\alpha = 100$ , while the right shows when  $\alpha = 1000$ .

Figure 2.9 shows the frequency dependencies of the noise current power spectral density. To see the relation of the phonon noise and Johnson noise, we have the ratio of those two terms as

$$\frac{\delta I_{\text{ph}}^2}{\delta I_{\text{J}}^2} = \frac{\alpha \mathcal{L}_0 \Gamma}{1 + \omega^2 \tau_0^2}. \quad (2.80)$$

Thus, in the low frequency region the Johnson noise is suppressed and the phonon noise is  $\alpha \mathcal{L}_0 \Gamma$  time larger, but in the region  $\omega > \tau_0^{-1}$  the Johnson noise starts dominating, and in the region  $\omega \gg \tau_{\text{eff}}^{-1}$  the Johnson noise finally dominates.

In contrast, the ratio of the signal and phonon noise is frequency independent as

$$\frac{\delta P_{\text{signal}}^2}{\delta P_{\text{n}}^2} = \frac{2E^2}{4k_B G T^2 \Gamma}, \quad (2.81)$$

because those two have identical frequency dependencies.

With (2.40) and (2.75), the Johnson noise can be expressed as

$$\delta I_{\text{J}}^2 = \frac{4k_B T}{R} \frac{b^2 (1 + \omega^2 \tau_0^2)}{\mathcal{L}_0^2} |S_I|^2 \quad (2.82)$$

using the current responsivity  $S_I$ . From (2.67) and (2.75), the intrinsic noise is given by

$$\delta I^2 = \frac{4k_B T}{R} \frac{1 + \omega^2 \tau_0^2}{\mathcal{L}_0^2} b^2 |S_I|^2 + 4k_B G T^2 \Gamma |S_I|^2. \quad (2.83)$$

The noise equivalent power  $\text{NEP}(f)$  is defined as

$$\text{NEP}(f)^2 = \left| \frac{\delta I}{S_I} \right|^2, \quad (2.84)$$

and the  $\text{NEP}(f)$  for the intrinsic noise can be calculated as

$$\text{NEP}(f)^2 = \left| \frac{\delta I}{S_I} \right|^2 \quad (2.85)$$

$$= \frac{4k_B T}{R} \frac{b^2}{\mathcal{L}_0^2} \left( 1 + (2\pi f)^2 \tau_0^2 + \frac{\mathcal{L}_0^2}{b^2} RGT\Gamma \right) \quad (2.86)$$

$$= 4k_B T P_b \left( \frac{1 + (2\pi f)^2 \tau_0^2}{\mathcal{L}_0^2} + \frac{\alpha\Gamma}{\mathcal{L}_0} \right). \quad (2.87)$$

### 2.2.5 Energy Resolution

Once the NEP is given, the energy resolution is given by

$$\Delta E_{\text{rms}} = \left( \int_0^\infty \frac{4df}{\text{NEP}^2(f)} \right)^{-\frac{1}{2}} \quad (2.88)$$

according to Moseley et al. [22]. Using (2.87), the energy resolution for the intrinsic noises is thus

$$\Delta E_{\text{rms}} = \left( \int_0^\infty \frac{4df}{\frac{4k_B T}{R} \frac{b^2}{\mathcal{L}_0^2} \left( (1 + (2\pi f)^2 \tau_0^2) + \frac{\mathcal{L}_0^2}{b^2} RGT\Gamma \right)} \right)^{-\frac{1}{2}} \quad (2.89)$$

$$= \sqrt{\frac{4k_B T}{R} \frac{b^2}{\mathcal{L}_0^2} \tau_0 \sqrt{1 + \frac{\mathcal{L}_0^2}{b^2} RGT\Gamma}} \quad (2.90)$$

$$= \sqrt{4k_B T^2 C \frac{b^2}{RGT\mathcal{L}_0^2} \sqrt{1 + \frac{\mathcal{L}_0^2}{b^2} RGT\Gamma}}. \quad (2.91)$$

Defining  $\xi$  as

$$\xi \equiv 2 \sqrt{\frac{b^2}{RGT\mathcal{L}_0^2} \sqrt{1 + \frac{\Gamma}{b^2}}, \frac{\Gamma}{RGT\mathcal{L}_0^2}} \quad (2.92)$$

we have the full width at half maximum (FWHM) intrinsic energy resolution as

$$\Delta E_{\text{FWHM}} = 2.35\xi \sqrt{k_B T^2 C}. \quad (2.93)$$

From (2.34) and (2.36), (2.92) becomes

$$\xi = 2\sqrt{\frac{1}{\alpha\mathcal{L}_0} \sqrt{1 + \alpha\mathcal{L}_0\Gamma}}. \quad (2.94)$$

### 2.2.6 Optimal Filtering

An acquired X-ray pulse signal is usually contaminated by noises, and taking its peak value as a pulse height does not achieve the best energy resolution. In this type of application, optimal filtering<sup>\*1</sup> is generally used to retrieve the pulse height minimizing the deterioration due to noises.

<sup>\*1</sup> The term optimal filtering sometimes refers the Wiener filter, but here it refers the matched filter.

Let us assume  $D(t)$  to be the acquired pulse signal, and in frequency domain it can be represented as

$$D(f) = A \times M(f) + N(f), \quad (2.95)$$

where  $M(f)$  and  $N(f)$  are ideal spectra of the pulse and the noise, and  $A$  is the amplitude of the pulse.  $M(f)$  is also called a model pulse. We now determine  $A$  so that the difference of the acquired pulse and the model pulse is minimized using the least-square method. Defining the difference of the acquired pulse and the model pulse as

$$\chi^2 \equiv \int \frac{|D(f) - A \times M(f)|^2}{|N(f)|^2}, \quad (2.96)$$

$A$  that minimize  $\chi^2$  is given by

$$A = \frac{\int_{-\infty}^{\infty} \frac{DM^* + D^*M}{2|N|^2} df}{\int_{-\infty}^{\infty} \frac{|M|^2}{|N|^2} df}. \quad (2.97)$$

$D(f)$  and  $M(f)$  are Fourier transformations of real functions, and thus  $D(-f) = D(f)^*$  and  $M(-f) = M(f)^*$ . We therefore have

$$\int_{-\infty}^{\infty} \frac{D(f)M(f)^*}{2|N|^2} df = - \int_{-\infty}^{\infty} \frac{D(-f)M(-f)^*}{2|N|^2} df = \int_{-\infty}^{\infty} \frac{M(f)D(f)^*}{2|N|^2} df, \quad (2.98)$$

and  $A$  can be given as

$$A = \frac{\int_{-\infty}^{\infty} \frac{DM^*}{|N|^2} df}{\int_{-\infty}^{\infty} \frac{|M|^2}{|N|^2} df}, \quad (2.99)$$

or

$$A = \frac{\int_{-\infty}^{\infty} \frac{D}{M} \left| \frac{M}{N} \right|^2 df}{\int_{-\infty}^{\infty} \left| \frac{M}{N} \right|^2 df}. \quad (2.100)$$

According to (2.100),  $A$  is the weighted average of  $D(f)/M(f)$  with the weight of  $[M(f)/N(f)]^2$ , which is the signal-to-noise ratio. (2.100) can be further transformed into

$$A = \frac{\int_{-\infty}^{\infty} D(t) \mathcal{F}^{-1} \left( \frac{M(f)}{|N(f)|^2} \right) dt}{\int_{-\infty}^{\infty} \left| \frac{M}{N} \right|^2 df}, \quad (2.101)$$

where  $\mathcal{F}^{-1}$  is the inverse-Fourier transformation. We now define a template of optimal filtering  $T(t)$  as

$$T(t) \equiv \mathcal{F}^{-1} \left( \frac{M(f)}{|N(f)|^2} \right). \quad (2.102)$$

Using (2.102), the pulse height  $H$  is given by

$$H = N \int_{-\infty}^{\infty} D(t)T(t)dt, \quad (2.103)$$

or for discrete signal data

$$H = N \sum_i D_i(t)T_i(t), \quad (2.104)$$

where  $N$  is a normalized constant, and  $D_i(t)$  and  $T_i(t)$  are the quantized pulse and template.

To calculate  $T(t)$ , we need  $M(f)$  and  $N(f)$ . They are generally estimated from the ensemble averages of the pulse and the noise as

$$M(t) = \langle D(t) \rangle \quad (2.105)$$

and

$$N(f) = \langle E(f) \rangle, \quad (2.106)$$

where  $E(f)$  is the acquired noise signal in the frequency domain.

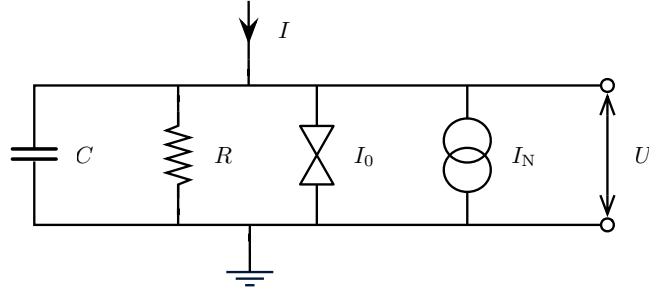


Fig. 2.10 RCSJ model

## 2.3 Superconducting Quantum Interference Devices

### 2.3.1 Josephson Junctions

A Josephson junction consists of two superconductors separated by a weak insulator. If the coupling is weak enough, a super-current  $I_S$  flows between the superconductors. Let  $\delta$  be the phase difference across the superconductors, the super-current  $I_S$  is then

$$I_S = I_0 \sin \delta. \quad (2.107)$$

$I_0$  is called a critical current of the junction, and gives the maximum current of the super-current. No voltage drop thus occurs at the junction when the current through the junction is below  $I_0$ .

When the phase difference  $\delta$  evolves with time  $t$ , a voltage  $U$  is generated across the junction as

$$\dot{\delta} \equiv \frac{d\delta}{dt} = \frac{2e}{\hbar} U = \frac{2\pi}{\Phi_0} U, \quad (2.108)$$

where  $\Phi_0 = h/2e \approx 2.07 \times 10^{-15}$  Wb is called the flux quantum.

### 2.3.2 RCSJ Model

Josephson junctions are generally modeled by a resistively- and capacitively-shunted junction (RCSJ) model. Figure 2.10 shows the equivalent circuit of RCSJ model. From Kirchhoff's laws, we have

$$C\dot{U} + \frac{U}{R} + I_0 \sin \delta = I + I_N(t). \quad (2.109)$$

For now we ignore the noise term  $I_N(t)$ , and (2.109) then becomes

$$\frac{\Phi_0}{2\pi} C\ddot{\delta} + \frac{\Phi_0}{2\pi} \frac{1}{R} \dot{\delta} = I - I_0 \sin \delta = -\frac{2\pi}{\Phi_0} \frac{\partial U_J}{\partial \delta} \quad (2.110)$$

using (2.108).  $U_J$  is called the tilted washboard potential and given by

$$U_J \equiv \frac{\Phi_0}{2\pi} \{I_0(1 - \cos \delta) - I\delta\} = E_J(1 - \cos \delta - i\delta), \quad (2.111)$$

where  $E_J$  is the Josephson coupling energy given by  $E_J = I_0\Phi_0/2\pi$ , and  $i$  is the normalized bias current given by  $i \equiv I/I_0$ .  $U_J$  can be normalized using  $E_J$  and let  $u_J$  be

$$u_J = 1 - \cos \delta - i\delta. \quad (2.112)$$

When  $I < I_0$ , the phase is trapped in one of the minima of the washboard potential, and the response of the junction then oscillates with the plasma frequency  $\omega_p$ , which is given by

$$\omega_{p,i} = \omega_p(1 - i^2)^{1/4} \quad \text{for} \quad \omega_p = \left( \frac{2\pi I_0}{\Phi_0 C} \right)^{1/2}. \quad (2.113)$$

In this case the time average is zero, so the voltage across the junction is also zero. When  $I > I_0$ , the phase can move over potential walls, and  $\dot{\delta}$  and the voltage across the junction then becomes non-zero. Substituting (2.110) with the characteristic frequency  $\omega_c \equiv 2\pi I_0 R / \Phi_0$ , which is the Josephson frequency at the characteristic voltage  $V_c \equiv I_0 R$ , we have

$$\frac{\ddot{\delta}}{\omega_p^2} + \frac{\dot{\delta}}{\omega_c} = i - \sin \delta = -\frac{\partial u_J}{\partial \delta}, \quad (2.114)$$

or

$$\beta_C \frac{\ddot{\delta}}{\omega_c^2} + \frac{\dot{\delta}}{\omega_c} = i - \sin \delta = -\frac{\partial u_J}{\partial \delta}. \quad (2.115)$$

$\beta_C$  is called Stewart-McCumber and defined as

$$\beta_C \equiv \left( \frac{\omega_c}{\omega_p} \right)^2 = \frac{2\pi}{\Phi_0} I_0 R^2 C. \quad (2.116)$$

Let us consider two limits,  $\beta_C \ll 1$  and  $\beta_C \gg 1$ , for (2.115).

In the limit of  $\beta_C \ll 1$ , which is called the over-damped limit, we can ignore the inertial term in (2.115), which is comparable to the negligible junction capacitance. In this limit the RCSJ model is simplified to the RSJ model. Since the inertial term is negligible, the particle gets trapped in the potential at  $I = I_0$  when reducing the bias current  $I$ , and the voltage across the junction instantly becomes zero. The  $I$ - $V$  characteristic is therefore non-hysteretic. Assuming  $\beta_C = 0$ , we can solve (2.115) for the normalized voltage  $u \equiv U/I_0 R$  as

$$u(t) = \begin{cases} 0 & i < 1 \\ \frac{i^2 - 1}{i + \cos \omega t} & i > 1 \end{cases}, \quad (2.117)$$

where  $\omega = \omega_c \sqrt{i^2 - 1}$ . When  $i > 1$ ,  $v$  oscillates with the frequency  $\omega$ , and the frequency increases as  $i$  increases. The normalized time averaged voltage  $v \equiv V/I_0 R$  ( $V$  is time averaged voltage) is

$$v = \begin{cases} 0 & i < 1 \\ \sqrt{i^2 - 1} & i > 1 \end{cases}. \quad (2.118)$$

In the limit of  $\beta_C \gg 1$ , which is called the under-damped limit, the dynamics of junction is determined by the  $RC$  circuit since the Josephson frequency is much higher than the relaxation frequency  $\omega_{RC}$ . The voltage across the junction keeps a finite value even at  $I < I_0$  (or  $i < 1$ ) when reducing  $I$ . On the other hand, when increasing  $I$  the voltage across the junction stays zero until  $I > I_0$  (or  $i > 1$ ). In this limit the  $I$ - $V$  characteristic is severely

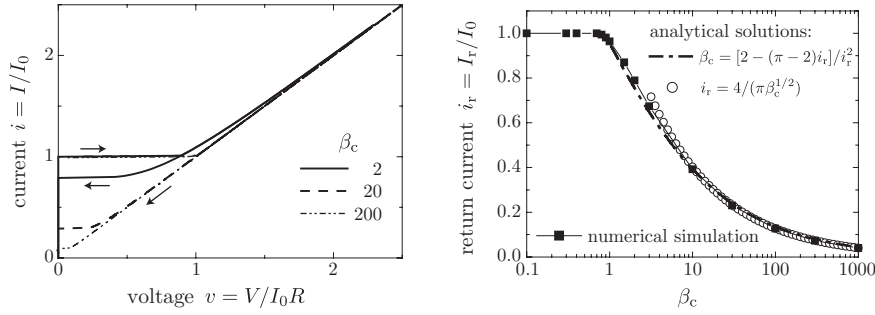


Fig. 2.11 Calculated hysteretic  $I$ - $V$  characteristics for various values of  $\beta_C$  (left) and the return critical current vs.  $\beta_C$  (right). Adapted from Clarke and Braginski [6].

hysteretic.

Figure 2.11 (left) shows the calculated  $I$ - $V$  characteristics for various values of  $\beta_C$  [6]. Reducing the bias current  $I$  from above  $I_0$ , the voltage across the junction becomes zero at the return critical current  $I_r(\beta_C)$ , which is the function of  $\beta_C$ . The normalized return critical current  $i_r = I_r/I_0$  is also the function of  $\beta_C$ , and it monotonically decreases from 1 to 0 for increasing  $\beta_C$ . Figure 2.11 (right) shows the approximated analytical solutions as well as the result of numerical simulation [6].

To achieve non-hysteretic  $I$ - $V$  characteristic, a shunt resistor is generally inserted in parallel with the junction to minimize  $\beta_C$  below 1.

### 2.3.3 Johnson-Nyquist Noise

The current fluctuation  $I_N$  due to Johnson noise is

$$I_N^2 = \frac{4k_B T}{R}. \quad (2.119)$$

Let  $i_N \equiv I_N/I_0$  be the normalized noise current, the washboard potential (2.111) now becomes

$$U_{J,N} = E_J \{1 - \cos \delta - [i + i_N(t)]\delta\}, \quad (2.120)$$

which means that the averaged tilt of the potential fluctuate with the normalized noise current.

Here we define a noise parameter  $\Gamma$  as the ratio of the thermal energy over the Josephson coupling energy

$$\Gamma \equiv \frac{k_B T}{E_J} = \frac{2\pi k_B T}{I_0 \Phi_0}. \quad (2.121)$$

Using  $\Gamma$  and  $\omega_c$ ,  $i_N$  now becomes

$$i_N^2 = \frac{4\Gamma}{\omega_c}.$$

Even when  $I < I_0$ , the total current through the junction with noise,  $I + I_N(t)$ , sometime exceeds the critical current  $I_0$ . When it happens, the phase move over the next minima in the potential, which makes a pulse-like voltage across the junction. In this case the time-averaged voltage becomes a finite value, making a rounding effect at the transition edge of superconducting state and normal state. Figure 2.12 shows the  $I$ - $V$  characteristic obtained by numerically solving

$$\beta_C \frac{\ddot{\delta}}{\omega_c^2} + \frac{\dot{\delta}}{\omega_c} = i + i_N(t) - \sin \delta \quad (2.122)$$

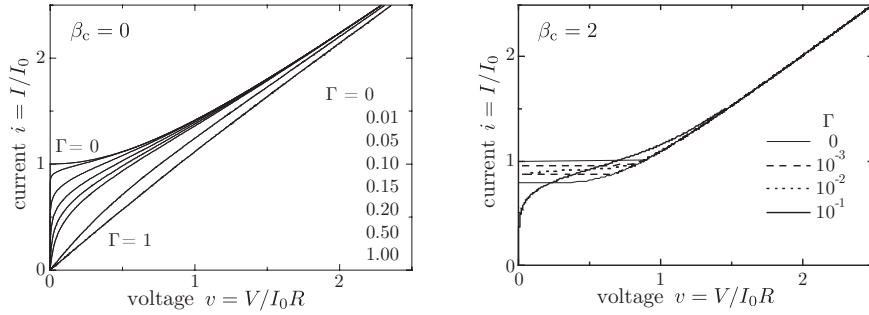


Fig. 2.12 Calculated  $I$ - $V$  characteristic for various values of  $\Gamma$  for negligible capacitance (left) and finite capacitance (right). Adapted from Clarke and Braginski [6].

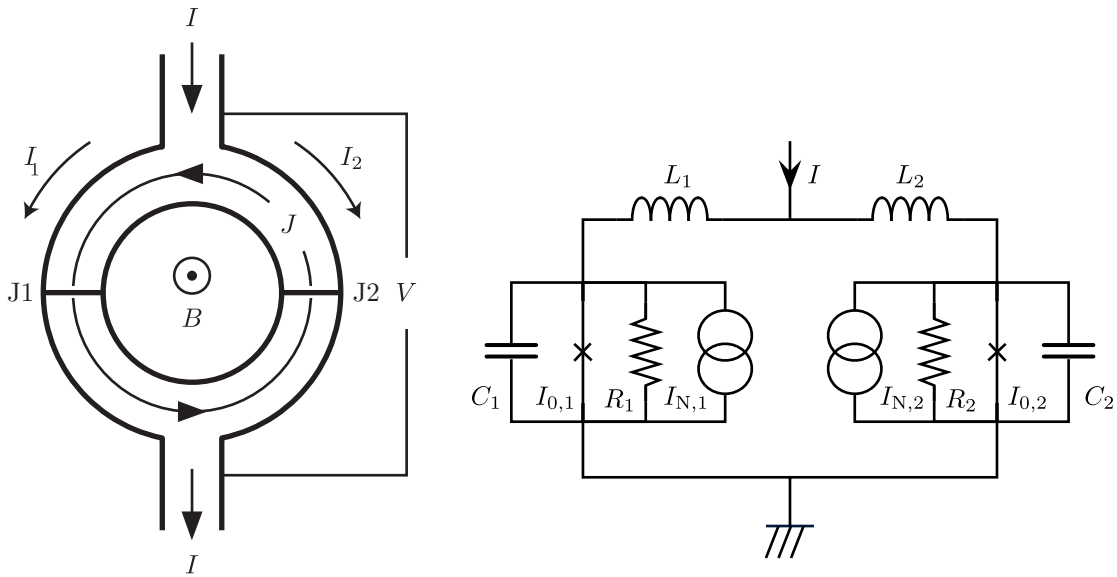


Fig. 2.13 The dc SQUID: the schematic diagram of dc SQUID (left) and the equivalent circuit of dc SQUID

[6]. Figure 2.12 (left) shows the rounding effect due to  $\Gamma$ . The hysteresis in the  $I$ - $V$  characteristic in  $\beta_C > 1$  is also minimized by  $\Gamma$ . This is because  $I + I_N(t)$  can be less than  $I_r$  even when  $I > I_r$  due to the current fluctuation.

From the definition of  $\Gamma$  we see the increase of noise when the operating temperature  $T$  becomes larger or the critical current  $I_0$  becomes smaller. If we redefine  $\Gamma$  as  $\Gamma = I_{th}/I_0$ , the thermal noise current  $I_{th}$  is defined by

$$I_{th} \equiv \Gamma I_0 = \frac{2\pi}{\Phi_0} k_B T. \quad (2.123)$$

Practically  $\Gamma$  should be less than one, and  $I_{th}$  therefore gives the minimum critical current. At liquid nitrogen temperature,  $I_{th} = 3.23 \mu\text{A}$ , and at liquid helium temperature,  $I_{th} = 176 \text{ nA}$ . The critical current should be larger than these.

### 2.3.4 dc SQUID

A dc SQUID consists of two Josephson junctions and a superconducting ring. Figure 2.13 shows the schematic diagram (left) and the equivalent circuit of dc SQUID (right).  $I_c$ , which is the sum of the critical currents at the junctions, modulates periodically with a period of  $\Phi_0 = h/2e$  once an external magnetic flux  $H = B/\mu_0$  is

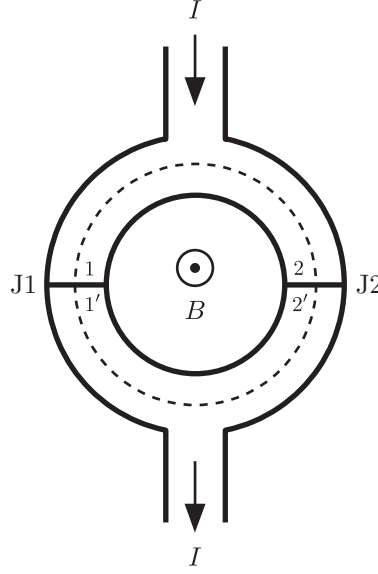


Fig. 2.14 The integral path on the superconducting ring of dc SQUID

applied to the superconducting ring. By reading  $I_c$ , we can precisely obtain the microscopic flux applied to the dc SQUID. More generally, the voltage across the ring is read by biasing the SQUID with a constant current above  $I_c$ . A large  $I_c$  allows a large super-current flow, which makes the voltage across the ring small, while a small  $I_c$  makes the voltage across the ring large. The dc SQUID, therefore, is a flux-to-voltage converter.

### 2.3.5 Principles of dc SQUID

Let us consider integral paths  $1 \rightarrow 2$  and  $1' \rightarrow 2'$  on the superconducting ring of dc SQUID (Figure 2.14). Let  $\phi(1)$ ,  $\phi(2)$ ,  $\phi(1')$  and  $\phi(2')$  be phases at the junctions. We compute integrals along the paths and get

$$\phi(1) - \phi(2) = \frac{2\pi}{\Phi_0} \mu_0 \lambda_L^2 \int_2^1 \vec{j}_s d\vec{l} + \frac{2\pi}{\Phi_0} \int_2^1 \vec{A} d\vec{l} \quad (2.124)$$

and

$$\phi(2') - \phi(1') = \frac{2\pi}{\Phi_0} \mu_0 \lambda_L^2 \int_{1'}^{2'} \vec{j}_s d\vec{l} + \frac{2\pi}{\Phi_0} \int_{1'}^{2'} \vec{A} d\vec{l}, \quad (2.125)$$

where  $\lambda_L$  is the London penetration depth,  $\vec{j}_s$  is the critical current density of superconductor, and  $\vec{A}$  is the vector potential of applied magnetic flux. Summing (2.124) and (2.132) and adding  $(2\pi/\Phi_0) [\int_{2'}^2 \vec{A} d\vec{l} + \int_1^{1'} \vec{A} d\vec{l}]$  to the both sides we have

$$\begin{aligned} \phi(2') - \phi(2) - \frac{2\pi}{\Phi_0} \int_2^{2'} \vec{A} d\vec{l} - \left( \phi(1') - \phi(1) - \frac{2\pi}{\Phi_0} \int_1^{1'} \vec{A} d\vec{l} \right) \\ = \frac{2\pi}{\Phi_0} \oint \vec{A} d\vec{l} + \frac{2\pi}{\Phi_0} \mu_0 \lambda_L^2 \left( \int_2^1 \vec{j}_s d\vec{l} + \int_{1'}^{2'} \vec{j}_s d\vec{l} \right). \end{aligned} \quad (2.126)$$

We can ignore the integrals at the left side because of the size ratio of superconductors and insulators. Defining  $\delta_1 \equiv \phi(1') - \phi(1)$  and  $\delta_2 \equiv \phi(2') - \phi(2)$  yields

$$\delta_2 - \delta_1 = \frac{2\pi}{\Phi_0} \left\{ \Phi + \mu_0 \lambda_L^2 \left( \int_2^1 \vec{j}_s d\vec{l} + \int_{1'}^{2'} \vec{j}_s d\vec{l} \right) \right\} = \frac{2\pi}{\Phi_0} \Phi_T, \quad (2.127)$$

where  $\Phi_T$  is the total flux through the superconducting ring. Let  $L$  be the self-inductance of the superconducting ring and  $J$  be the super-current in the ring, and  $\Phi_T$  then becomes

$$\Phi_T = \Phi_a + LJ, \quad (2.128)$$

where  $\Phi_a$  is the externally applied magnetic flux.

Figure 2.13 (right) shows the equivalent circuit of dc SQUID using the RCSJ model. With a current at the junction J1,  $I_1 = I/2 + J$ , and a current at the junction J2,  $I_2 = I/2 - J$ , we have

$$\frac{I}{2} \pm J = I_{0,k} \sin \delta_k + \frac{\Phi_0}{2\pi R_k} \dot{\delta}_k + \frac{\Phi_0}{2\pi} C_k \ddot{\delta}_k + I_{N,k} \quad (\text{for } k = 1, 2) \quad (2.129)$$

for each junction. The voltages  $U_k$  ( $k = 1, 2$ ) across the junctions are

$$U_k = \frac{\Phi_0}{2\pi} \dot{\delta}_k \quad (k = 1, 2). \quad (2.130)$$

Here we define the averaged critical current  $I_0 = (I_{0,1} + I_{0,2})/2$ , (twice) the parallel resistance  $R = 2R_1 R_2 / (R_1 + R_2)$  and the capacitance  $C = (C_1 + C_2)/2$ , and normalize (2.129) and (2.127) using  $I_0$  for currents,  $R$  for resistances,  $\tau \equiv \Phi_0 / (2\pi I_0 R) = \omega_c^{-1}$  for time,  $I_0 R$  for voltages, and  $\Phi_0$  for magnetic flux. We then obtain

$$\frac{i}{2} + j = (1 - \alpha_I) \sin \delta_1 + (1 - \alpha_R) \dot{\delta}_1 + \beta_c (1 - \alpha_C) \ddot{\delta}_1 + i_{N,1}, \quad (2.131)$$

$$\frac{i}{2} - j = (1 + \alpha_I) \sin \delta_2 + (1 + \alpha_R) \dot{\delta}_2 + \beta_c (1 + \alpha_C) \ddot{\delta}_2 + i_{N,2}, \quad (2.132)$$

and

$$\delta_2 - \delta_1 = 2\pi(\phi_a - \frac{1}{2}\beta_L j), \quad (2.133)$$

where  $i \equiv I/I_0$ ,  $j \equiv J/I_0$ ,  $i_{N,k} \equiv I_{N,k}/I_0$  ( $k = 1, 2$ ), and  $\phi_a = \Phi_a/\Phi_0$ .  $\alpha_I$ ,  $\alpha_R$ , and  $\alpha_C$  are parametrize asymmetries in the junction critical currents, resistances and capacitances, respectively. Dots above variables are derivatives with respect to  $\tau$ .  $\beta_L$  is called the screening parameter defined as

$$\beta_L \equiv \frac{2LI_0}{\Phi_0}. \quad (2.134)$$

The normalized voltages  $u_k$  are given by  $u_k = \dot{\delta}_k$  ( $k = 1, 2$ ).

We now consider a static solution when two junctions are identical as a simple limit case. (2.131) and (2.132) now become

$$\frac{i}{2} + j = \sin \delta_1, \quad \frac{i}{2} - j = \sin \delta_2. \quad (2.135)$$

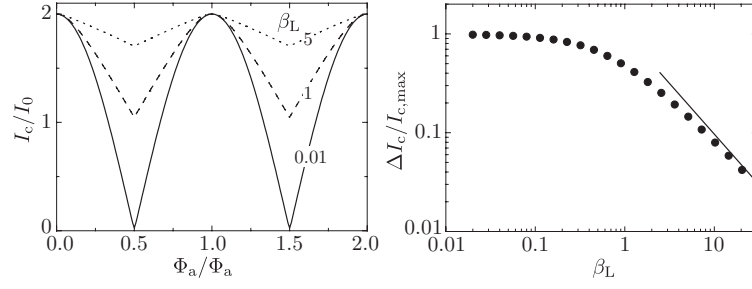


Fig. 2.15 Critical current of the dc SQUID vs. applied magnetic flux for various values of  $\beta_L$  (left) and the modulation depth vs.  $\beta_L$  (solid line is  $\beta_L^{-1}$ ) (right). Adapted from Clarke and Braginski [6].

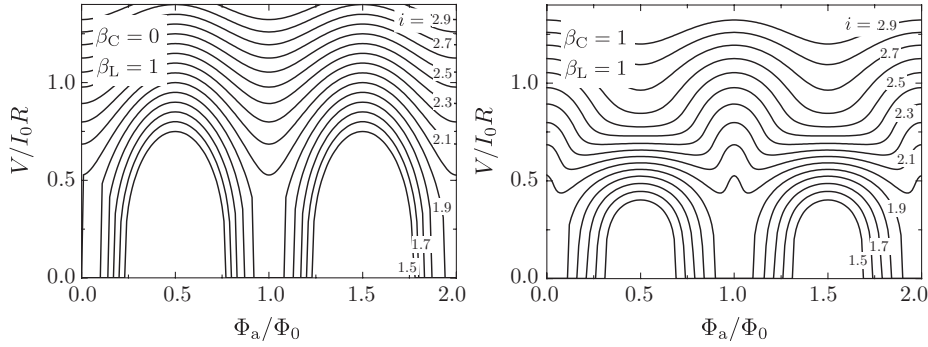


Fig. 2.16  $\Phi$ - $V$  characteristic:  $\beta_C = 0$  (left) and  $\beta_C = 1$  (right). Adapted from [6].

Moreover, when the self-inductance of the SQUID is negligible,  $\beta_L \ll 1$ , thus (2.133) becomes

$$\delta_2 - \delta_1 = 2\pi\phi_a. \quad (2.136)$$

We now have

$$i = \sin \delta_1 + \sin \delta_2 = \sin \delta_1 + \sin(\delta_1 + 2\pi\phi_a). \quad (2.137)$$

By defining  $\gamma \equiv \delta_1 + \pi\phi_a$ , we finally have

$$i = 2 \sin \gamma \cdot \cos(\pi\phi_a). \quad (2.138)$$

The critical current, which is the maximum super-current, is therefore  $i_c = 2|\cos(\pi\phi_a)|$  when normalized, or simply

$$I_c = 2I_0 \left| \cos \left( \pi \frac{\Phi_a}{\Phi_0} \right) \right|. \quad (2.139)$$

In this limit case, the critical current modulates from 0 to  $2I_0$ .

Practically, the self-inductance  $L$  can not be ignored.  $L$  reduces the modulation depth  $\Delta I_c/I_{c,\max}$  by  $1/(\beta_L + 1)$ . When the magnetic flux applied externally is  $\Phi_0/2$ , the required ring current to quantize the flux in the ring is the order of  $J = \Phi_0/2L$ . Then, the minimum critical current is the order of  $2(I_0 - J)$ , and  $\Delta I_c/I_{c,\max}$  is therefore

$$\Delta I_c/I_{c,\max} \approx \frac{I_{c,\max} - 2(I_0 - J)}{I_{c,\max}} = \frac{\Phi_0}{2LI_0} = \frac{1}{\beta_L}, \quad (2.140)$$

meaning that the modulation depth is reduced by  $1/\beta_L$ . Figure 2.15 shows the critical current modulation depth for various values of  $\beta_L$ .

We now consider the case of nonzero dc voltage across the junctions. We first consider the case when  $\beta_L \ll 1$ . Assuming two junctions are identical, (2.131) and (2.132) become

$$\frac{i}{2} + j = \sin \delta_1 + \dot{\delta}_1 + \beta_c \ddot{\delta}_1 \quad (2.141)$$

$$\frac{i}{2} - j = \sin \delta_2 + \dot{\delta}_2 + \beta_c \ddot{\delta}_2. \quad (2.142)$$

As  $\beta_L \ll 1$ , we obtain  $\dot{\delta}_1 = \dot{\delta}_2$  and

$$i = \sin \delta_1 + \sin(\delta_1 + 2\pi\phi_a) + 2\dot{\delta}_1 + 2\beta_c \ddot{\delta}_1 \quad (2.143)$$

from (2.133). For  $\gamma = \delta_1 + \pi\phi_a$ , we have  $i = 2(\cos \pi\phi_a \cdot \sin \gamma + \dot{\gamma} + \beta_c \ddot{\gamma})$ , or in general

$$I = 2I_0 \cos\left(\pi \frac{\Phi_a}{\Phi_0}\right) \sin \gamma + \frac{2\Phi_0}{2\pi R} \dot{\gamma} + \frac{2\Phi_0}{2\pi} C \ddot{\gamma}. \quad (2.144)$$

Figure 2.16 (left) shows the numerical simulation of the  $\Phi$ - $V$  characteristic at  $\beta_C = 0$  [6]. The above equation is equivalent to (2.110) if the resistance, the capacitance, and the critical current are substituted for  $R/2$ ,  $2C$ , and  $2I_0 \cos \pi\phi_a$ , respectively. In the limit of  $\beta_c \ll 1$ , the  $I$ - $V$  characteristic of dc SQUID for  $I > I_c$  is therefore

$$V = \frac{R}{2} \sqrt{I^2 - I_c^2}. \quad (2.145)$$

This means that the voltage across dc SQUID modulates periodically with a period of  $\Phi_0$  as an external magnetic flux is applied to the SQUID. Partially differentiating the above with a respect to  $\Phi_a$ , we have

$$\frac{\partial V}{\partial \Phi_a} = -2\pi \frac{I_0 R}{\Phi_0} \frac{I_0 \sin(\pi\Phi_a/\Phi_0) \cos(\pi\Phi_a/\Phi_0)}{\sqrt{I^2 - I_c^2}}. \quad (2.146)$$

It diverges at  $I = I_c$ , however, it converges when the noise is not negligible and the maximum will be around  $I = I_c$ . Let us now define the SQUID transfer function  $V_\Phi$  as

$$V_\Phi = \max\left(\left|\frac{\partial V}{\partial \Phi_a}\right|\right). \quad (2.147)$$

From (2.145) the peak-to-peak output voltage  $V_{pp}$  is

$$V_{pp} = V(\Phi_a = \Phi_0/2) - V(\Phi_a = 0) = I_0 R \left[ \frac{I}{2I_0} - \sqrt{\left(\frac{I}{2I_0}\right)^2 - 1} \right], \quad (2.148)$$

which takes its maximum value  $I_0 R$  when  $I = 2I_0$ .

When  $\beta_L$  can not be ignored, the critical current is reduced by  $1/(\beta_L + 1)$ , thus  $\partial V/\partial \Phi_{in}$  is reduced by

$$\frac{\partial V}{\partial \Phi_a} \propto \frac{1}{\beta_L + 1}, \quad (2.149)$$

and  $V_\Phi$  is also reduced by

$$V_\Phi \propto \frac{1}{\beta_L + 1}. \quad (2.150)$$

It does not mean that  $\beta_L = 0$  is the optimized SQUID. We will discuss it later, but  $\beta_L \approx 1$  will be the optimized

considering the effect of noise.

We finally see the effect of capacitance  $C$  to the SQUID transfer function. When the Josephson frequency  $f_J = \omega_c/2\pi = V/\Phi_0$  becomes the same level of the resonance frequency  $1/2\pi\sqrt{L(C/2)}$ , the effect of  $L$ - $C$  resonance can not be negligible. When  $\Phi_a = 0$ , the phases at two junctions match and it does not start oscillating. However, if they are out-of-phase, it starts oscillating. Once the oscillation occurred, the output voltage becomes smaller as the dc component of Josephson current becomes larger. As it works opposite to the transfer function, the SQUID output becomes smaller when  $\Phi_a = \Phi_0/2$ , which the output is supposed to be the maximum, while the output stays same when  $\Phi_a = 0$ . The  $\Phi$ - $V$  characteristic then becomes severely distorted as shown in Figure 2.16 (right).

### 2.3.6 Johnson-Nyquist Noise

The power spectral density  $S_V$  of Johnson noise at the shunt resistors of junctions can be given by

$$S_V = 4k_B T R, \quad (2.151)$$

and it causes fluctuations in the output voltage and the ring current. While there is no correlation between the output voltage and the ring current in the case of a non-superconducting ring ( $I_0 = 0$ ), in the SQUID there is a correlation between them since  $\delta J$ , the fluctuation of the ring current  $J$ , causes  $\delta\Phi$ , the fluctuation of the magnetic flux, and the output voltage  $V$  is the function of the flux.

If we normalize  $S_V$  using  $\omega_c = \tau^{-1} = 2\pi I_0 R / \Phi_0$  and  $V_c = I_0 R$ , we obtain

$$s_V = S_V \frac{\omega_c}{V_c^2} = 4\Gamma \quad (2.152)$$

with the noise parameter  $\Gamma$ .

Using the SQUID transfer function  $V_\Phi$ , the magnetic flux noise power  $S_\Phi$  is given by

$$S_\Phi = \frac{S_V}{V_\Phi^2}, \quad (2.153)$$

which is also one of the important figures of merit of SQUID.

With (2.140), (2.150) and the effect of  $\beta_C$  to  $\Phi$ - $V$  characteristic, a symmetric dc SQUID is now characterized by three parameters,  $\beta_C$ ,  $\beta_L$  and  $\Gamma$ . In the next section, we discuss the optimization of these parameters.

### 2.3.7 Optimization

Here we review the definitions of the three parameters:

$$\beta_C \equiv \frac{2\pi}{\Phi_0} I_0 R^2 C, \quad \beta_L \equiv \frac{2L I_0}{\Phi_0}, \quad \Gamma \equiv \frac{2\pi k_B T}{I_0 \Phi_0}. \quad (2.154)$$

It is obvious that the optimized  $\beta_C$  is  $\beta_C \ll 1$  considering undesirable effects of hysteretic junctions and the LC resonance at the superconducting ring. To suppress the thermal fluctuation, the noise parameter should be  $\Gamma \ll 1$ . A typical  $\Gamma$  at liquid helium temperature is

$$\Gamma = 0.018 \left( \frac{T}{4.2\text{K}} \right) \left( \frac{I_0}{10\mu\text{A}} \right)^{-1}, \quad (2.155)$$

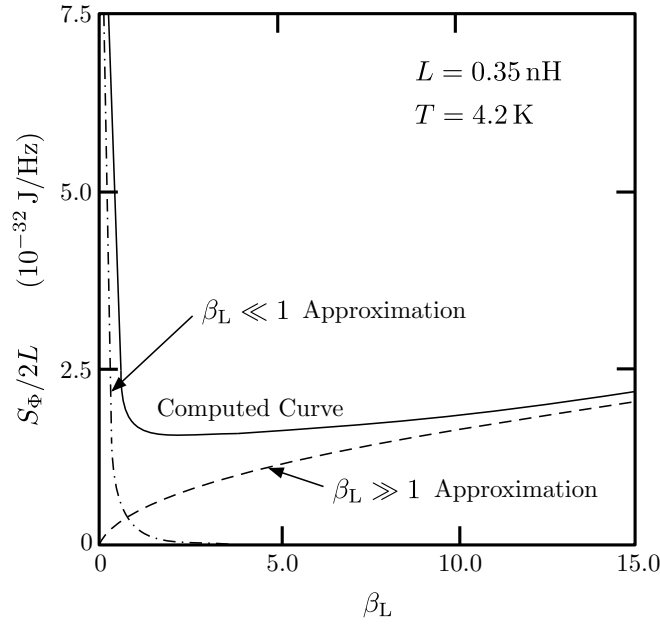


Fig. 2.17  $\beta_L$  optimization. Adapted from Tesche and Clarke [32].

which is already very small, so we may not need to worry about  $\Gamma$  at liquid helium temperature. At liquid nitrogen temperature,  $\Gamma$  becomes 18 time larger, and is generally not negligible.

As seen in (2.140) and (2.150),  $\beta_L$  reduces the output voltage, but  $\beta_L \ll 1$  is not preferable. Figure 2.17 shows the computed values of  $S_\Phi/2L$ , which is equivalent to the current noise, as the function of  $\beta_L$  [32]. At  $\beta_L \ll 1$ ,  $S_\Phi/2L$  takes a large value, and then takes the minimum value around  $\beta_L \approx 1$ , so the optimized value for  $\beta_L$  is  $\beta_L \approx 1$ .

To summarize, the optimized values for  $\beta_C$ ,  $\beta_L$  and  $\Gamma$  are

$$\beta_C \ll 1, \quad \beta_L \approx 1, \quad \Gamma \ll 1. \quad (2.156)$$

### 2.3.8 Numerical Analysis and Approximate Solutions for dc SQUID

Equations from (2.131) to (2.133) are numerically analyzed in order to discuss the SQUID performance.

The transfer function  $V_\Phi$ , the voltage noise power spectral density  $S_V$ , and the magnetic flux noise power spectral density  $S_\Phi$  at the operating point  $I \approx 1.6I_0$  and  $\Phi_a = 0.25\Phi_0$ , at which the SQUID gain is maximum, for the optimized SQUID,  $\beta_C \ll 1$ ,  $\beta_L \approx 1$ , and  $\Gamma = 0.05$ , are approximated as

$$V_\Phi \approx \frac{R}{L}, \quad (2.157)$$

$$S_V \approx 16k_B T R, \quad (2.158)$$

$$S_\Phi \approx \frac{16k_B T L^2}{R} \quad (2.159)$$

[4, 5, 34, 28].

The above approximations do not hold on the SQUID at liquid nitrogen temperature. In this case the gener-

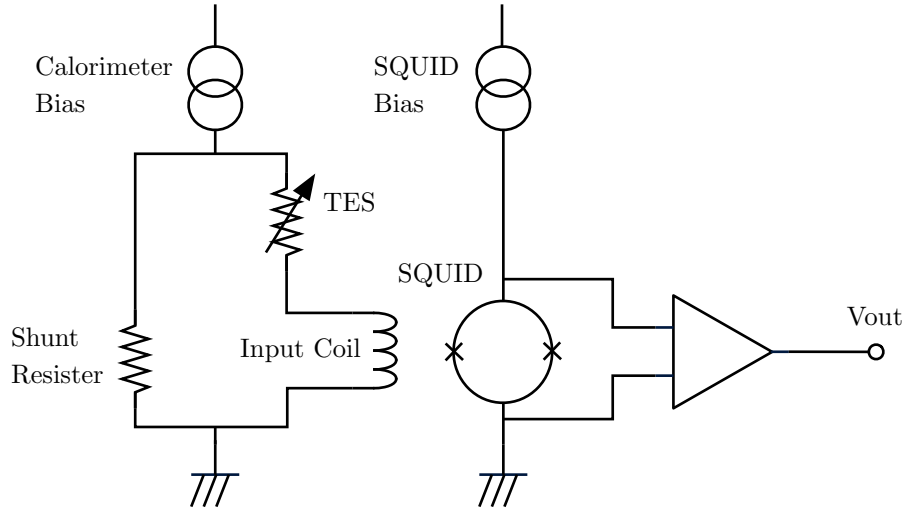


Fig. 2.18 TES readout using SQUID

alized approximations [10, 9] below are often used:

$$V_{\Phi} = \frac{4I_0 R}{\Phi_0(1 + \beta_L)} \exp\left(-\frac{3.5\pi^2(\delta\Phi_n)^2}{\Phi_0^2}\right) = \frac{4I_0 R}{\Phi_0(1 + \beta_L)} \exp(-2.75\Gamma\beta_L) \quad (2.160)$$

$$S_{\Phi} = \alpha L^2 \left(\frac{2k_B T}{R}\right) \left[1 + \left(\frac{R}{LV_{\Phi}}\right)^2\right] \quad (2.161)$$

$(\delta\Phi_n)^2 = k_B T L$  is the mean square of the magnetic flux noise, and  $\alpha = 1 + \exp(1.23 - 4.82\Gamma)$ .

The dynamic resistance  $R_{\text{dyn}}$  is approximated as

$$R_{\text{dyn}} = \frac{R}{\sqrt{2}} \quad (2.162)$$

from the numerical analysis of the  $\Phi$ - $V$  characteristic [6].

### 2.3.9 TES Readout with SQUID

To read a current change of TES in the voltage-biasing mode, one needs an ammeter. Since the TES current is as small as  $\sim 100 \mu\text{A}$ , and the TES impedance is as small as tens of milliohms, it needs to have a resolution of microamps and a low input impedance of milliohms. It should also have a low equivalent input noise, preferably less than  $20 \text{ pA}/\sqrt{\text{Hz}}$ , which is the typical TES current noise. This makes no other choice than the SQUID for the ammeter. Figure 2.18 shows the schematic diagram of TES readout circuit using the SQUID. The current from TES is converted to a magnetic flux through an input coil, which is around tens of pH to a few nH, and then is converted to a voltage that can be read by ordinary voltmeters. In this way the SQUID is used as a current to voltage converter, or a transimpedance amplifier.

Using the mutual-inductance  $M_{\text{in}}$  between the input coil and the SQUID superconducting ring, the current to voltage transfer function of SQUID, namely the transimpedance gain  $Z_{\text{tran}}$ , is given by

$$Z_{\text{tran}} = M_{\text{in}} V_{\Phi}. \quad (2.163)$$

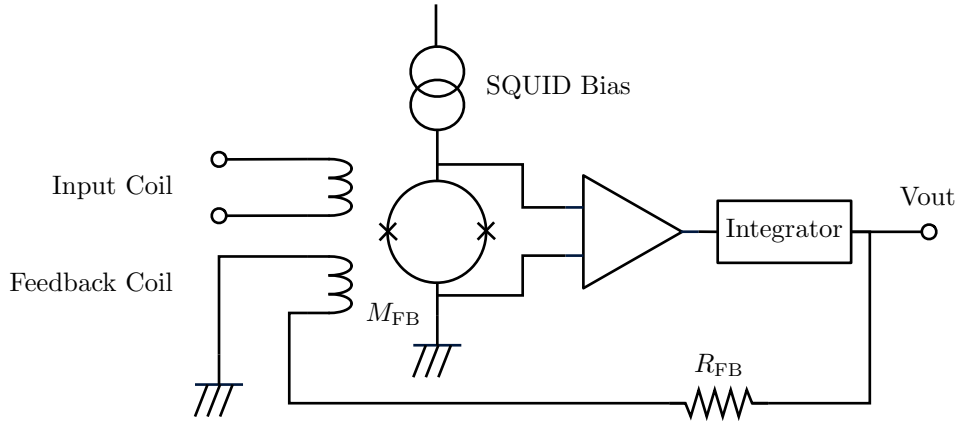


Fig. 2.19 The schematic diagram of Flux-Locked Loop (FLL)

Using the above, the equivalent input current noise of SQUID,  $I_N$ , is then given by

$$I_N = \frac{\sqrt{S_V}}{Z_{\text{tran}}} = \frac{\sqrt{S_\Phi}}{M_{\text{in}}}. \quad (2.164)$$

### 2.3.10 Flux-Locked Loop

Since the SQUID has a periodic response, the transfer function largely vary depend on the operating point. Moreover, the SQUID output turns around for a large input, which makes difficult to use as an ordinary amplifier. For that reason the SQUID is generally used with a negative feedback. The feedback keeps the flux through the SQUID ring constant, and is therefore called a flux-locked loop (FLL). In FLL, the SQUID output is fed back to a feedback coil, which is coupled magnetically with the SQUID superconducting ring, through a feedback resistor (Figure 2.19).

In this case the feedback factor  $b$  is given by

$$b = \frac{\Phi_{\text{FB}}}{V_{\text{out}}} = \frac{M_{\text{FB}}}{R_{\text{FB}}}, \quad (2.165)$$

and the overall gain of the FLL circuit becomes  $1/b = R_{\text{FB}}/M_{\text{FB}}$ , where  $R_{\text{FB}}$  is the feedback resistance and  $M_{\text{FB}}$  is the mutual-inductance between the feedback coil and the superconducting ring. The magnetic flux  $\Phi_{\text{in}}$  that the input current  $I_{\text{in}}$  generates is

$$\Phi_{\text{in}} = M_{\text{in}} I_{\text{in}} \quad (2.166)$$

using  $M_{\text{in}}$ , the mutual-inductance between the input coil and the superconducting ring. The (current-to-voltage) transfer function  $\Xi$  in the FLL circuit is then given by

$$\Xi = \frac{M_{\text{in}}}{M_{\text{FB}}} R_{\text{FB}}. \quad (2.167)$$

### 2.3.11 SQUID Array

By joining multiple SQUID in series and having them work in phase, one can have an increased SQUID output. It is called a SQUID series array. The series SQUID array tends to have a large output impedance, so one may

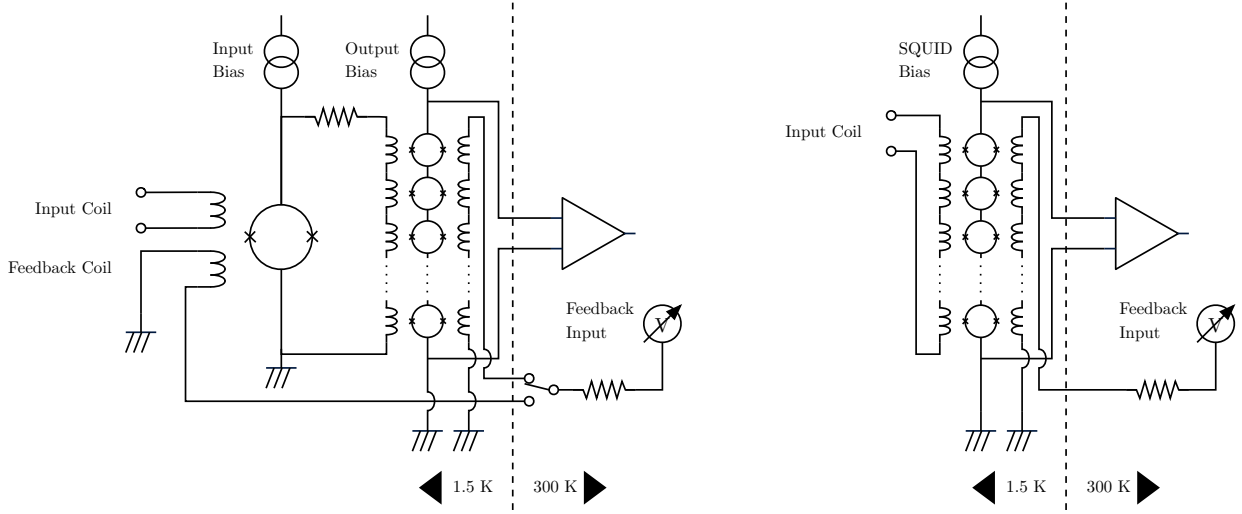


Fig. 2.20 The TES readout using the SQUID array: the two-staged SQUID (left), and the SQUID series array (right)

have to parallelize the series SQUID array to reduce the impedance.

Let us consider a SQUID array with  $n$  series and  $m$  parallel. With the single SQUID transfer function  $V_\Phi$ , the voltage noise power spectral density  $S_V$ , the magnetic flux noise power spectral density  $S_\Phi$ , and the dynamic resistance  $R_{\text{dyn}}$ , we have the SQUID array transfer function  $\mathcal{V}_\Phi$ , the voltage noise spectral density  $\mathcal{S}_V$ , the magnetic flux noise power spectral density  $\mathcal{S}_\Phi$ , and the dynamic resistance  $\mathcal{R}_{\text{dyn}}$  as

$$\mathcal{V}_\Phi = nV_\Phi, \quad (2.168)$$

$$\mathcal{S}_V = \frac{n}{m} S_V, \quad (2.169)$$

$$\mathcal{S}_\Phi = \frac{\mathcal{S}_V}{\mathcal{V}_\Phi^2} = \frac{S_\Phi}{nm}, \quad (2.170)$$

and

$$\mathcal{R}_{\text{dyn}} = \frac{n}{m} R_{\text{dyn}}, \quad (2.171)$$

respectively. From  $Z_{\text{tran}} = M_{\text{in}} V_\Phi$ , we thus have the SQUID array transimpedance gain  $\mathcal{Z}_{\text{tran}}$  as

$$\mathcal{Z}_{\text{tran}} = M_{\text{in}} \mathcal{V}_\Phi = nM_{\text{in}} V_\Phi. \quad (2.172)$$

The SQUID output becomes  $n$  time larger in the series array. The voltage noise also becomes  $n$  time larger in the series array, but  $m$  time smaller in the parallel array. The equivalent input current noise  $\mathcal{I}_N$  in the array now becomes

$$\mathcal{I}_N = \frac{\sqrt{\mathcal{S}_V}}{\mathcal{Z}_{\text{tran}}} = \sqrt{\frac{1}{nm}} I_N, \quad (2.173)$$

which is reduced by  $\sqrt{1/nm}$ . Therefore, as the number of SQUID increases either in series or in parallel, the overall noise level decreases and the signal-to-noise ratio increases. This is a huge advantage of the SQUID array. The number of SQUID in array can be as many as tens or hundreds.

There are generally two types of amplifiers using the SQUID array; one is a two-staged SQUID amplifier shown in Figure 2.20 (left), and the other is a single-stage SQUID series amplifier shown in Figure 2.20 (right). The

former is called the TSS (two-staged SQUID) amplifier, and the later is called the SSA (series SQUID array) amplifier.

### 2.3.12 Joule Heating

The SQUID at the operating point generates heat. The heat is Joule heating at the shunt resistors of junctions, and the maximum heat  $P$  is

$$P = VI = 2RI_0^2 \quad (2.174)$$

at  $I = 2I_0$  and  $V = I_0R$ , at which the SQUID output becomes maximum. The Joule heating for the SQUID array  $\mathcal{P}$  with  $n$  series and  $m$  parallel is the sum of Joule heating of each SQUID as

$$\mathcal{P} = nmP. \quad (2.175)$$

### 2.3.13 Bandwidth

Because the SQUID voltage output is the periodic function with a period of  $\Phi_0$ , a flux input exceeding roughly  $\pm 1/4\Phi_0$  causes a  $\Phi_0$  jump of the operating point, which is called a flux jump. The maximum flux input  $\Phi_{\max}$  into SQUID without flux-jumping is given by

$$\frac{1}{1 + \mathcal{L}(\omega)} |\Phi_{\max}| < \frac{1}{4}\Phi_0, \quad (2.176)$$

where  $\mathcal{L}(\omega)$  is the loopgain of FLL.

### 2.3.14 SQUID Noise Contribution to Energy Resolution

The NEP of the SQUID is given by

$$\text{NEP}_{\text{readout}}^2 = \frac{i_n^2}{S_I^2}, \quad (2.177)$$

where  $i_n$  is the noise current spectral density of SQUID. The contribution of the SQUID noise to the energy resolution is thus

$$\Delta E_{\text{FWHM}} = 2.35 \left( \int_0^\infty \frac{4df}{\text{NEP}_{\text{readout}}^2(f)} \right)^{-\frac{1}{2}} \quad (2.178)$$

$$= 2.35 \frac{\mathcal{L}_0 + 1}{\mathcal{L}_0} |b| i_n \sqrt{\tau_{\text{eff}}} \quad (2.179)$$

$$= 2.35 \frac{\mathcal{L}_0 + 1}{\mathcal{L}_0} V_b i_n \sqrt{\tau_{\text{eff}}} \quad (2.180)$$

using (2.88). Therefore, for the case of  $\mathcal{L}_0 \gg 1$ , it is

$$\Delta E_{\text{FWHM}} \sim 2.35 V_b i_n \sqrt{\tau_{\text{eff}}}. \quad (2.181)$$

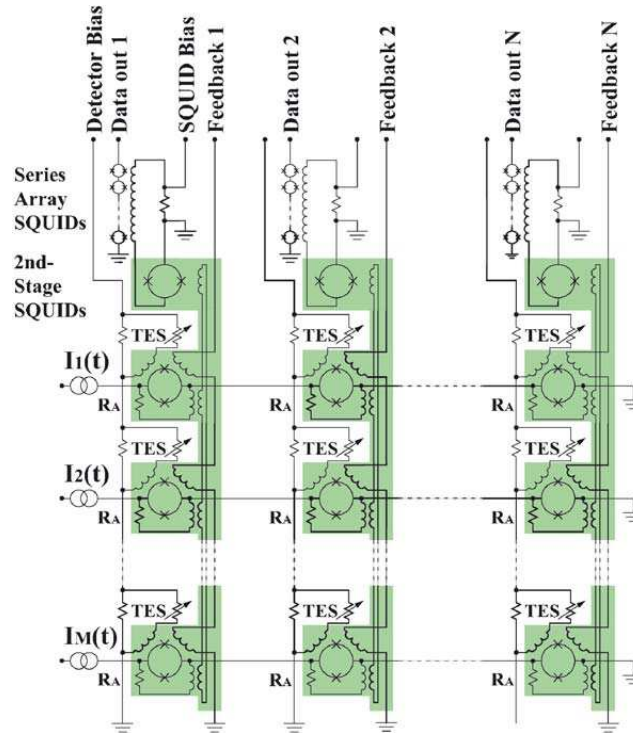


Fig. 2.21 The schematic diagram of the SQUID TDM architecture. Adapted from Irwin et al. [18].

### 2.3.15 SQUID Multiplexing

To readout a TES using a single SQUID, we generally need 4 pairs of electrical wires; one pair for TES biasing, one for a SQUID feedback, one for SQUID biasing, and one for a SQUID output. As the number of TES increases, the required number of SQUID increases, meaning the required number of electrical wires also increases, which finally causes a non-negligible heat flow from a higher temperature stage to a cryogenic stage. Therefore, the maximum number of SQUID that can be placed at a cryogenic stage is generally limited by a cooling power for the stage, and is typically less than 100 even by optimistic estimates. For readout of more than hundreds of TES, SQUID multiplexing is mandatory.

The methods of SQUID multiplexing are divided into several types: time-division multiplexing (TDM), code-division multiplexing (CDM), and frequency-division multiplexing (FDM).

#### Time-Division Multiplexing

In TDM, each TES signal is connected to each SQUID, and SQUIDs are turned on one at a time. For example, Figure 2.21 shows the schematic diagram of TDM developed by Irwin et al. [18]. Each TES is coupled to each SQUID, which is shunted with an address resistor and a coil coupled to a summing coil that connects all of the SQUIDs in a column. The summing coil is then coupled to a single second-stage SQUID, and the output of the second-stage SQUID is finally coupled to a third-stage SQUID array at a higher temperature. Address currents,  $I_M(t)$ , are turned on one row at a time. By switching address currents far faster than a time constant of TES, one can readout multiple TES signals with a single (column of) SQUID.

Although one can theoretically multiplex any number of signals with TDM as long as SQUIDs are switched fast enough, it also increases the noise because of SQUID noise aliasing [16]. If the number of multiplexing is  $N$ ,

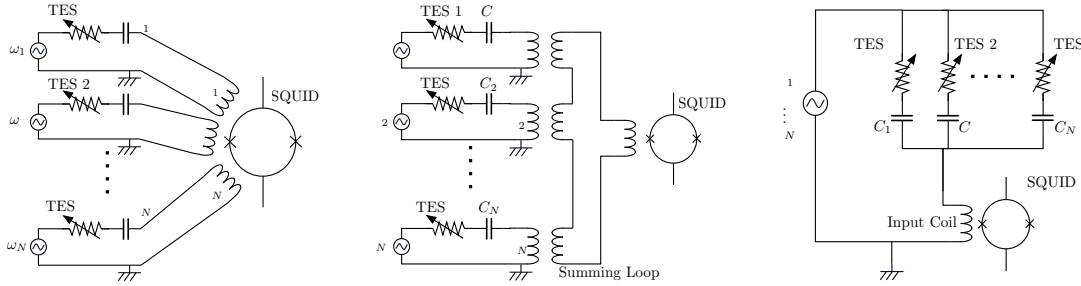


Fig. 2.22 Signal summing methods in FDM: flux summing (left), voltage summing (middle), and current summing (right)

then the effective noise power of SQUID is increased by a factor of  $N$ . In order to keep the signal-to-noise ratio (SNR) of a non-multiplexed case, the SQUID gain needs to be  $N$  times larger, making it difficult to increase the number of multiplexing.

#### Code-Division Multiplexing

CDM is an enhanced version of TDM. In CDM, SQUIDS are not turned on/off but switched polarity, or modulated, according to the Walsh code. In contrast to TDM, all the TES are biased all the time in CDM. As a result, both the effective signal power and the effective noise power are increased by a factor of  $N$ , and the SNR is thus maintained. Moreover, all signals except the unmodulated channel are moved to higher signal bands of modulation frequencies, and the demodulated signals are free of low-frequency noises, such as  $1/f$  noise and power line noise. Therefore, the modulated channels usually exhibit better energy resolutions than the unmodulated channel.

As the cryogenic system of CDM is identical to that of TDM, CDM is used as a better replacement of TDM. Therefore, CDM is adopted by groups that developed TDM. For example, NIST has achieved 2.6 eV FWHM at 5.9 keV multiplexing 8 channels [11].

#### Frequency-Division Multiplexing

In FDM, TES are AC-biased in different frequencies, and their signals are summed, or modulated, at a single SQUID (or SQUID array). The modulated signals are demodulated at a room-temperature electronics to retrieve TES signals of each channel. Biasing frequencies need to be faster than the thermal diffusion time constant and are generally several MHz. In this method a single SQUID is only used, and there is no noise aliasing nor an addition of multiple SQUID noises. Consequently, the SNR is maintained as in a non-multiplexed case. Moreover, all signals are moved to higher signal bands, as in CDM, and demodulated signals are also free of low-frequency noises. In FDM, the required number of SQUID is less than that in TDM and CDM, and the cryogenic stage is therefore rather simpler, although band-pass filters with different passbands are required for each TES. One disadvantage in FDM is that a large slew rate and a large dynamic range are required to SQUID since the input to SQUID is larger than TES signals as TES are AC-biased with amplitudes evidently more than amplitudes of TES signals.

FDM can be further divided into three types by its signal summing methods: flux summing, voltage summing (or summing loop), and current summing. In flux summing, signals are converted to flux then summed at a SQUID input (Figure 2.22 left). Owing to spatial limitations of multiple input coils and a SQUID washer, the number of multiplexing is limited. In voltage summing, signals are summed using a superconducting inductance loop called a summing loop (Figure 2.22 middle). It has been developed by a group of UCB and LLNL [7]. In current summing, signals are summed directly at a SQUID input (Figure 2.22 right). It is the simplest method, but has a disadvantage that a signal from a TES may go to other signal lines, which causes signal cross talks,

due to a non-zero common impedance at a summing point. However, the input impedance is mostly nulled with FLL, and cross talks due to the common impedance is generally negligible. This method is widely adopted including TES bolometer FDM readouts [e.g. 14, 13, 8] as well as TES X-ray FDM readouts [e.g. 33]. We developed the 8-input flux-summing SQUID before, but we now have also moved to current-summing SQUIDS.

#### Comparison of Multiplexing Types

CDM and FDM share most of benefits, and can be good candidates for practical TES multiplexing applications. However, there is one non-negligible disadvantage in CDM especially for space missions. In CDM, TES bias lines can not be multiplexed, and the required number of wires in CDM is larger than that in FDM, which makes the required cooling power of cryogenic stage larger in CDM. It is critical disadvantage for space missions where resources are very limited. Therefore, FDM is generally the only choice to multiplex large-format TES arrays in space missions.

## Chapter 3

# Development of Low-Power SQUIDs

### 3.1 Requirements for SQUIDs

DIOS is planned to carry a 256- to 400-pixel TES array to carry out the WHIM mapping. To readout the 256-pixel TES array multiplexed by, for instance, 8, we need at least 32 SQUIDs. The maximum heat allowance at the cryogenic stage of the DIOS adiabatic demagnetization refrigerator (ADR) is 640 nW, which makes the maximum heat dissipation of a single SQUID to be 20 nW or less. For two-staged configurations, the SQUID at the first stage is usually a single non-arrayed SQUID (or a very small number SQUID array) and this requirement can easily be fulfilled. However, for single-staged configurations, the single SQUID needs to amplify the signal from TES usually up to 100 times or more, causing a lot of heat dissipation, which makes it very challenging to place it at the resource-limited cryogenic stage. Typical noise levels of TES and low-noise amp at room temperature are  $20 \text{ pA}/\sqrt{\text{Hz}}$  and  $1 \text{ nV}/\sqrt{\text{Hz}}$  respectively, which make an absolute minimum SQUID gain of  $50 \text{ V/A}$  (or  $50 \Omega$ ) or more, and the equivalent input current noise to be less than  $20 \text{ pA}/\sqrt{\text{Hz}}$ . To realize a single-staged SQUID readout, one needs an unprecedented low-power SQUID with an adequate gain.

Besides, to multiplex TES signals, which typical bandwidth is  $\lesssim 100 \text{ kHz}$ , in frequency domain, the TES and SQUID are AC-biased to up to several MHz, so they need to be optimized for operations in the MHz band. The wires between the cryogenic stage and room temperature electronics typically have some parasitic capacitance of  $\sim 100 \text{ pF}$  or more, which attenuates the SQUID output and decreases the effective SQUID gain. Assuming the parasitic capacitance of  $100 \text{ pF}$  and the cut off frequency of  $6 \text{ MHz}^{\ast 1}$ , the output resistance becomes  $250 \Omega$ . The wires also have some resistance of  $\sim 100 \Omega$ . Therefore, the output impedance of SQUID is preferred to be  $150 \Omega$  or less.

These design goals are summarized in Table 3.1 along with the minimum requirements if those are unfeasible. For the input current noise and the transimpedance gain, the design goals are halved (doubled for the gain) from the minimum requirement for an extra margin. The minimum requirement for the power dissipation is set to  $< 32 \text{ nW}$ , which makes the total power dissipation  $< 1 \mu\text{W}$  for 32 SQUIDs. The minimum requirement for the output impedance is simply a double of the design goal, which makes the cut off frequency  $\sim 4 \text{ MHz}$ .

Table 3.1 Design targets of low-power SQUIDs

		Goal	Requirement
Thermal power dissipation (nW)	$P$	$< 20$	$< 32$
Equivalent input current noise @ 4 K ( $\text{pA}/\sqrt{\text{Hz}}$ )	$I_N$	$< 10$	$< 20$
Transimpedance gain ( $\text{V/A}$ or $\Omega$ )	$Z_{\text{tran}}$	$> 100$	$> 50$
Output impedance ( $\Omega$ )	$Z_{\text{out}}$	$< 150$	$< 300$

<sup>$\ast 1$</sup>  It is equivalent to the required bandwidth for 16-channel multiplexing described in Section 4.2.

Table 3.2 Design parameters of ISAS-A10, ISAS-B10, ISAS-C10, and new ISAS-G15

		ISAS-A10/C10	ISAS-B10	ISAS-G15
Junction critical current ( $\mu\text{A}$ )	$I_0$	10	10	8
Junction shunt resistance ( $\Omega$ )	$R$	10	15	10
SQUID washer self-inductance (pH)	$L$	100	100	120
Input coil self-inductance (pH)	$L_{\text{in}}$	100	100	120
Input coil mutual-inductance (pH)	$M_{\text{in}}$	75	75	90
Number of SQUIDs in series	$n$	10	10	15

Table 3.3 Design targets and actual results of ISAS-A10, ISAS-B10 and ISAS-C10

		Goal	Requirement	Actual Results		
				A10	B10	C10
Thermal power dissipation (nW)	$P$	$< 20$	$< 32$	21	33	26
Equivalent input current noise @ 4K ( $\text{pA}/\sqrt{\text{Hz}}$ )	$I_N$	$< 10$	$< 20$	8	10	8
Transimpedance gain (V/A or $\Omega$ )	$Z_{\text{tran}}$	$> 100$	$> 50$	87	115	87
Output impedance ( $\Omega$ )	$Z_{\text{out}}$	$< 150$	$< 300$	96	141	103

## 3.2 Parameter Optimizations and SQUID Designs

### 3.2.1 Parameter Optimizations

As the gain of the SQUID becomes larger, the SQUID becomes hotter, meaning that a development of a cooler yet higher-gain SQUID is challenging. To build such low power SQUIDS with sufficient gains, we took following approach. The heat dissipation  $P$  and the transimpedance gain  $Z_{\text{tran}}$  are given by

$$P = 2nRI_0^2 \quad \text{and} \quad Z_{\text{tran}} \propto nRI_0M_{\text{in}}, \quad (3.1)$$

where  $R$  is a junction shunt resistance,  $I_0$  is the junction critical current,  $n$  is the number of SQUIDs in series, and  $M_{\text{in}}$  is a mutual-inductance of the SQUID washer and the input coil. Using these, the transimpedance gain per unit power,  $Z_{\text{tran}}/P$ , is given by

$$Z_{\text{tran}}/P \propto M_{\text{in}}/I_0. \quad (3.2)$$

To maximize the gain per unit power, we can increase the mutual inductance, or decrease the critical current. However, the former limits the input dynamic range, and the latter makes the noise larger. As we place SQUIDS at the cryogenic stage which temperature is  $\sim 100$  mK, the SQUID equivalent input current noise, which is proportional to the temperature, tends to be smaller. Therefore, the latter approach is more feasible.

We have so far developed several types of low-power SQUIDS by decreasing the junction critical current, but none of them fully satisfied the requirement [29]. Table 3.2 shows the design parameters for low-power SQUIDS, ISAS-A10, ISAS-B10, and ISAS-C10. The junction critical current is  $10 \mu\text{A}$  for all types. They also share most of the design parameters. The difference is the shunt resistance: ISAS-A10 and ISAS-C10 have  $10 \Omega$  resistance, while ISAS-B10 has  $15 \Omega$  resistance. ISAS-C10 is gradiometer type of ISAS-A10. Table 3.3 shows the measurement results of those SQUIDS. ISAS-A10 is sufficiently low-power, but has an insufficient gain. ISAS-B10 has a sufficient gain, but is slightly hotter.

To develop a low-power SQUID with a sufficient gain, we further decreased the critical current to  $8 \mu\text{A}$ . Table 3.2 also shows the design parameters of a new ISAS-G15, which is a series array of 15 ISAS-G. Compared to ISAS-A10/C10, ISAS-G15 has slightly larger SQUID washer and input coil self-inductances, making the mutual-

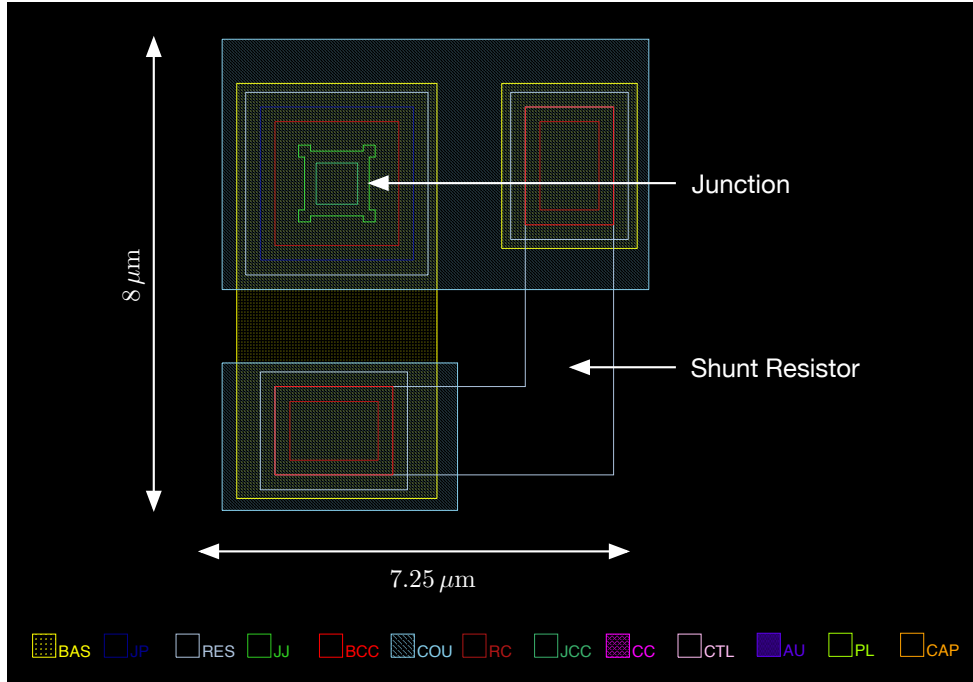


Fig. 3.1 The design of the junction and shunt resistor part

inductance also slightly larger. As the heat dissipation of single SQUID is decreased due to the smaller critical current, the number of SQUIDs in series is increased to 15, but the heat dissipation is to be still under 20 nW. For other parameters, we have followed the SQUID optimization rule (2.156).

### 3.2.2 SQUID Designs

For the layout design we used Xic (Version 3.2) developed by Whiteley Research Inc. SQUIDs were fabricated in the Clean Room for Analog & Digital superconductIVITY (CRAVITY) at National Institute of Advanced Industrial Science and Technology (AIST), in accordance with the SRL Nb Standard Process (STD3). See Appendix A for the detail of the design parameter and rule in STD3.

Figure 3.1 shows the junction and shunt resistor part of ISAS-G15. The critical current density,  $1 \text{ kA/cm}^2$ , and the junction design size including the shrink of junctions,  $1.1 \mu\text{m} \times 1.1 \mu\text{m}$ , make the critical current to be  $8.1 \mu\text{A}$ . The shunt resistor is bypassing the junction with  $10 \Omega$  resistance.

Figure 3.2 shows the design of ISAS-G, a Ketchen-type [19] SQUID with a single-turn input coil and a single-turn feedback coil, and Figure 3.3 shows the design of ISAS-G15.

Finally, Figure 3.4 shows the design of a  $2.5 \text{ mm} \times 2.5 \text{ mm}$  ISAS-G15 chip. It is equipped with two sets of ISAS-G15 with  $5 \text{ m}\Omega$  TES shunt resistors, and a  $15 \text{ k}\Omega$  SQUID heater for a removal of trapped flux. The TES shunt resistor is an interdigitated electrode array in shape to produce a very small resistance from the  $2.4 \Omega$  sheet resistance.

### 3.2.3 Multi-Input Current-Summing SQUID

We also designed a 4-input current-summing SQUID for FDM. Figure 3.5 (left) shows the design of a 4-input ISAS-G15 chip with inductors. It is equipped with a ISAS-G15, a  $5 \text{ m}\Omega$  TES shunt resistor, a  $15 \text{ k}\Omega$  SQUID heater, and four  $500 \text{ nH}$  inductors. Figure 3.5 (right) shows the design of a 4-input extension chip with inductors. It is

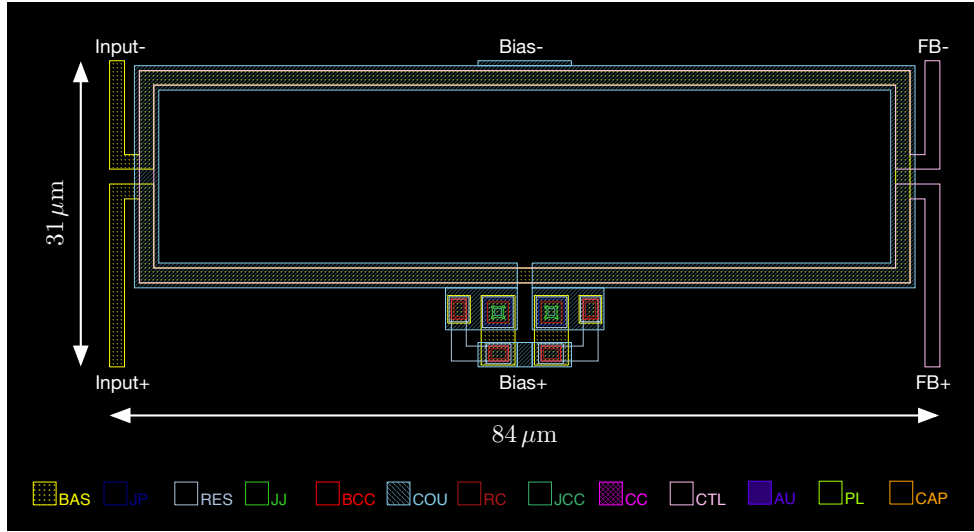


Fig. 3.2 The design of ISAS-G

Table 3.4 Inductances, capacitances and resonance frequencies of the LC filters on the 4-input current-summing SQUID and the 4-input extension chips

Inductance (nH)	Area (mm <sup>2</sup> )	Capacitance (nF)	Resonance Frequency (MHz)
4-input current-summing SQUID			
500	0.358	3.2	4.0
	0.316	2.8	4.3
	0.283	2.5	4.5
	0.253	2.2	4.8
4-input extension			
500	0.636	5.6	3.0
	0.528	4.7	3.3
	0.468	4.1	3.5
	0.408	3.6	3.8

equipped with four 500 nH inductors, which can be connected to the former SQUID chip to expand multiplexing channel up to 8. Figure 3.6 shows the equivalent circuit for those chips. Each TES channel is separated each other by a LC bandpass filter serially inserted to TES, and signals from each TES are summed right before the SQUID input coil. The capacitors for the filters are attached externally.

Externally attached capacitors for the LC filter are usually SMD multilayer ceramic capacitors. To design MHz-band bandpass filters using on-chip 500 nH inductors, we need several nF capacitors. The typical size of those capacitors is usually 1608 (0603) or larger, which is almost the same size as the SQUID chip. To save precious cryogenic stage space, those capacitors should be also on chip. Thus, we designed a 4-input current-summing SQUID with built-in LC filters for FDM. Figure 3.7 shows the design of the chip along with an extension chip with built-in LC filters, and Figure 3.8 shows the equivalent circuit for those chips. The capacitors are simple parallel-plate capacitors. The dielectric is the JP (JJ protection) layer, which is a 10 nm thick anodic aluminum oxide film, and the relative permittivity is 8–10. Therefore, a 0.1 mm<sup>2</sup> sized capacitor will have  $\sim 1$  nF in capacity. We summarized capacitances and resonance frequencies of the filters in Table 3.4.

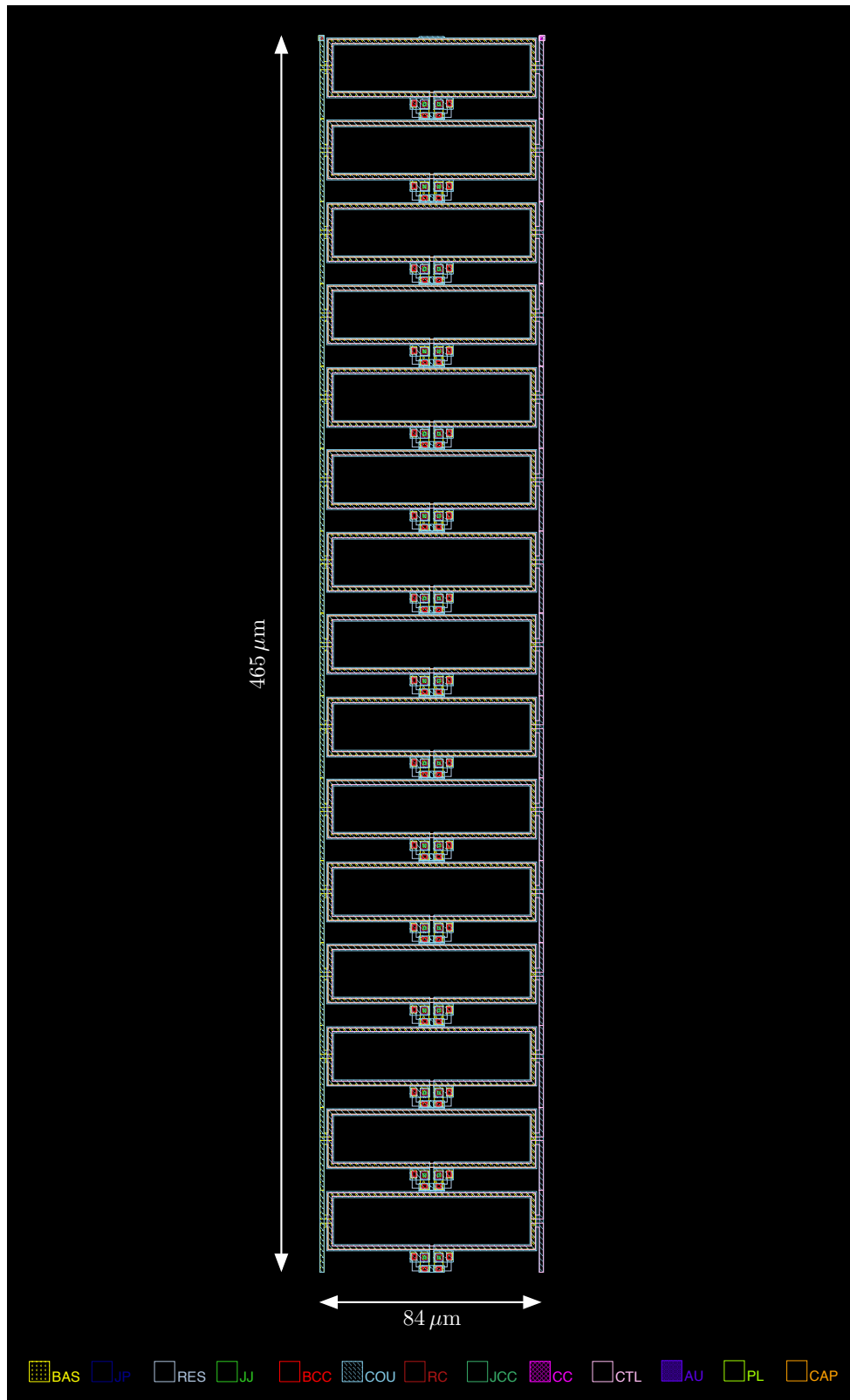


Fig. 3.3 The design of ISAS-G15

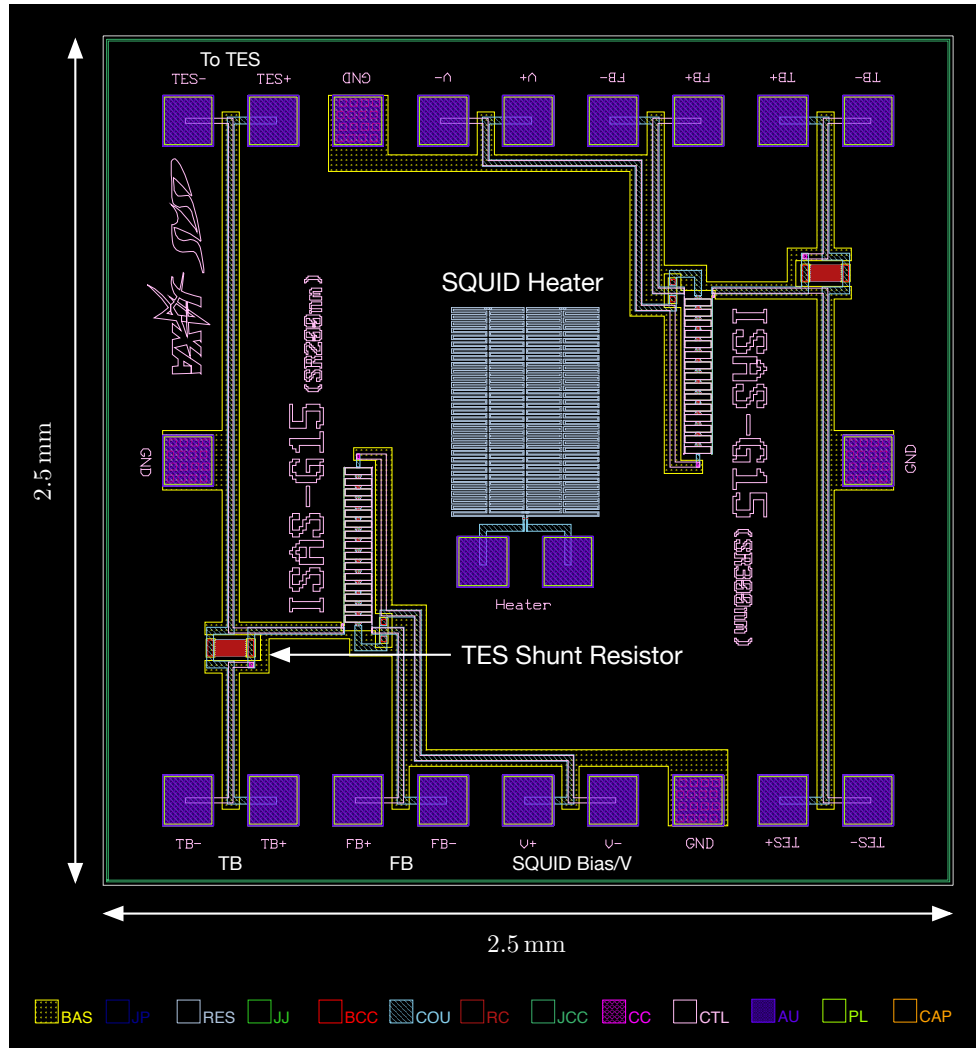


Fig. 3.4 The design of the ISAS-G15 chip

### 3.3 Measurements

All the SQUIDS were fabricated in the CRAVITY at AIST. Figure 3.9 shows photomicrographs of the fabricated ISAS-G15 chip. Figure 3.10 shows the photomicrographs of the 4-input current-summing SQUID chip with inductors, a zoomed 500 nH inductor, and a zoomed current-summing point. All the TES signal lines are paired on the chip, and only broken at the summing-point to sum those signals and put into the input coil. Figure 3.11 shows the photomicrographs of the fabricated 4-input current-summing SQUID chip with built-in LC filters, and its current-summing point. The TES signals are summed in the same manner. Finally Figure 3.12 shows the photomicrographs of the 4-input extension chip with inductors, and the 4-input extension chip with built-in filters.

The  $\Phi$ - $V$  characteristic was first measured for the fabricated ISAS-G15 in 4 K. From the measurement, we can derive most of the figures of merit except the noise. The noise characteristic and the filter characteristics were then measured also in 4 K.



Fig. 3.5 The designs of the 4-input ISAS-G15 chip with inductors (left) and the 4-input extension chip with inductors (right)

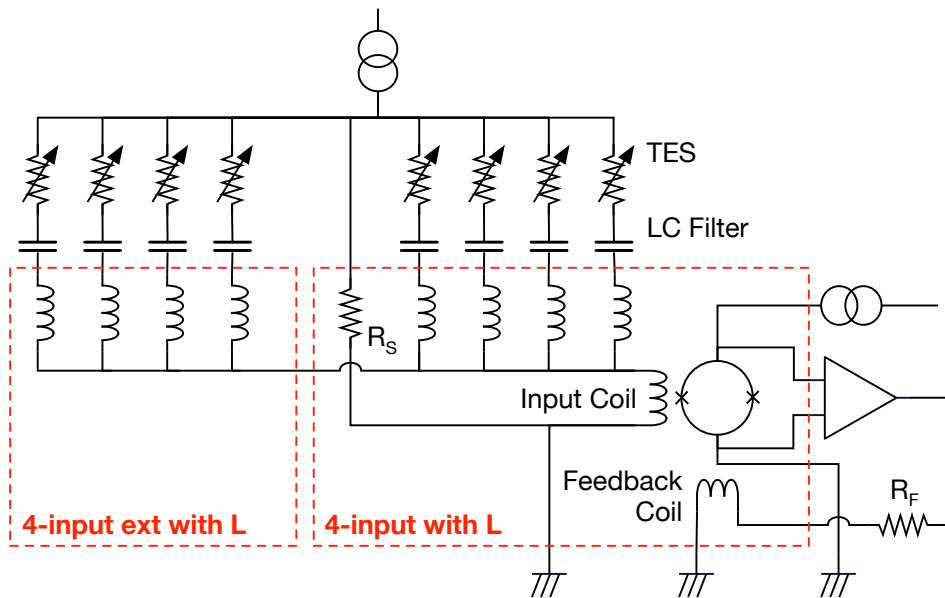


Fig. 3.6 Equivalent circuits for the 4-input SQUID chip with inductors and the 4-input extension chip with inductors

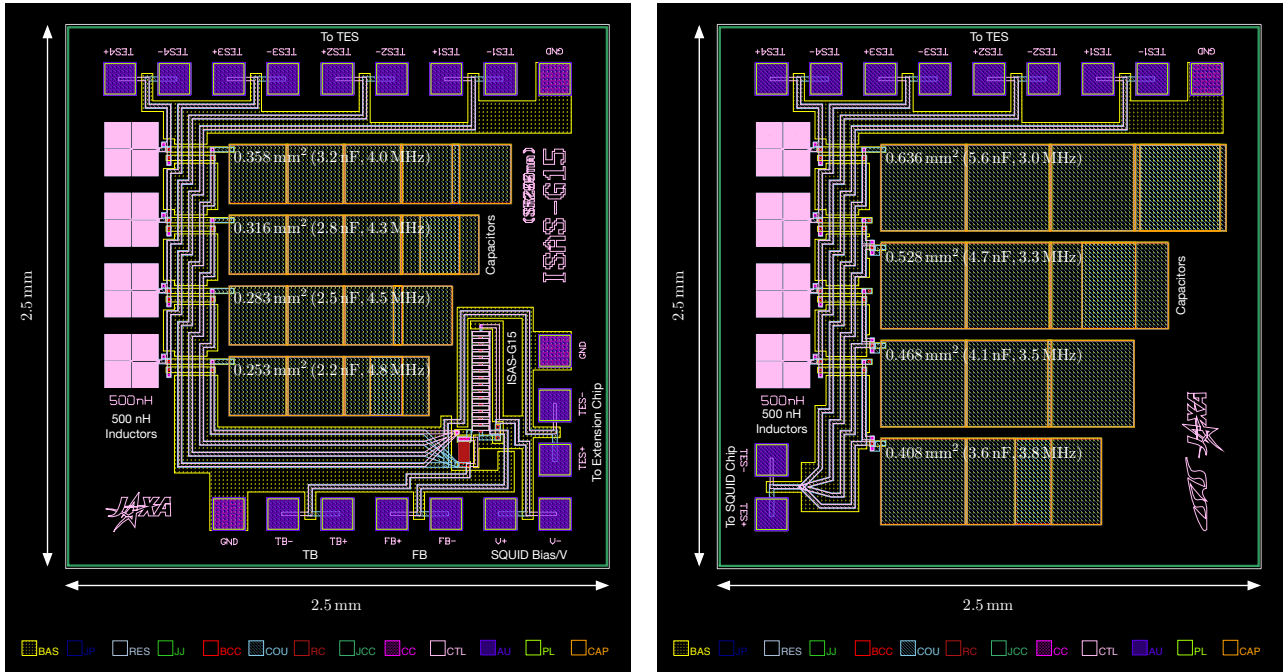


Fig. 3.7 The designs of the 4-input ISAS-G15 chip with built-in LC filters and the 4-input extension chip

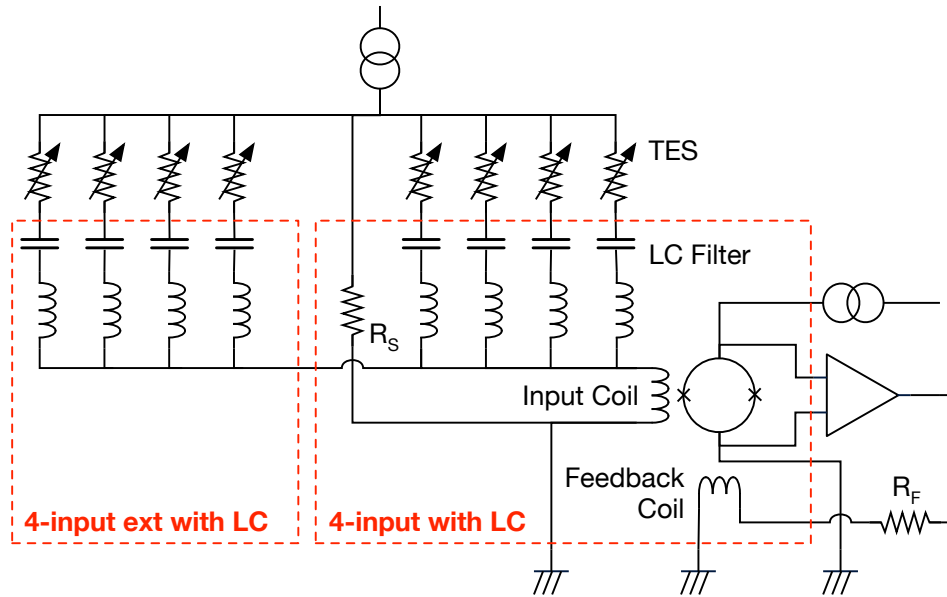


Fig. 3.8 Equivalent circuits for the 4-input SQUID chip with built-in LC filters and the 4-input extension chip

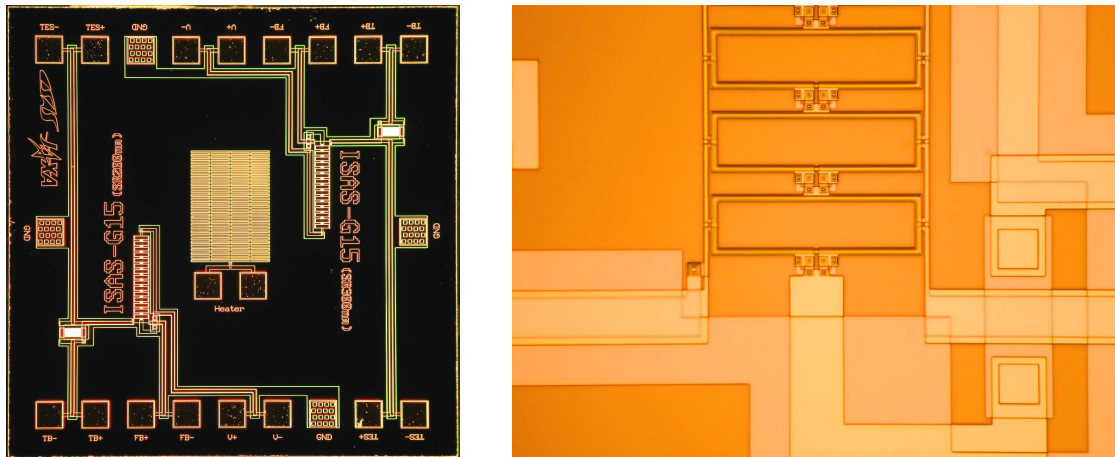


Fig. 3.9 Photomicrographs of the fabricated ISAS-G15: an overall view of the chip (left) and a zoomed SQUID (right)

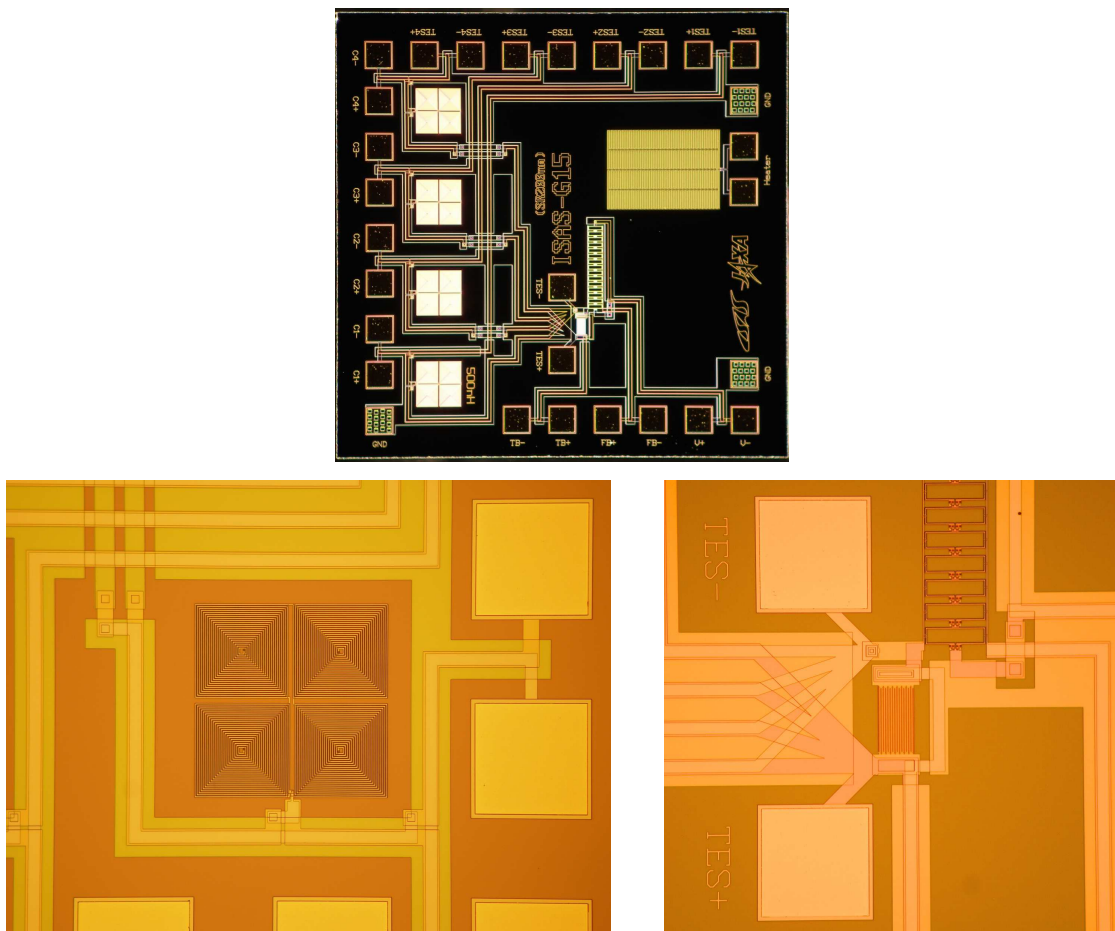


Fig. 3.10 Photomicrographs of the 4-input ISAS-G15 with inductors: an overall view of the chip (top), a zoomed inductor (bottom left), and a zoomed current-summing point (bottom right)

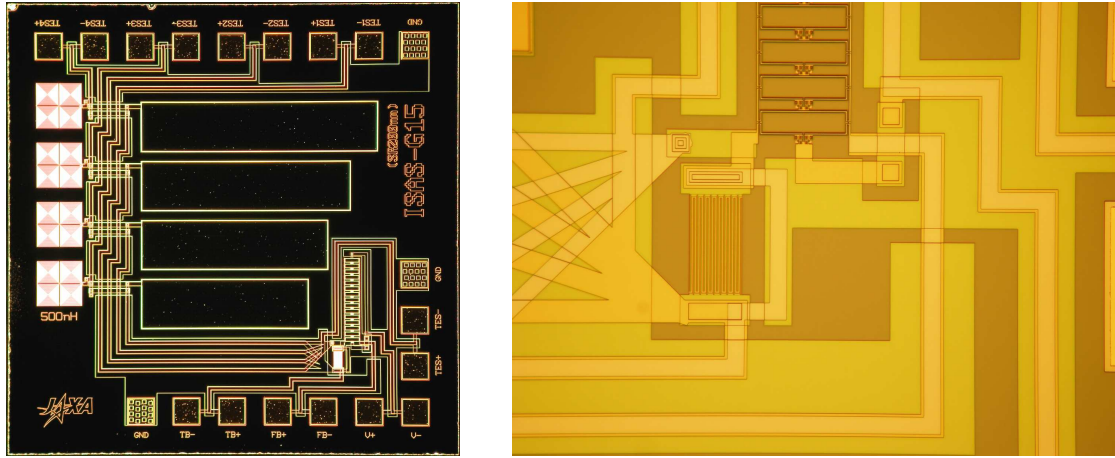


Fig. 3.11 Photomicrographs of the 4-input ISAS-G15 with inductors and capacitors: an overall view of the chip (left) and a zoomed current-summing point (right)

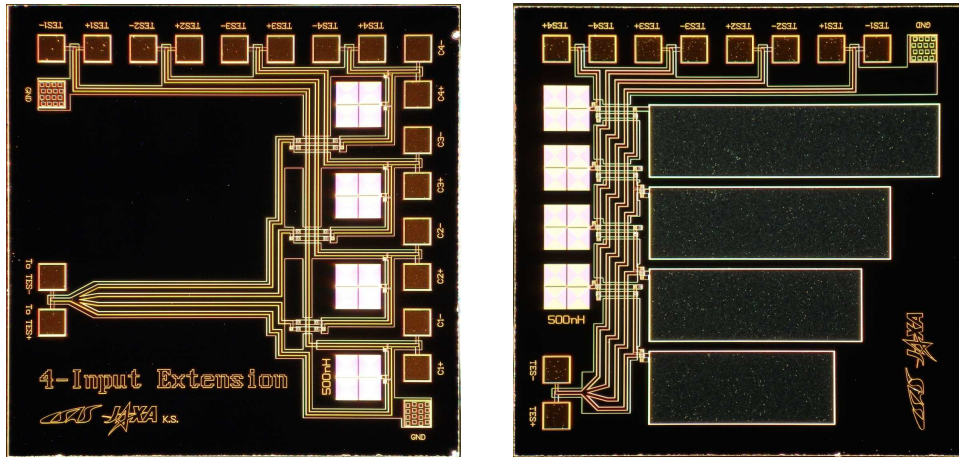


Fig. 3.12 Photomicrographs of the 4-input extension chips: an extension with inductors (left) and an extension with inductors and capacitors (right)

### 3.3.1 Setups

SQUIDS were measured using the Magnicon XXF-1. Figure 3.13 shows the experimental setups for  $\Phi$ - $V$  measurements and noise measurements. For both measurements, SQUIDS were placed at a cryogenic stage (Figure 3.15 left) of a 4 K probe (Figure 3.14) and shielded with a Cryoperm magnetic shield (Figure 3.15 right). The XXF-1 amp is placed in the head of the probe, which is a diecast aluminum box, and carefully shielded for a better noise performance. The SQUID and the amp are wired using paired constantan loom wires. The 4 K probe was then inserted into a LHe dewar upon measurements.

In  $\Phi$ - $V$  measurements, signals were captured using a Yokogawa DL708E DSO equipped with 701855 (12-bit ADC) modules. An IWATSU DS-5324 DSO was also used for a quick look of signals. The XXF-1 was powered by a TEXIO PW18-1.3AT stabilized power supply. In noise measurements, a HP 35670A FFT analyzer was used. In both measurements, all the powers were supplied from a DENKENSEIKI NCT-I noise cut transformer except for the XXF-1 controller PC. It is battery-powered on noise measurements, and optically-isolated from the system on  $\Phi$ - $V$  measurements.

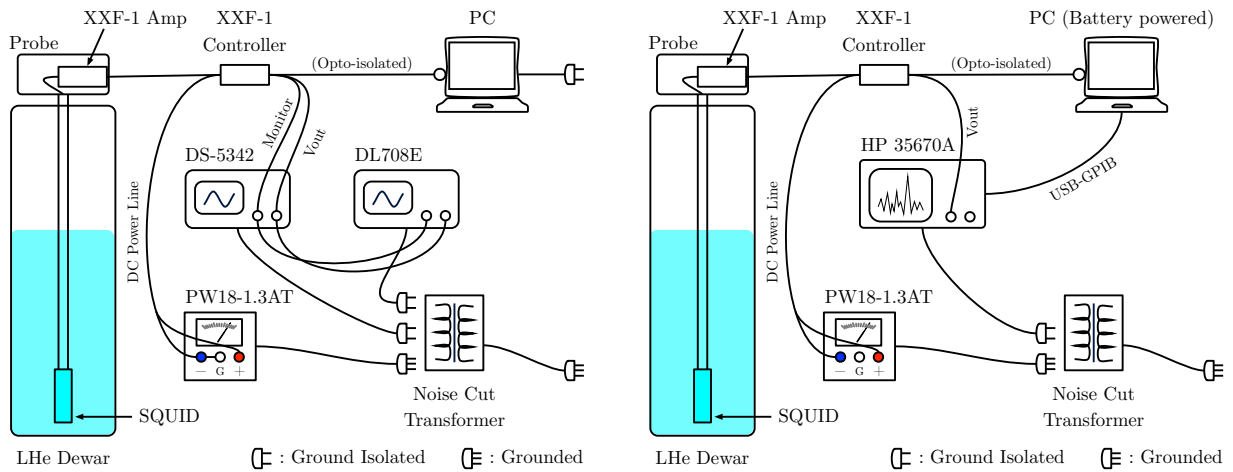


Fig. 3.13 Experimental setups for  $\Phi$ - $V$  measurements (left) and noise measurements (right)

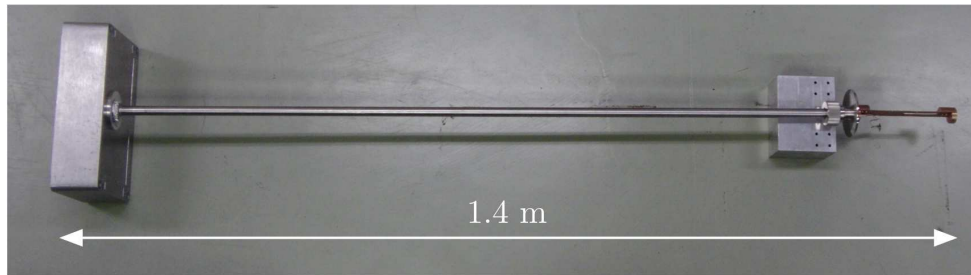


Fig. 3.14 4 K probe

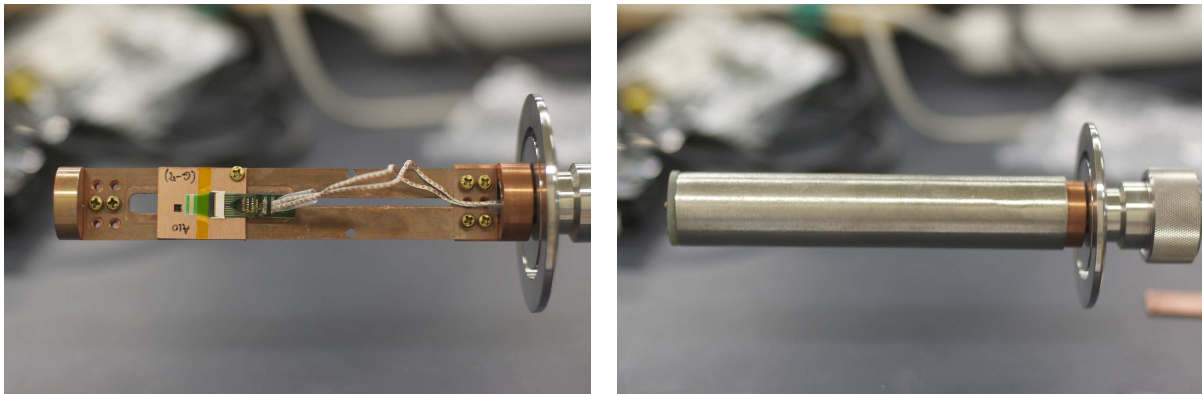


Fig. 3.15 The stage of the 4 K probe: the stage (left) and the stage covered with the Cryoperm magnetic shielding

In filter measurements, the developed analog front-end (Chapter 4) was used as the TES bias current supply and the low noise amp for the SQUID output.

### 3.3.2 $\Phi$ - $V$ Measurements

An 1-Hz  $60\text{-}\mu\text{A}_{\text{p-p}}$  sine wave was applied to the SQUID through the feedback coil (or the input coil when measuring the mutual-inductance of the input coil), and SQUID output was captured 40 times and then averaged. The gain of the XXF-1 amp was set to 2000, and the 5 kHz LPF was applied when capturing at the DL708E. Figure 3.16 shows the obtained  $\Phi$ - $V$  characteristics of ISAS-G15 for bias currents from  $8\text{ }\mu\text{A}$  to  $19\text{ }\mu\text{A}$ . As the

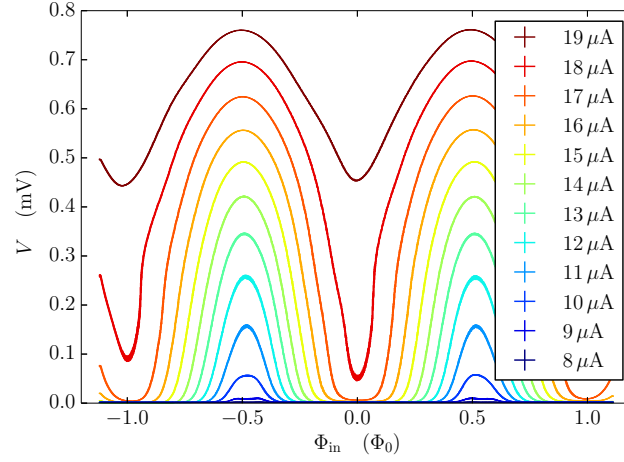


Fig. 3.16 The  $\Phi$ - $V$  characteristics of ISAS-G15 for various values of bias current

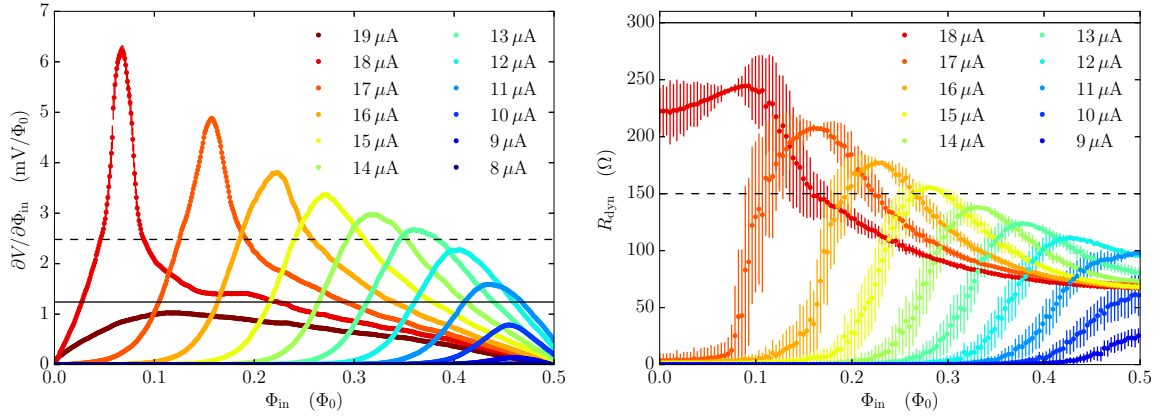


Fig. 3.17  $\partial V/\partial\Phi_{in}$  and the dynamic resistance in  $0-0.5\Phi_0$  of ISAS-G15 for various values of bias current. The dashed lines show the design goals, while the solid lines show the design requirements.

minimum value of the  $\Phi$ - $V$  characteristic becomes larger than 0 when  $I_b > 17\mu\text{A}$ , the critical current of ISAS-G15 is calculated to be  $8.5\mu\text{A}$ , which is slightly larger than the designed value. The power dissipation is then calculated to be slightly-hotter  $22\text{ nW}$ . The mutual-inductances of the input coil and the feedback coil were calculated from periods of the  $\Phi$ - $V$  characteristic to be  $83.26\text{ pH}$  and  $76.62\text{ pH}$  for the input coil and the feedback coil, respectively.

From the  $\Phi$ - $V$  characteristics, the transfer function  $\partial V/\partial\Phi_{in}$  and the dynamic resistance  $\partial V/\partial I_b$  were also derived.  $\partial V/\partial\Phi_{in}$  was obtained by chi-square fitting to  $\Phi$ - $V$  at each point from  $0\Phi_0$  to  $0.5\Phi_0$  for each bias current. Figure 3.17 (left) shows the obtained  $\partial V/\partial\Phi_{in}$ . The dashed line in the plot shows the design goal,  $2.48\text{ mV}/\Phi_0$ , which is equivalent to the required transimpedance gain  $100\text{ V/A}$ , and the solid line shows the design requirement,  $1.24\text{ mV}/\Phi_0$ , which is equivalent to  $50\text{ V/A}$ . The dynamic resistance was obtained by calculating  $\partial V/\partial I_b$  from the obtained  $\Phi$ - $V$  characteristic. Figure 3.17 (right) shows the calculated dynamic resistance. The dashed line in the plot shows the design goal,  $150\Omega$ , and the solid line shows the design requirement,  $300\Omega$ .

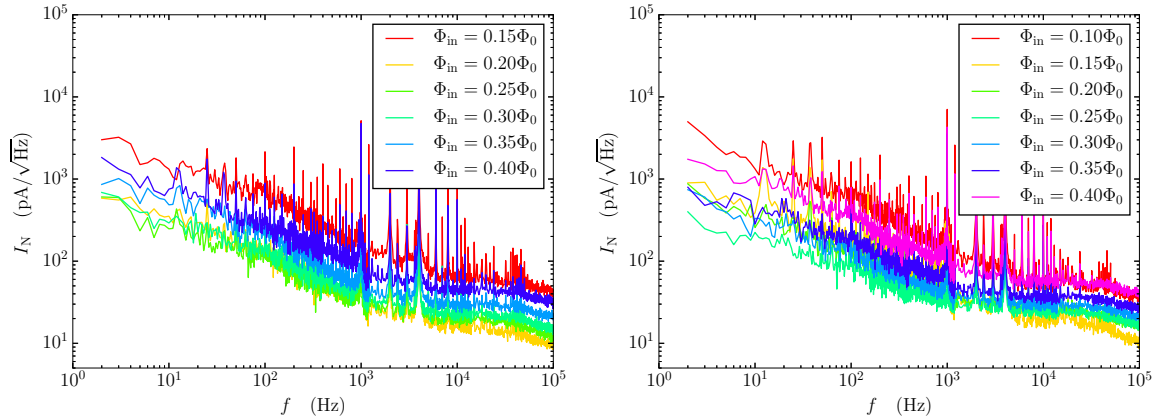


Fig. 3.18 Equivalent input current noises of ISAS-G15 in the open loop for various  $\Phi$  offsets:  $I_b = 16 \mu\text{A}$  (left) and  $I_b = 17 \mu\text{A}$  (right)

Table 3.5 Noise characteristics of ISAS-G15 at 4 K

Bias current	$\Phi$ offset						
	$0.10\Phi_0$	$0.15\Phi_0$	$0.20\Phi_0$	$0.25\Phi_0$	$0.30\Phi_0$	$0.35\Phi_0$	$0.40\Phi_0$
Output voltage noise <sup>†</sup> @ 4 K (nV/ $\sqrt{\text{Hz}}$ )							
$15 \mu\text{A}$	1.0	1.0	1.6	1.5	1.5	1.4	1.3
$16 \mu\text{A}$	1.0	1.6	1.7	1.8	1.4	1.2	1.2
$17 \mu\text{A}$	2.0	2.8	2.0	1.4	1.2	1.1	1.2
Equivalent input current noise <sup>‡</sup> @ 4 K (pA/ $\sqrt{\text{Hz}}$ )							
$15 \mu\text{A}$	...	...	58	13	14	20	32
$16 \mu\text{A}$	...	57	13	17	20	27	41
$17 \mu\text{A}$	49	16	22	21	26	33	51
Equivalent input current noise after other noises subtracted <sup>‡</sup> @ 4 K (pA/ $\sqrt{\text{Hz}}$ )							
$15 \mu\text{A}$	...	...	42	9	10	12	17
$16 \mu\text{A}$	...	42	10	13	13	13	16
$17 \mu\text{A}$	42	15	18	13	13	10	20

<sup>†</sup>Errors are  $< 0.1 \text{ nV}/\sqrt{\text{Hz}}$

<sup>‡</sup>Errors are  $< 1 \text{ pA}/\sqrt{\text{Hz}}$

### 3.3.3 Noise Measurements

The SQUID output voltage noise in open-loop was measured at working points from  $0.1\Phi_0$  to  $0.4\Phi_0$  in  $0.05\Phi_0$  steps for bias currents from  $15 \mu\text{A}$  to  $17 \mu\text{A}$ . The gain of the XXF-1 amp was set to 2000, and the HP 35670A mode was set to FFT analysis with a uniform window in  $\text{V}/\sqrt{\text{Hz}}$  unit. The obtained noise was averaged 10 times in the 1–400 Hz band, 30 times in the 0.4–1.2 kHz band, and 50 times in the 1.2–100 kHz band.

Figure 3.18 shows the noise for bias currents  $16 \mu\text{A}$  and  $17 \mu\text{A}$ . They are converted to the equivalent input current noise  $I_N$  by

$$I_N = \frac{V_N}{Z_{\text{tran}}} = \frac{V}{GZ_{\text{tran}}}, \quad (3.3)$$

where  $V_N$  is the SQUID output voltage noise,  $Z_{\text{tran}}$  is the transimpedance gain calculated from the  $\Phi$ – $V$  characteristics,  $V$  is the system output voltage noise, and  $G$  is the XXF-1 amp gain. However, working points with  $Z_{\text{tran}} > 10 \text{ V/A}$  were only converted. SQUIDs usually have two types of noises,  $1/f$  noise and white noise. Since we use our SQUIDs in the MHz band, we examine white noise only. Table 3.5 shows the white noise level at each

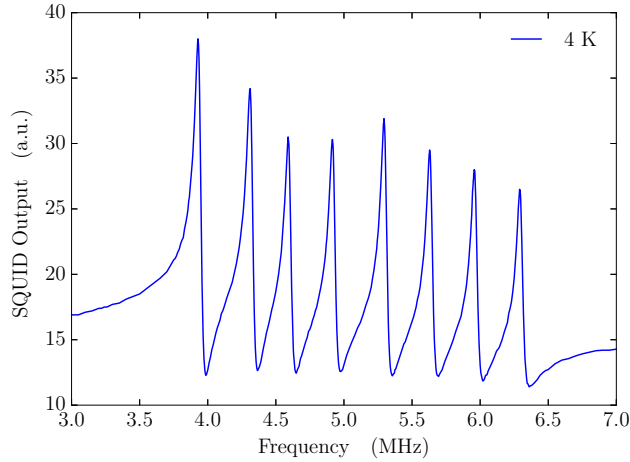


Fig. 3.19 The measured LC bandpass filter characteristic at 4 K

Table 3.6 The measured resonance frequencies of the LC filters on the 4-input current-summing SQUID and the 4-input extension chips

Inductance (nH)	Area (mm <sup>2</sup> )	Capacitance (nF)	Resonance Frequency	
			Design (MHz)	Actual (MHz)
4-input current-summing SQUID				
500	0.358	3.2	4.0	5.294
	0.316	2.8	4.3	5.629
	0.283	2.5	4.5	5.959
	0.253	2.2	4.8	6.291
4-input extension				
500	0.636	5.6	3.0	3.928
	0.528	4.7	3.3	4.309
	0.468	4.1	3.5	4.592
	0.408	3.6	3.8	4.914

working point obtained by fitting the noise spectra for  $f > 10$  kHz, along with the calculated equivalent input current noise.

The noise values in Table 3.5 includes noises arisen from components other than SQUID. To eliminate those noises and estimate unblended SQUID noises, we first measured the system noise without having any SQUID at the cryogenic stage but shorted, and subtracted it from the measured noises. The system noise without SQUID is  $2.2 \mu\text{V}/\sqrt{\text{Hz}}$ . Table 3.5 also shows the subtracted noises.

### 3.3.4 Filter Measurements

The 4-input SQUID with built-in filters and the 4-input extension with built-in filters are connected by bonding wires, and eight  $50 \text{ m}\Omega$  resistors are connected to those chips as a dummy TES. A sinusoidal signal was then applied to the TES bias line. Since the SQUID was used in the open-loop, the amplitude of the signal is kept low so that the SQUID output at the resonance frequencies is not folded. The frequency of the signal was then swept from 3 to 7 MHz in 1 kHz steps. Figure 3.19 shows the measured filter characteristic at 4 K. The designed resonance frequencies are from 3 to 5 MHz, but the measured resonance frequencies are from about 4 to 6.5 MHz, meaning that the actual relative permittivity is somewhat smaller than the expected value. Table 3.6 shows the measured resonance frequencies along with the designed values. The calculated actual relative permittivity is

Table 3.7 ISAS-G15 working point

$I_b$ ( $\mu\text{A}$ )	$\Phi$ offset ( $\Phi_0$ )	$\partial V/\partial\Phi_{\text{in}}$ ( $\text{mV}/\Phi_0$ )	$Z_{\text{tran}}$ ( $\text{V}/\text{A}$ or $\Omega$ )	$R_{\text{dyn}}$ ( $\Omega$ )	$I_N$ ( $\text{pA}/\sqrt{\text{Hz}}$ )
15	0.30	$2.9 \pm 0.1$	$117 \pm 1$	$152 \pm 4$	$9.7 \pm 0.2$

Table 3.8 Design targets and measurement results of ISAS-G15

SQUID Parameter	Measurement	Result	Goal	Requirement
Critical current ( $\mu\text{A}$ )	$I_0$	8.5	–	–
Input coil mutual-inductance (pH)	$M_{\text{in}}$	83.26	–	–
Feedback coil mutual-inductance (pH)	$M_{\text{FB}}$	76.62	–	–
SQUID Figures of Merit				
Thermal power dissipation (nW)	$P$	22	$< 20$	$< 32$
Equivalent input current noise @ 4K ( $\text{pA}/\sqrt{\text{Hz}}$ )	$I_N$	10	$< 10$	$< 20$
Transimpedance gain ( $\text{V}/\text{A}$ or $\Omega$ )	$Z_{\text{tran}}$	117	$> 100$	$> 50$
Output impedance ( $\Omega$ )	$Z_{\text{out}}$	150	$< 150$	$< 300$

$\sim 6$ .

### 3.3.5 Working Points

From the  $\Phi$ - $V$  characteristic and the noise characteristics, the SQUID working points that fulfill the requirement were selected. There is only one working point found that fulfills all the requirements. Table 3.7 shows the working point and figures of merit at the point.

### 3.3.6 Measurement Summary

Table 3.8 summarizes the measurement results of ISAS-G15 along with the design targets.

## 3.4 Summary

In this chapter we have successfully developed the low-power SQUID with the sufficient gain and the low noise. The heat dissipation is as low as  $\sim 20$  nW while the transimpedance gain is  $> 100$  V/A and the equivalent input current noise is  $\sim 10$  pA/ $\sqrt{\text{Hz}}$  @ 4K. With these attributes, the simple single-staged cryogenic setup for the DIOS mission and even for the ATHENA mission is amply feasible. We also developed the 4-input SQUID chip with built-in bandpass filters using the developed low-power SQUID, and the 4-input extension chip with built-in bandpass filters. The former consists of the low-power SQUID, the TES shunt resistor, and the LC bandpass filters for four channels in the size of  $2.5 \times 2.5$  mm. The latter is in the same size and can be connected to the former chip with bonding wires to add four more multiplexing channels. These chips dramatically simplify the cryogenic stage and greatly support the realization of large-format TES readout cryoelectronics.



## Chapter 4

# Development of Digital Electronics for Frequency-Division Multiplexing

### 4.1 Principles of Frequency-Division Multiplexing and Baseband Feedback

#### 4.1.1 Preparation

We use the following definition for the Fourier transform:

$$\hat{f}(\omega) = \int_{-\infty}^{\infty} f(t)e^{-i\omega t} dt = \mathcal{F}[f(t)]. \quad (4.1)$$

The Fourier transform of  $f(t) \cos(at)$  is then given by

$$\mathcal{F}[f(t) \cos(at)] = \frac{1}{2} \mathcal{F}[f(t)(e^{iat} + e^{-iat})] = \frac{1}{2} \hat{f}(\omega - a) + \frac{1}{2} \hat{f}(\omega + a). \quad (4.2)$$

We also define the resistance of a microcalorimeter at time  $t$  as

$$R(t) = R_0 + \Delta R(t), \quad (4.3)$$

where  $R_0$  is the resistance at the operating temperature, and  $\Delta R(t)$  is the deviation of the resistance due to an incident X-ray photon at time  $t$ .

#### 4.1.2 Principles of AC-biased Microcalorimeter

Figure 4.1 (left) shows the typical TES biasing with a constant DC current, and the bias current  $I_{\text{in}}(t)$  in this case is given by

$$I_{\text{in}}(t) = I_0. \quad (4.4)$$

The TES is considered to be biased by a constant voltage  $V_0 (\approx I_0 R_s)$  as long as  $R_s \ll R_{\text{TES}}$  is maintained. The Joule heating of the TES,  $P_b(t)$ , then becomes

$$P_b(t) = \frac{V_0^2}{R_0} = P_0. \quad (4.5)$$

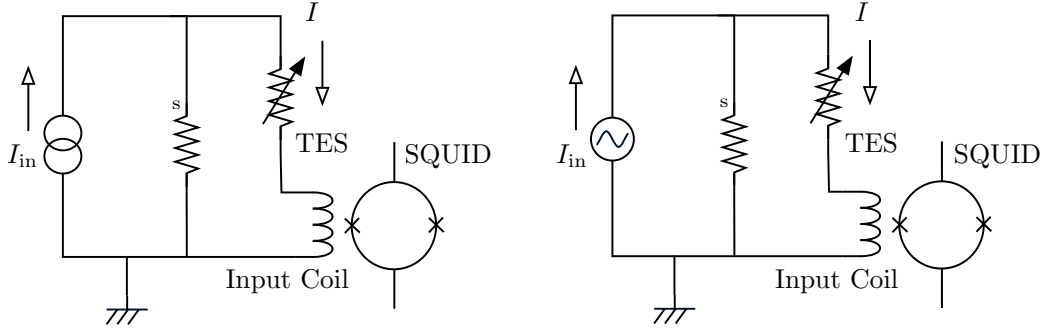


Fig. 4.1 TES biasing with DC-current (left) and AC-current (right)

The input current to the SQUID,  $I_{\text{sq}}(T)$ , is then given by

$$I_{\text{sq}}(t) = \frac{V_0}{R(t)}. \quad (4.6)$$

Fourier transforming this equation gives

$$\hat{I}_{\text{sq}}(\omega) = V_0 \mathcal{F} \left[ \frac{1}{R(\omega)} \right], \quad (4.7)$$

and from (4.3) we obtain

$$\frac{1}{R(t)} = \frac{1}{R_0 + \Delta R(t)} \quad (4.8)$$

$$\approx \frac{1}{R_0} \left( 1 - \frac{\Delta R(t)}{R_0} \right). \quad (4.9)$$

The Fourier transformation of above is

$$\mathcal{F} \left[ \frac{1}{R(\omega)} \right] \approx \mathcal{F} \left[ \frac{1}{R_0} \left( 1 - \frac{\Delta R(t)}{R_0} \right) \right] = \frac{1}{R_0} \delta(\omega) - \frac{\Delta \hat{R}(\omega)}{R_0^2}, \quad (4.10)$$

where  $\delta(\omega)$  is the Dirac delta function. (4.6) thus becomes

$$\hat{I}_{\text{sq}}(\omega) = \frac{V_0}{R_0} \delta(\omega) - \frac{V_0}{R_0^2} \Delta \hat{R}(\omega). \quad (4.11)$$

$\Delta \hat{R}(\omega)$  is generally confined to a frequency range,  $-\omega_s < \omega < \omega_s$ . Therefore, the power spectrum of the TES signal is confined around  $\omega = 0$  as in Figure 4.2.

We now consider the TES biasing with a sinusoidal AC current (Figure 4.1 right). Suppose that the bias current in this case is given by

$$I_{\text{in}}(t) = \sqrt{2} I_0 \cos(\omega_0 t + \theta), \quad (4.12)$$

where  $\omega_0$  is the carrier frequency. The Joule heating of the TES then becomes

$$P_b(t) = \frac{2V_0^2}{R_0} \cos^2(\omega_0 t + \theta). \quad (4.13)$$

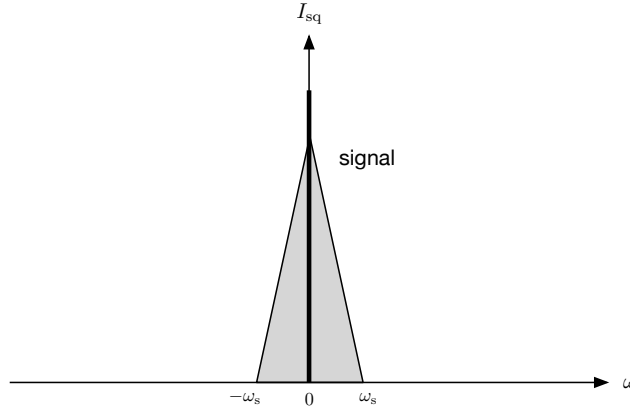


Fig. 4.2 The signal power spectrum of DC-biased TES

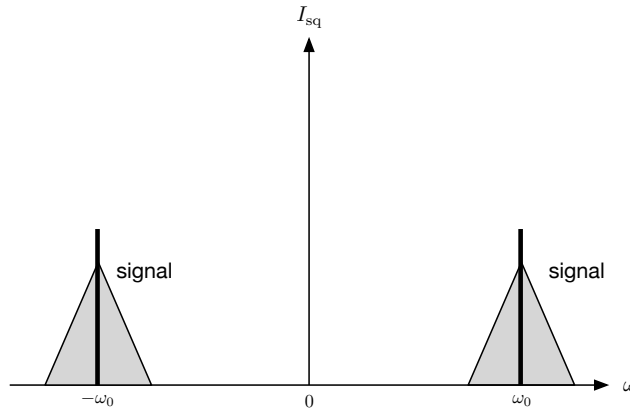


Fig. 4.3 The signal power spectrum of AC-biased TES

The time-averaged Joule heating is thus given by

$$\bar{P}_b(t) = \frac{V_0^2}{R_0} = P_0, \quad (4.14)$$

which is identical to the Joule heating (4.5) in the DC-biased base. The SQUID input in this case is given by

$$I_{\text{sq}}(t) = \frac{\sqrt{2}V_0 \cos(\omega_0 t + \theta)}{R(t)}, \quad (4.15)$$

and its Fourier transformation is then given by

$$\hat{I}_{\text{sq}}(\omega) = \sqrt{2} \left[ \frac{e^{i\theta}}{2} \left\{ \frac{V_0}{R_0} \delta(\omega - \omega_0) - \frac{V_0}{R_0^2} \Delta \hat{R}(\omega - \omega_0) \right\} + \frac{e^{-i\theta}}{2} \left\{ \frac{V_0}{R_0} \delta(\omega + \omega_0) - \frac{V_0}{R_0^2} \Delta \hat{R}(\omega + \omega_0) \right\} \right]. \quad (4.16)$$

Therefore, the power spectrum of the TES signal is split into two components where  $\omega = \pm\omega_0$  as in Figure 4.3.

To retrieve the TES signal from the modulated signal (4.16), it needs to be demodulated. There are several methods for the demodulation. One way is a phase detection. By multiplying (4.15) with  $\sqrt{2} \cos(\omega_0 t + \theta')$ , we obtain

$$I'_{\text{sq}}(t) = \sqrt{2} I_{\text{sq}}(t) \cos(\omega_0 t + \theta') = \frac{2V_0}{R(t)} \cos(\omega_0 t + \theta) \cos(\omega_0 t + \theta'), \quad (4.17)$$

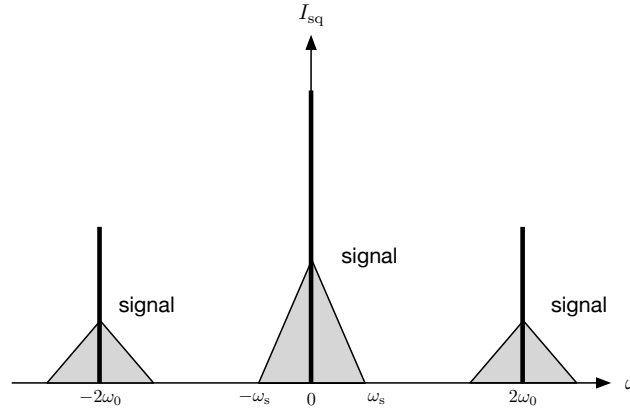


Fig. 4.4 The demodulated signal power spectrum using the phase detection method

and its Fourier transformation is given by

$$\begin{aligned} \hat{I}'_{sq}(\omega) &= \cos(\theta - \theta') \left\{ \frac{V_0}{R_0} \delta(\omega) - \frac{V_0}{R_0^2} \Delta \hat{R}(\omega) \right\} \\ &+ \frac{e^{i(\theta + \theta')}}{2} \left\{ \frac{V_0}{R_0} \delta(\omega - 2\omega_0) - \frac{V_0}{R_0^2} \Delta \hat{R}(\omega - 2\omega_0) \right\} \\ &+ \frac{e^{-i(\theta + \theta')}}{2} \left\{ \frac{V_0}{R_0} \delta(\omega + 2\omega_0) - \frac{V_0}{R_0^2} \Delta \hat{R}(\omega + 2\omega_0) \right\}. \end{aligned} \quad (4.18)$$

When  $\theta = \theta'$ , the power spectrum of the demodulated signal becomes as in Figure 4.4. We can retrieve the first term on the right-hand side by applying a low-pass filter and obtain

$$\hat{I}''_{sq}(\omega) = \frac{V_0}{R_0} \delta(\omega) - \frac{V_0}{R_0^2} \Delta \hat{R}(\omega), \quad (4.19)$$

which is exactly the same as (4.11).

Another method is an I/Q demodulation. In this method, we multiply (4.15) with  $\sqrt{2} \sin(\omega_0 t + \theta')$  and  $\sqrt{2} \cos(\omega_0 t + \theta')$ , and obtain

$$I(t) = \frac{2V_0}{R(t)} \cos(\omega_0 t + \theta) \sin(\omega_0 t + \theta'), \quad (4.20)$$

$$Q(t) = \frac{2V_0}{R(t)} \cos(\omega_0 t + \theta) \cos(\omega_0 t + \theta'), \quad (4.21)$$

where  $I(t)$  and  $Q(t)$  are called in-phase and quadrature components, respectively. Their Fourier transformations are given by

$$\begin{aligned} \hat{I}(\omega) &= \sin(\theta - \theta') \left\{ \frac{V_0}{R_0} \delta(\omega) - \frac{V_0}{R_0^2} \Delta \hat{R}(\omega) \right\} \\ &+ \frac{e^{i(\theta - \theta')}}{2i} \left\{ \frac{V_0}{R_0} \delta(\omega - 2\omega_0) - \frac{V_0}{R_0^2} \Delta \hat{R}(\omega - 2\omega_0) \right\} \\ &+ \frac{e^{-i(\theta - \theta')}}{2i} \left\{ \frac{V_0}{R_0} \delta(\omega + 2\omega_0) - \frac{V_0}{R_0^2} \Delta \hat{R}(\omega + 2\omega_0) \right\} \end{aligned} \quad (4.22)$$

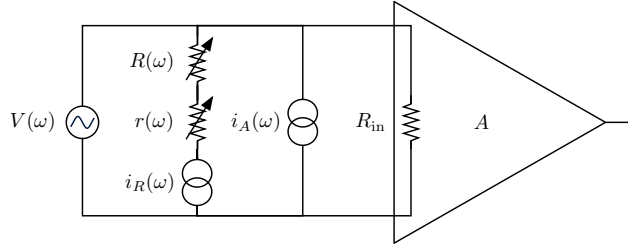


Fig. 4.5 Equivalent noise circuit for AC-biased microcalorimeter

for  $I(t)$  and

$$\begin{aligned} \hat{Q}(\omega) = & \cos(\theta - \theta') \left\{ \frac{V_0}{R_0} \delta(\omega) - \frac{V_0}{R_0^2} \Delta \hat{R}(\omega) \right\} \\ & + \frac{e^{i(\theta + \theta')}}{2} \left\{ \frac{V_0}{R_0} \delta(\omega - 2\omega_0) - \frac{V_0}{R_0^2} \Delta \hat{R}(\omega - 2\omega_0) \right\} \\ & + \frac{e^{-i(\theta + \theta')}}{2} \left\{ \frac{V_0}{R_0} \delta(\omega + 2\omega_0) - \frac{V_0}{R_0^2} \Delta \hat{R}(\omega + 2\omega_0) \right\} \end{aligned} \quad (4.23)$$

for  $Q(t)$ . Again we retrieve the first term by applying a low-pass filter and obtain

$$\begin{aligned} \hat{I}'(\omega) = & \sin(\theta - \theta') \left\{ \frac{V_0}{R_0} \delta(\omega) - \frac{V_0}{R_0^2} \Delta \hat{R}(\omega) \right\}, \\ \hat{Q}'(\omega) = & \cos(\theta - \theta') \left\{ \frac{V_0}{R_0} \delta(\omega) - \frac{V_0}{R_0^2} \Delta \hat{R}(\omega) \right\}, \end{aligned}$$

and by taking an absolute value of these vectors we finally obtain the demodulated signal as the same as (4.11). This method is superior to the phase detection method in a way that it is independent to  $\theta'$ .

### 4.1.3 Noise of AC-biased microcalorimeters

Figure 4.5 shows the equivalent noise circuit for an AC-biased microcalorimeter.  $R$ ,  $V$ ,  $R_{\text{in}}$ , and  $A$  are the TES resistance, the bias voltage, the input impedance of ammeter, and the gain of readout system, respectively.  $r$ ,  $i_R$ , and  $i_A$  are noise sources.  $r$  represents the noise that appears in the TES resistance, such as the phonon noise, and satisfies  $R_0 \gg |\Delta R(t)| \gg |r(t)|$ .  $i_R$  and  $i_A$  represent the current noise due to Johnson noise and the equivalent input voltage noise of the readout system, respectively.

Let us first consider the DC-biasing case using Figure 4.5. When  $V(t) = V_0$ , the TES output current (or SQUID input current) is given by

$$I_{\text{sq}}(t) = \frac{V_0}{R(t) + r(t)} + i_R(t) + i_A(t) \quad (4.24)$$

$$\approx \frac{V_0}{R_0} \left( 1 - \frac{\Delta R(t) + r(t)}{R_0} \right) + i_R(t) + i_A(t). \quad (4.25)$$

From (4.10), the Fourier transformation of above becomes

$$\hat{I}_{\text{sq}}(\omega) \approx \frac{V_0}{R_0} \delta(\omega) - \frac{V_0}{R_0^2} \Delta \hat{R}(\omega) - \frac{V_0}{R_0^2} \hat{r}(\omega) + \hat{i}_R(\omega) + \hat{i}_A(\omega). \quad (4.26)$$

The first two terms at the right-hand side represent the signal on a X-ray event, and its power spectral density

is given by

$$\hat{i}_S^2(\omega) = \frac{V_0^2}{R_0^4} \Delta \hat{R}^2(\omega). \quad (4.27)$$

The rest represents the noise, and its power spectral density is given by

$$\hat{i}_N^2(\omega) = \hat{i}_{N1}^2(\omega) + \hat{i}_{N2}^2(\omega), \quad (4.28)$$

where

$$\hat{i}_{N1}^2(\omega) = \frac{V_0^2}{R_0^4} \hat{r}^2(\omega), \quad (4.29)$$

which represents the noise due to the TES resistance, and

$$\hat{i}_{N2}^2(\omega) = \hat{i}_R^2(\omega) + \hat{i}_A^2(\omega), \quad (4.30)$$

which represents the noise due to Johnson noise and the readout system noise. Therefore, the signal-to-noise ratio (SNR) for the DC-biasing case is

$$(SNR_1)^2 = \frac{\Delta \hat{R}^2(\omega)}{\hat{r}^2(\omega)}, \quad (4.31)$$

$$(SNR_2)^2 = \frac{V_0^2}{R_0^4} \frac{\Delta \hat{R}^2(\omega)}{\hat{i}_R^2(\omega) + \hat{i}_A^2(\omega)}, \quad (4.32)$$

where  $SNR_1 \equiv i_S/i_{N1}$  and  $SNR_2 \equiv i_S/i_{N2}$ .

We now consider the AC-biasing case. Suppose that we have

$$V(t) = \sqrt{2}V_0 \cos(\omega_0 t). \quad (4.33)$$

The TES output (or SQUID input) is then given by

$$I_{\text{sq}}(t) = \frac{\sqrt{2}V_0 \cos(\omega_0 t)}{R(t) + r(t)} + i_R(t) + i_A(t) \quad (4.34)$$

$$\approx \frac{\sqrt{2}V_0 \cos(\omega_0 t)}{R_0} \left( 1 - \frac{\Delta R(t) + r(t)}{R_0} \right) + i_R(t) + i_A(t), \quad (4.35)$$

and its Fourier transformation is given by

$$\begin{aligned} \hat{I}_{\text{sq}}(\omega) = \sqrt{2} \left[ \frac{1}{2} \left\{ \frac{V_0}{R_0} \delta(\omega - \omega_0) - \frac{V_0}{R_0^2} \Delta \hat{R}(\omega - \omega_0) \right\} + \frac{1}{2} \left\{ \frac{V_0}{R_0} \delta(\omega + \omega_0) - \frac{V_0}{R_0^2} \Delta \hat{R}(\omega + \omega_0) \right\} \right] \\ - \sqrt{2} \left[ \frac{1}{2} \frac{V_0}{R_0^2} \hat{r}(\omega - \omega_0) + \frac{1}{2} \frac{V_0}{R_0^2} \hat{r}(\omega + \omega_0) \right] + \hat{i}_R(\omega) + \hat{i}_A(\omega). \end{aligned} \quad (4.36)$$

Let us demodulate (4.35) and apply a low-pass filter, then we obtain

$$\begin{aligned} \hat{I}'_{\text{sq}}(\omega) = \left( \frac{V_0}{R_0} \delta(\omega) - \frac{V_0}{R_0^2} \Delta \hat{R}(\omega) - \frac{V_0}{R_0^2} \Delta \hat{r}(\omega) \right) \\ + \frac{\sqrt{2}}{2} \left\{ \hat{i}_R(\omega - \omega_0) + \hat{i}_R(\omega + \omega_0) + \hat{i}_A(\omega - \omega_0) + \hat{i}_A(\omega + \omega_0) \right\}. \end{aligned} \quad (4.37)$$

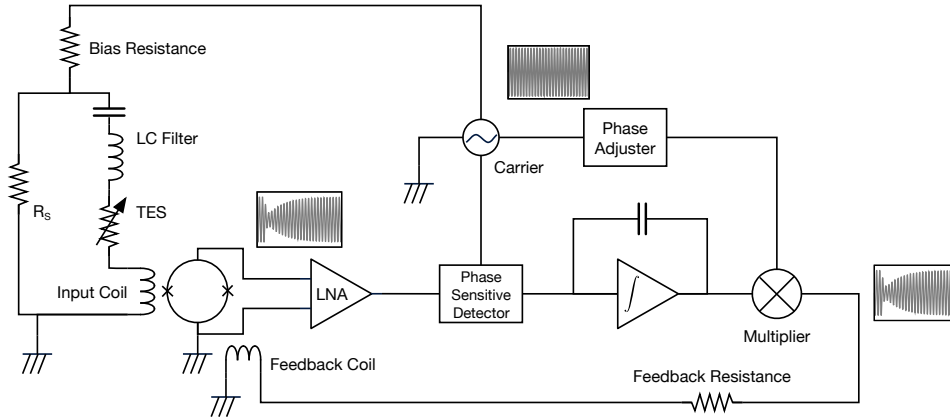


Fig. 4.6 The schematic diagram of the baseband feedback architecture. Only the single channel configuration is shown.

Therefore, the power spectral density of noise becomes

$$\hat{i}_{N1}^2(\omega) = \frac{V_0^2}{R_0^4} \hat{r}^2(\omega), \quad (4.38)$$

which remains the same, and

$$\hat{i}_{N2}^2(\omega) = \frac{1}{2} \left\{ \hat{i}_R^2(\omega - \omega_0) + \hat{i}_R^2(\omega + \omega_0) + \hat{i}_A^2(\omega - \omega_0) + \hat{i}_A^2(\omega + \omega_0) \right\}. \quad (4.39)$$

When  $\hat{i}_R^2(\omega - \omega_0) = \hat{i}_R^2(\omega + \omega_0)$  and  $\hat{i}_A^2(\omega - \omega_0) = \hat{i}_A^2(\omega + \omega_0)$  within the signal band  $-\omega_s < \omega < \omega_s$ , the above equation can be given as

$$\hat{i}_{N2}^2(\omega) = \hat{i}_R^2(\omega_0) + \hat{i}_A^2(\omega_0), \quad (4.40)$$

and the SNR becomes identical to (4.31) and (4.32). This means that the difference of SNR between the DC-biasing case and the AC-biasing case is determined only by (4.30) and (4.40). The readout noise at low frequency is generally larger on account of  $1/f$  noise, and the SNR in AC-biasing is thus larger than that in DC-biasing.

#### 4.1.4 Principles of Baseband Feedback

In FDM TES are typically biased at several MHz, which is sufficiently faster than the thermal time constant of TES, and is sufficiently large to multiplex enough number of TES channels. However, it is too fast to stably feedback in the flux-locked loop mostly because of the parasitic capacitance of electrical wires between the cryogenic stage and the room temperature electronics. The typical parasitic capacitance of a twisted-pair of wires used in a refrigerator is  $\sim 100$  pF/m, and the typical length of the wires is  $\sim 1$  m or more. As a result, the parasitic capacitance can be several hundreds of pF, which is critically high for the FLL in MHz. To achieve a stable feedback even in MHz frequency, a feedback scheme called baseband feedback (BBFB) is used.

Figure 4.6 shows the schematic diagram of BBFB. The modulated signal is first demodulated at the phase sensitive detector (or the I/Q demodulator) and the baseband signal is extracted. The integrator is then applied to the baseband signal, as is done in the DC-biasing FLL. Finally, another carrier signal that is phase-adjusted, so that the phase becomes opposite at the summing point, is modulated by the baseband signal, and then sent back to the SQUID to nullify the input. In this way, we succeeded in the stable FLL for a 5 MHz carrier [31]. Although BBFB overcomes the wire delay, the closed loop of FLL should still be as short as possible to eliminate

Table 4.1 Requirements for digital electronics

	Minimal (8 multiplexing)	Goal (16 multiplexing)
Bandwidth	> 1.5 MHz	> 3 MHz
ADC SNR (and theoretical bit width)	60 dB (10 bits)	60 dB (10 bits)
DAC SNR (and theoretical bit width)	78 dB (13 bits)	84 dB (14 bits)
ADC and DAC Sampling Rate	$\gg$ 6 MHz	$\gg$ 12 MHz
FPGA Multiplier	> 200	> 400
FPGA RAM	> 4 MB	> 8 MB

the baseband signal delay, which makes a finite input into SQUID even in the FLL and ultimately causes a flux jump.

In our previous study, we succeeded to multiplex two TES signals, one biased with a 1.0 MHz carrier and the other biased with a 1.5 MHz carrier, and to readout X-ray pulses simultaneously [35]. We used the analog-based room-temperature electronics for BBFB, which jointly-developed with NF corporation, but it supports only up to 2 MHz carrier frequency, thus it is not suitable for high-density multiplexing. Moreover, the lack of scalability in analog-based circuits may become the major drawback when realizing a readout system for large-format TES arrays. As we have successfully demonstrated the principle of BBFB using the analog electronics, we started to develop a scalable FPGA-based digital readout system.

## 4.2 Requirements for Digital Electronics

To multiplex 256 to 400 signals with a reasonable number of SQUIDs, a single SQUID should multiplex at least 8 signals, and preferably 16 signals or more. A typical bandwidth of a baseband signal (TES signal) is  $\sim 100$  kHz, hence a required spacing frequency between multiplexed channels is  $\gtrsim 200$  kHz, which makes the number of multiplexed channels within 1 MHz bandwidth to be 5 or less. To multiplex at least 8 signals with a single SQUID, we need a bandwidth of more than 1.5 MHz.

The TES for DIOS will be optimized for soft X-rays ( $\lesssim 2$  keV) and the requirement on energy resolution is 2 eV, so the required SNR for the system is at least 60 dB. In FDM with BBFB, the SQUID output will be suppressed by a factor of the loopgain, which is the function of baseband frequency. The lower frequency ( $\sim$ DC) of the signal gets almost fully suppressed, but the higher frequency may not get suppressed. However, it would cause an excess only when photons hit TES at the very same time, which should rarely occur for astronomical observations where the typical count rate is less than 1 cps. Therefore, an increase of multiplexing channels would not cause an excess in ADC dynamic ranges. On the other hand, as the multiplexing number increases, a dynamic range of DAC for a single channel decreases, so the required SNR for DAC would be higher than that of ADC, and can be expressed as  $60 + 6.02 \times \log_2$  (number of multiplexing channels) dB. To multiplex 8 signals, the required SNR for DAC would be 78 dB, while it would be 84 dB to multiplex 16 signals. Therefore, a 13-bit DAC is sufficient to multiplex 8 signals, while a 14-bit DAC is sufficient to multiplex 16 signals theoretically. In a real world scenario we need more DAC bits due to noises. Obviously both ADC and DAC need to have sufficient sampling rates to satisfy the required system bandwidth. To multiplex 8 signals, the required bandwidth is  $> 1.5$  MHz, and if a band from 1.5 to 3.0 MHz is used, then we need a sampling rate of more than 6 MHz. To multiplex 16 signals, we need a doubled sampling rate.

Recent fast field-programmable gate arrays (FPGAs) have plenty of logic cells, block RAMs, and multipliers, so we may not need to worry about resources when selecting a FPGA. It should have at least several hundreds of multipliers (at least 16-bit $\times$ 16-bit) for signal processing, and several megabytes of RAM for data acquisition.

We summarized the requirements for digital electronics in Table 4.1.

Table 4.2 FMC150 specifications

ADC (ADS62P49)	
Number of channels	2
Channel resolution	14-bit
Input voltage range	$2 V_{pp}$ (10 dBm)
Input gain	Programmable from 0 dB to 6 dB in 0.5 dB steps
Input impedance	$50 \Omega$ (AC-coupled)
Analog input bandwidth	0.40 – 500 MHz
SNR	71 dBFS @ 45 MHz
SFDR	80 dBc @ 45 MHz
DAC (DAC3283)	
Number of channels	2
Channel resolution	16-bit
Output voltage range	$1 V_{pp}$
Output impedance	$50 \Omega$ (AC-coupled)
Analog output bandwidth	82 MHz 5th-order Chebyshev LPF 3 MHz HPF due to the output transformer
THD	-67 dBc

## 4.3 System Overview

For rapid prototyping, this time we selected off-the-shelf FPGA and ADC/DAC boards.

### 4.3.1 ADC/DAC Board

We selected the 4DSP FMC150 ADC/DAC board. It has two 250Mps 14-bit ADC and two 800Mps 16-bit DAC, and can be mounted to FPGA boards with a low-pin count (LPC) FPGA mezzanine card (FMC) connector. It is based on Texas Instruments (TI) ADS62P49 and TI DAC3283. The detailed specifications are summarized in Table 4.2. The input bandwidth is broad enough to use for the BBFB, while the output bandwidth has a low-cut off at 3 MHz, which may causes a loss of loopgain in smaller frequency. The loopgain, however, can be adjusted in each channel, and the effect of the low-cut off thus may be negligible.

The input voltage range of the ADC is  $2 V_{pp}$ , while its of the DAC is  $1 V_{pp}$ . To adjust the input/output range, we configured the ADC input gain to be 6 dB. This makes the actual input bit width to be 13 bits.

The DAC has internal  $\times 2$  and  $\times 4$  interpolators, however, we do not use any of them as they introduce additional delays in signals (discussed in Section 4.5).

### 4.3.2 FPGA Board

We selected the Xilinx ML605 evaluation board<sup>\*1</sup>. It is based on Xilinx Virtex-6 LX240T (XC6VLX240T-1FFG1156) FPGA, which provides 240k logic cells, 768 25-bit $\times$ 18-bit multipliers, and 15 MB block RAM. The board has one LPC FMC connector and one high-pin count (HPC) FMC connector, so it can mount up to two FMC150 boards, which makes possible to multiplex 32 signals thanks to the plenty of FPGA resources.

<sup>\*1</sup> The system is also ported to the Xilinx KC705 evaluation board.

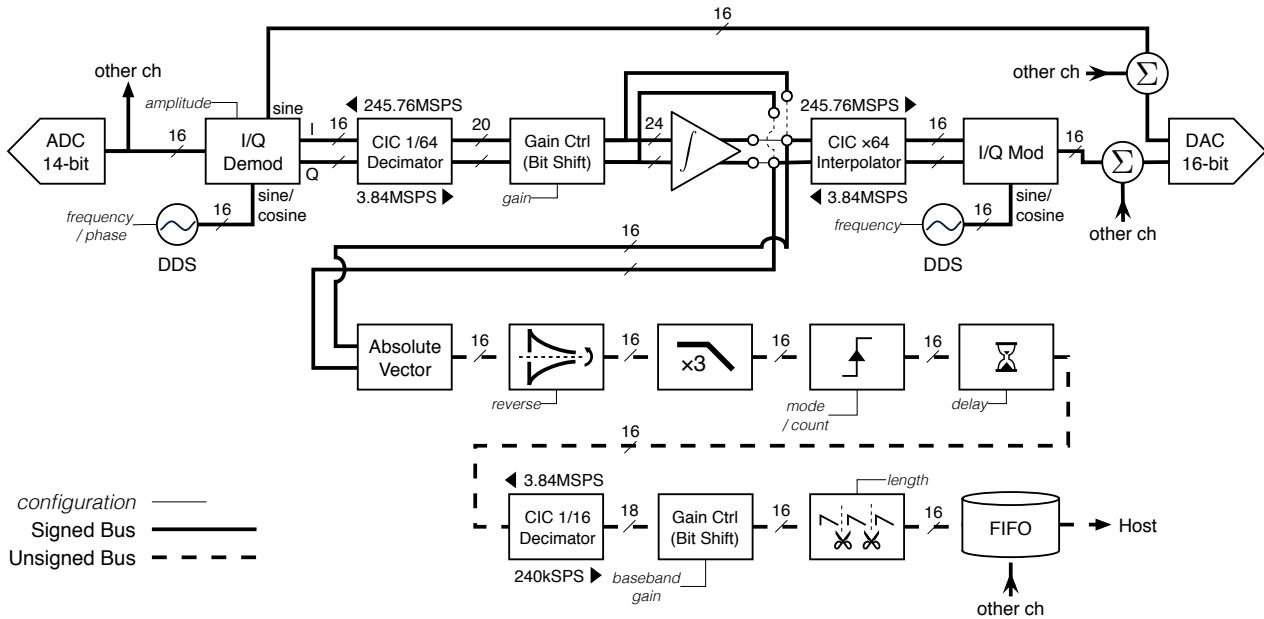


Fig. 4.7 Digital BBFB diagram

## 4.4 Design and Implementation

### 4.4.1 Core Logic

Figure 4.7 shows the overall block diagram (single-channel unit except ADC, DAC and FIFO) of a developed digital BBFB system. The incoming signal is digitized in 245.76 MspS by the ADC, and then spread to each channel unit. In analog electronics, a phase sensitive detector was used to demodulate, but we used an I/Q demodulator for a stable demodulation. The demodulated I and Q signals are decimated by 64 and down-sampled to 3.84 MspS. To filter out second harmonic generated at the I/Q demodulator, and to FLL, I and Q signals are integrated by the discrete-time integrator. To generate the feedback signal, both signals are interpolated by 64, up-converted to the carrier frequency, and modulate the phase-adjusted carrier at the I/Q modulator. The feedback signal is then summed up with other channel feedback signals, divided by the number of multiplexing channels, and finally converted to the analog signal by the DAC in 245.76 MspS.

The baseband signal, which is the absolute value of I and Q signals, is calculated by the coordinate rotation digital computer (CORDIC) algorithm. The baseband signal optionally flipped upside down, and then applied the 3rd-order low-pass filter. The signal is still just a digital stream, and to extract a pulse (and a noise) waveform, the signal is triggered by a threshold trigger, extracted preset number of points, and then transferred to the first-in-first-out (FIFO) buffer.

Here we elaborate more on each component.

#### I/Q Demodulator and Modulator

The I/Q demodulator takes the input signal data stream of 16-bit signed integer from the ADC, and sine/cosine data streams of 16-bit signed integer from a direct digital synthesizer (DDS), and multiplies them to produce the I and Q signals. Two least significant bits (LSB) of input signal is dummy (zero), since the ADC is 14-bit converter. The DDS is generated using the Xilinx DDS Compiler (ver. 4.0). The frequency and phase of the

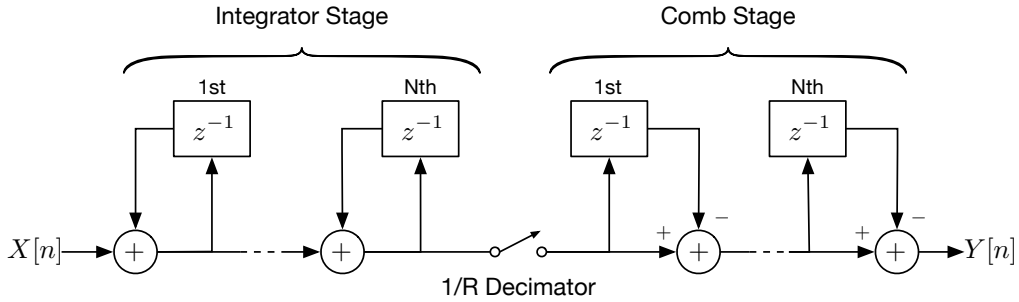


Fig. 4.8 CIC Decimator

DDS output are programmable, and the bit width of the frequency/phase register is 18 bits, which makes the frequency resolution to be  $\sim 1$  kHz ( $245.76$  MHz/ $2^{18}$ ), and the phase resolution to be  $\sim 2.4 \times 10^{-5}$  rad. The output bit width of the DDS is 16 bits, and therefore the spurious free dynamic range (SFDR) is 96 dB. The input signal and the sine/cosine signals are multiplied with the pipelined multiplier (3 stages) clocked in 245.74 MHz using the DSP48E1 hardware multiplier. The bit width of the product is 32 bits, and we extract 16 bits from 2nd most significant bit (MSB) as the I and Q signals, since the two MSB are both signed bits (unless both signals are  $-32768$ ), which makes the gain at this stage to be  $1/2$  if we cut off the higher frequency component. The sine signal from the DDS is also output for the carrier signal.

The I/Q modulator takes the I and Q input signal data stream of 16-bit signed integer, and sine/cosine data streams of 16-bit signed integer from another DDS, multiplies them, and finally sums up to produce the feedback signal. The DDS is identical to the I/Q demodulator DDS except that only the frequency is programmable. The output is extracted in the same manner.

The carrier signal and the feedback signal are summed up with other channel carrier signals and feedback signals, divided (arithmetic right shift) by the number of channels, or the output scaler, and transferred to the DAC.

#### CIC Decimator and Interpolator

The signal sampling rate, 245.76 Msps, is too fast to process for demodulated signals with a small bandwidth ( $< 1$  MHz), and therefore is down-sampled to a much smaller frequency, 3.84 Msps. The I and Q signals from the I/Q demodulator are decimated by 64 using a cascaded integrator-comb (CIC) filter. The CIC filter is efficient way to implement a combination of a simple boxcar filter (averaging filter) and a simple decimator (or simply a moving-average filter) [15]. It consists of three stages; an integrator stage, a  $1/N$  decimator, and a comb stage (Figure 4.8).

The transfer function of the CIC decimation filter is given by

$$H(z) = \left( \sum_{k=0}^{RM-1} z^{-k} \right)^N \quad (4.41)$$

$$= \left( \frac{1 - z^{-RM}}{1 - z^{-1}} \right)^N, \quad (4.42)$$

where  $R$  is the decimation (or interpolation) ratio,  $M$  is the differential delay, which is usually 1 or 2, and  $N$  is the number of stages in the filter. Figure 4.9 shows the frequency responses of the 3rd-order  $1/64$  CIC decimation filter for both  $M = 1$  and  $M = 2$  cases. In both cases, integral multiplications of  $f_s/R$ , where  $f_s$  is

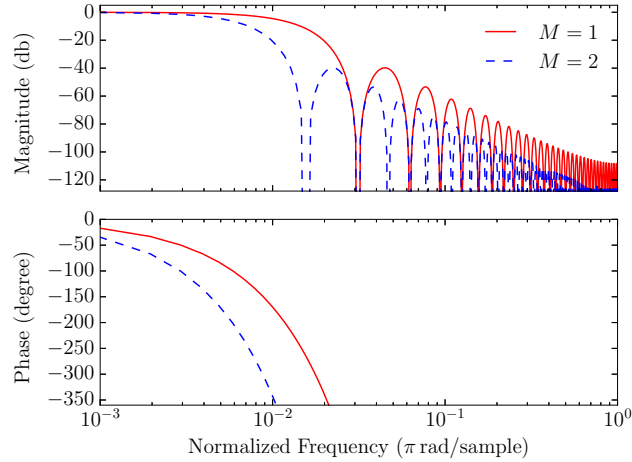


Fig. 4.9 Frequency responses of 3rd-order 1/64 CIC decimation filter

the sampling frequency, becomes zero, which suppresses the aliased spectral components due to the decimation (or interpolation). Therefore, the CIC filter is well-suited for anti-aliasing filtering.

The properly decimated signal is known to have a larger effective number of bits (ENOB), because of the improved SNR. The growth of ENOB,  $\Delta\text{ENOB}$ , after the decimation with the decimation rate  $R$  is given by

$$\Delta\text{ENOB} = \log_4 R, \quad (4.43)$$

therefore the ENOB increases by 3 bits when  $R = 64$ . As we are using the 3rd-order differential-delayed 1/64 decimation filter for the I and Q signals, the bit width after the decimation becomes 19 ignoring the fact that two LSB of incoming signals are dummy and that the actual ENOB of incoming signals are smaller than 14 due to noise. The decimation rate is also configurable to be 128, so we are making the bit width to be 20.

The CIC interpolator takes the integrated I and Q signal data stream of 16-bit signed integer clocked in 3.84 MHz and up-samples to 245.76 Msps. The output bit width remains 16.

#### Discrete-Time Integrator and Gain Control

The integrator is the key component for the FLL. In analog electronics, the integrator is a single op-amp integrator for a single channel, while it is a set of two discrete-time integrators for each I and Q signals in digital electronics. The integrator is actually a simple infinite impulse response (IIR) filter which transfer function is given by

$$H(z) = \frac{a}{1 - z^{-1}}, \quad (4.44)$$

where  $a$  is the gain parameter of the integrator. The gain parameter is programmable from  $2^{-4}$  to  $2^3$  in 8 steps using a barrel shifter. Figure 4.10 shows the frequency responses of the discrete-time integrator for  $a = 2^{-4}$ ,  $2^{-2}$ ,  $2^0$  and  $2^2$  cases. Unlike the analog integrator which DC gain is limited by the op-amp open-loop gain, the DC gain of the discrete-time integrator is infinity, and the carrier signal is thus almost completely suppressed (but limited by the ADC effective resolution) in the FLL loop.

The bit width of incoming I and Q signals to the gain control component is 20, and the gain control attenuates signals by  $2^4$  at a maximum, therefore the output bit width from the gain control is 24. The integrator then takes 24-bit signed integer data streams, integrates them, and outputs them as 16-bit signed integer data stream taking the 16 most significant bits.

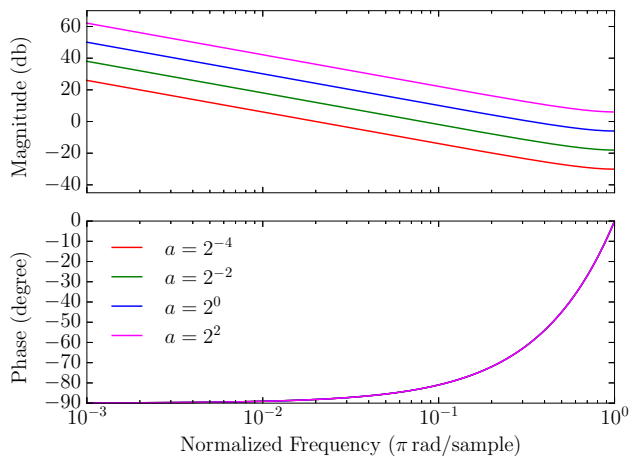


Fig. 4.10 Frequency responses of discrete-time integrator for various gains

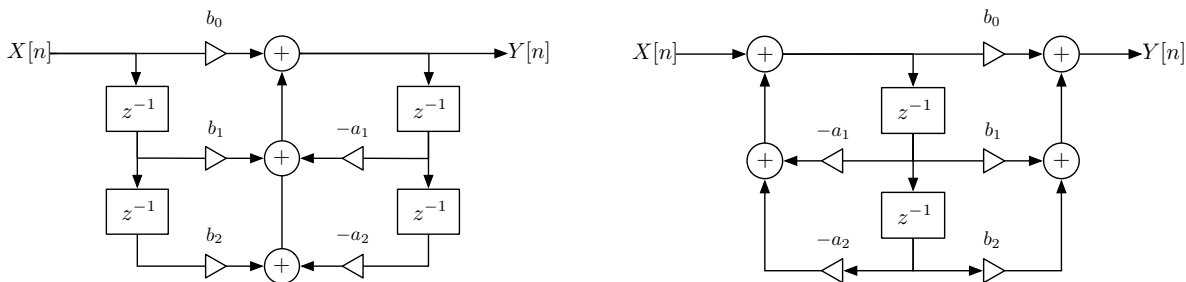


Fig. 4.11 Biquad filter implementations: direct form 1 (left) and direct form 2 (right)

**CORDIC**

To calculate the absolute value of the I and Q vectors, the CORDIC algorithm is used. It is a calculation technique to break trigonometric calculations to simple additions, subtractions, and bit shifts. The CORDIC is generated using the Xilinx CORDIC (ver. 4.0). It takes I and Q 16-bit signed integer data streams, calculates their absolute values, and output them as 16-bit unsigned integer data stream. Upon the calculation, the I and Q signals are normalized to be from  $-1 \leq (I \text{ or } Q) \leq 1$ , then the absolute value range becomes from 0 to 1, and finally it is scaled so that the absolute value 0 to be 0 and 1 to be  $2^{16} - 1$ .

**3rd-order LPF for Baseband**

The demodulated signal is filtered by the CIC decimator and the integrator, yet it may still include signals from neighbor channels. To filter out those undesired signals, the 3rd-order low-pass filter (LPF) is applied to the demodulated signal. The filter consists of cascaded IIR biquad filter (direct form 1). Figure 4.11 shows the two types of biquad filter implementations, the direct form 1 and the direct form 2. The transfer function of both types is the same, and is given by

$$H(z) = \frac{b_0 + b_1z^{-1} + b_2z^{-2}}{1 + a_1z^{-1} + a_2z^{-2}} \tag{4.45}$$

The direct form 2 is usually preferred since it uses less amount of delays, however, we used the direct form 1 that maximize the merit of the multiply accumulator (MACC) of the FPGA DSP core.

The filter can be designed to be many types of signal filters, including high-pass filters, band-pass filter, and so

Table 4.3 Baseband LPF design parameters

Filter type	Butterworth
Passband	1/64 ( $\pi$ rad/sample) (30 kHz)
Stopband	1/16 ( $\pi$ rad/sample) (120 kHz)
The maximum loss in the passband	3 (dB)
The minimum attenuation in the stopband	20 (dB)

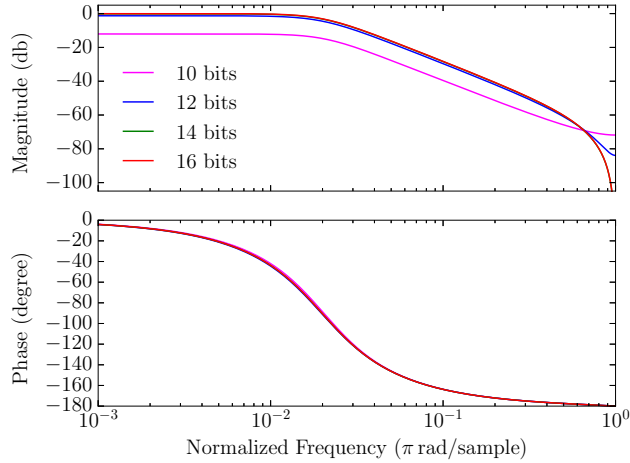


Fig. 4.12 Frequency responses of biquad low-pass filter for various fraction bits

on. It can be also designed to be several types of LPF, such as Chebyshev filters and elliptic filters. We designed our biquad low-pass filter to be a simple Butterworth filter as in Table 4.3, and the coefficients are

$$b_0 = 0.00093078, \quad (4.46)$$

$$b_1 = 0.00186157, \quad (4.47)$$

$$b_2 = 0.00093078, \quad (4.48)$$

$$a_1 = -1.91177368, \quad (4.49)$$

$$a_2 = 0.91549682. \quad (4.50)$$

To implement the filter in digital, the coefficients need to be quantized. Figure 4.12 shows the frequency responses of the filter for various fraction bits. The smaller bits cause inconsistencies from the ideal transfer function, therefore we used 16 bits for fraction bits.

Figure 4.13 shows the frequency response of the 3rd-order low-pass filter for the baseband signal. Both input and output signals to the filter are 16-bit unsigned integers.

#### Trigger, Baseband Decimation and Waveform Extract

The baseband signal is still the data stream, and pulses (and noises) need to be triggered and extracted. The trigger is a simple threshold trigger. The trigger direction can be configured in both directions.

The signal stream through the trigger can be changed to the 1st-order derivative or 2nd-order (pseudo-) derivative of the 2-point or 4-point averaged signal. The 2-point 1st-order derivative filter is a convolution of a 2-point moving average filter and a simple derivative filter which transfer function is given by

$$H(z) = 1 - z^{-1}, \quad (4.51)$$

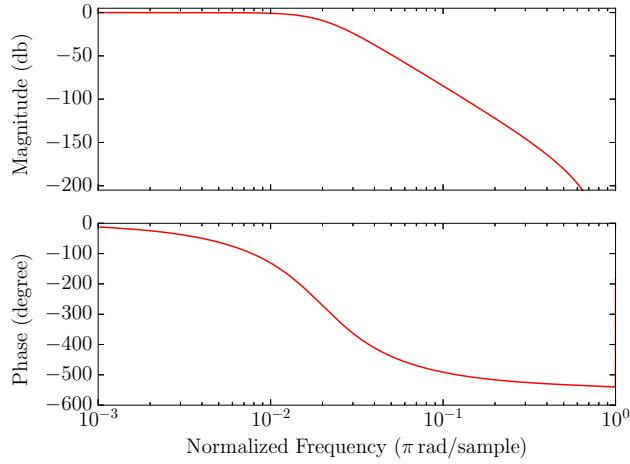


Fig. 4.13 Frequency response of 3rd-order low-pass filter

and its transfer function is given by

$$H(z) = 0.5 - 0.5z^{-2}. \quad (4.52)$$

Similarly the transfer function of 4-point 1st-order derivative filter is given by

$$H(z) = 0.25 - 0.25z^{-4}. \quad (4.53)$$

The 2nd-order derivative filters are a convolution of moving average filters and a 2nd-order pseudo-derivative filter which transfer function is given by

$$H(z) = 1 - z^{-1} - z^{-2} + z^{-3}, \quad (4.54)$$

while that of ideal 2nd-order derivative filter is given by

$$H(z) = 1 - 2z^{-1} + z^{-2}. \quad (4.55)$$

The reason for the pseudo-derivative filter is to reduce the number of calculations. The transfer functions of 2-point and 4-point 2nd-order pseudo-derivative filters are given by

$$H(z) = 0.5 - z^{-2} + 0.5z^{-4} \quad (2 \text{ points}), \quad (4.56)$$

$$H(z) = 0.25 - 0.25z^{-2} - 0.25z^{-4} + 0.25z^{-6} \quad (4 \text{ points}), \quad (4.57)$$

respectively. However, to further reduce the number of calculations for (4.57), we merged the second and the third terms and obtained

$$H(z) = 0.25 - 0.5z^{-3} + 0.25z^{-6}.$$

The sampling rate of the baseband signal after the low-pass filter is 3.84 Msps. However, the effective signal bandwidth is far smaller. To reduce the data rate, we further decimate the baseband signal by 16, and the sampling rate after the decimation becomes 240 kps which Nyquist frequency is the same as the stopband of the

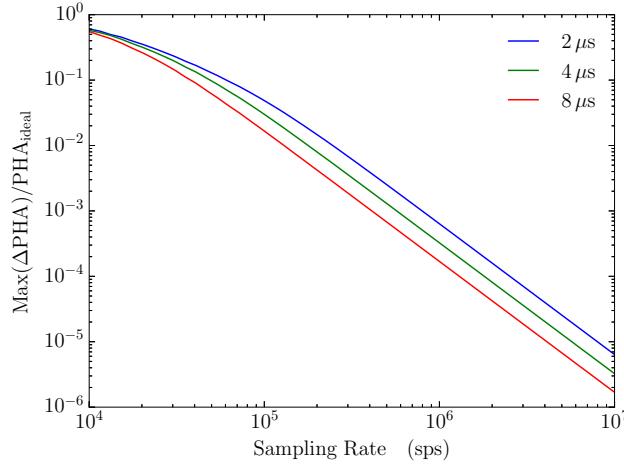


Fig. 4.14 Dispersion of pulse heights (PHA) vs. sampling rates for various pulse rise times

low-pass filter. However, the trigger has to be applied before the decimation. Figure 4.14 shows the simulation results of a dispersion of pulse heights as a function of sampling rate for various pulse rise times. 10,000 noiseless pulses which pulse height is fixed to 1.0 but rise timings are varied within a single sampling clock were simulated, and then the maximum values for each pulse were taken as pulse heights. The fall time and the length of pulses are fixed to  $200\ \mu\text{s}$  and  $2\ \text{ms}$ , respectively.  $\Delta\text{PHA}$  is calculated as  $\Delta\text{PHA} = |\text{PHA}_{\text{ideal}} - \text{PHA}|$ , where  $\text{PHA}_{\text{ideal}} = 1.0$ . To achieve the required energy resolution ( $2\ \text{eV}$  @  $2\ \text{keV}$ ), the dispersion needs to be suppressed less than  $10^{-3}$ , therefore the sampling rate for triggering should be 1 Msp/s or more. For this reason, the decimation needs to be done after triggering.

The data stream of the baseband signal from the trigger component passes through the delay component, which delays the signal by a given amount of 3.84 MHz clocks for a positive trigger position, and then gets decimated by 16. The decimator is always reseted upon the trigger signal to align the extracted pulses. The bit width increases by 2 bits here, and the following gain control aligns the width to 16 bits. Finally a pulse (or noise) waveform is extracted into a local buffer from the signal stream with a given amount of data length chosen from 256, 512, 1024 or 2048 points, which corresponds to 1, 2, 4 or 8 ms length, and then flushed to the FIFO. A very little time during the data flush from the local buffer to the FIFO becomes a dead time. The flush is done in the 245.76 MHz clock, so the maximum dead time in the worst case is  $(\text{data length})/245.76\ \text{MHz} \times (\text{number of channels} - 1)$ , and is  $\sim 3\ \mu\text{s}$  for the 16-channel multiplexing 512-point configuration. If the dead time is critical, it can be completely avoided by adding another local buffer to do double buffering, yet it obviously requires more hardware resources.

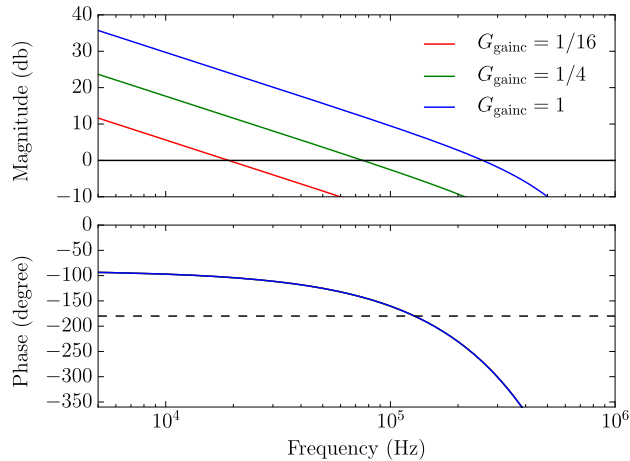
The data sizes for each data length, 256, 512, 1024 and 2048 points, are 512, 1024, 2048 and 4096 bytes, respectively. The data rate is therefore  $\sim 500\ \text{KB/s}$  per channel at maximum, and the system overall data rate for 16-channel multiplexing is  $\sim 8\ \text{MB/s}$  at maximum. However, the required maximum count rate is far less in astronomical applications. If we assume the required count rate to be 100 cps, which is still very large, the data rate per channel becomes  $\sim 100\ \text{KB/s}$ , and the system data rate for 16-channel multiplexing therefore becomes  $\sim 1.6\ \text{MB/s}$ , which is reasonably small even for resource-limited satellite applications.

#### 4.4.2 System Overall Gain

The overall gain in the flux-locked loop in this digital system is the sum of gains of the I/Q demodulator, the CIC decimator, the gain control, the integrator, the CIC interpolator, the I/Q modulator, and the signal divider right before the DAC. The gains at each stage is summarized in Table 4.4. Figure 4.15 shows the overall frequency

Table 4.4 Gains at each FLL stage

Stage		Gain	DC (Carrier) Gain
I/Q Demodulator	$G_{\text{demod}}$	1/2	1/2
CIC Decimator	$G_{\text{dec}}$	$ H_{\text{dec}}(\omega) $	1
Gain Control	$G_{\text{gainc}}$	1/16, 1/8, 1/4, 1/2, 1, 2, 4, or 8 (programmable)	$\leftarrow$
Integrator	$G_{\text{int}}$	$ H_{\text{int}}(\omega) $	$\infty$
CIC Interpolator	$G_{\text{interp}}$	$ H_{\text{interp}}(\omega) $	1
I/Q Modulator	$G_{\text{mod}}$	1	1
Signal Divider	$G_{\text{div}}$	1/16, 1/8, 1/4, 1/2, or 1 (programmable)	$\leftarrow$

Fig. 4.15 Overall gain in the digital electronics for various gain parameters ( $G_{\text{div}} = 1$ )

response for various  $G_{\text{gainc}}$  values. As we see in the figure, the overall gain is well-determined by the integrator.

### 4.4.3 Interface

Extracted pulse and noise waveforms in the FIFO need to be transferred to a host machine. There are several ways to achieve it, and we use a system-on-chip (SOC) design with the LEON processor. The LEON processor was originally developed by the European Space Agency (ESA), and now is developed and supported by Gaisler Research. It is a 32-bit CPU microprocessor core, based on the SPARC-V8 RISC architecture and instruction set. Figure 4.16 shows our SoC design.

The custom module, the BBFB controller, is attached to the advanced peripheral bus (APB), which is bridged to the advanced high-performance bus (AHB) at the AHB/APB bridge and then connected to the processor (Figure 4.17). The core logic extracts pulse and noise waveforms and transfer them to the FIFO in the BBFB controller. Once waveform data is available in the FIFO, the controller generates an interrupt and demands the processor to pull the waveform data. The hardware registers for configuration parameters are memory-mapped in the 32-bit physical address space. Table 4.5 shows the excerpted memory-mapped hardware configuration parameters. The complete list of the parameters and registers is in Appendix B.

The SoC runs Linux (2.6) as an operating system. Figure 4.18 show the application stack. As the processor is interrupted, the data in the hardware FIFO is pulled to the software FIFO in the kernel driver. The waveform data can be accessed from the user space through the device file, and configuration registers can be accessed through the sysfs. The measured throughput from the hardware FIFO to the user space is  $\sim 11$  MB/s, which is large enough for the estimated required system data rate, 1.6 MB/s.

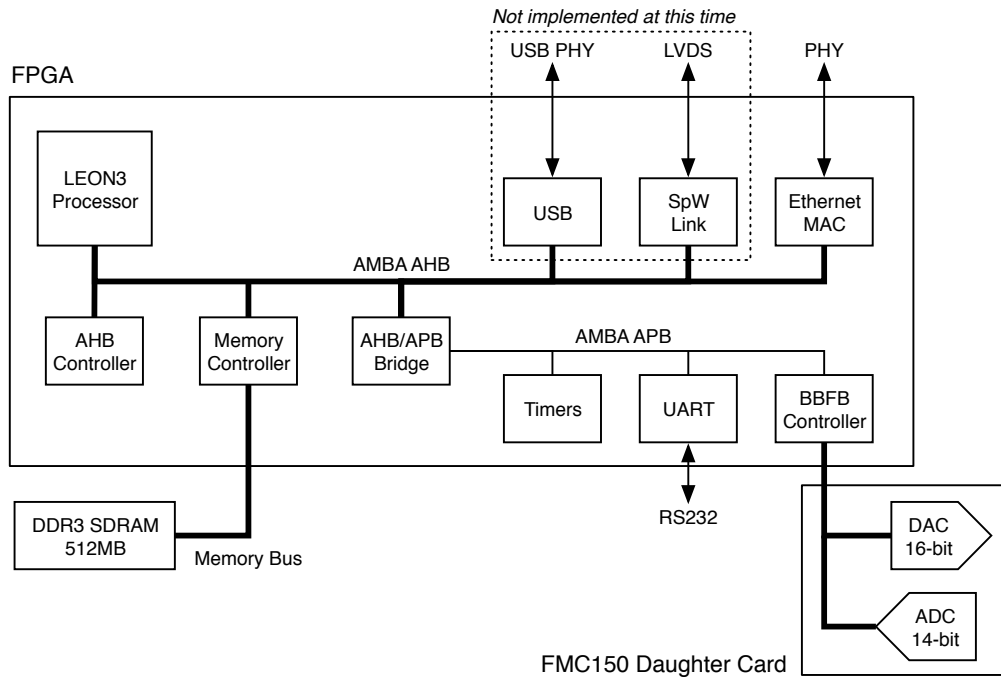


Fig. 4.16 SoC design with LEON3 microprocessor

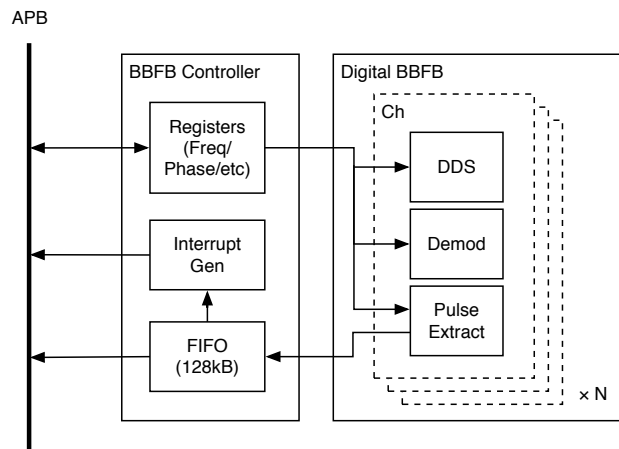


Fig. 4.17 The BBFB controller attached to the APB

Remote clients on the same network (or even other networks) can access waveforms and registers by XML-RPC connecting a server running on the user space. Figure 4.19 shows the developed client software, the TES Workbench. It connects to the server, which is running on the FPGA, pulls waveforms, and saves them to a database file on a local machine. It can also control all the hardware parameters from the GUI.

#### 4.4.4 Resource Utilization

Figure 4.20 shows the resource usage of the FPGA. It shows the usage only by the core logic. The block RAM/FIFO usage is higher even for the smaller number of channels due to the 64kB hardware FIFO. Since the resource usage for the LEON3 SoC is fairly small (Table 4.6), we can implement up to 32 channels within the

Table 4.5 Excerpted hardware configuration parameters. The complete list of parameters and addresses is in Appendix B.

Parameter Name	Register Name	R/W	Bit width
Device Control Parameters			
Reset	Device Control	WO	1
IRQ Enable		RW	1
Record Length		RW	2
Trigger Delay		RW	8
FIFO Count	Device Statistics	RO	16
Previous Trigger	Trigger Threshold	RW	16
Next Trigger		RW	16
FIFO Data	FIFO	RO	32
Channel Control Parameters			
Enable	Channel Control 1	RW	1
Clear		RW	1
Feedback Enable		RW	1
Integrator Enable		RW	1
Trigger-Level/Count Select		RW	1
Frequency/Phase Select		RW	1
Baseband Gain		RW	2
Modulation Enable		RW	1
Derivation Mode		RW	2
Trigger Mode		RW	4
Gain		RW	3
Amplitude		RW	12
Frequency/Phase	Channel Control 2	RW	16
Trigger-Level/Count		RW	16
Trigger Count	Channel Statistics	RO	16

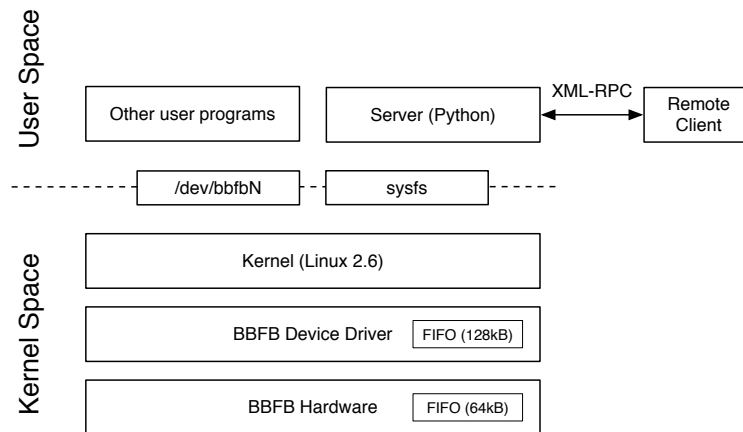


Fig. 4.18 Application stack on the SoC

Table 4.6 The FPGA resource usage by the LEON3 SoC

	Usage
Slice Registers	4%
Slice LUTs	11%
Block RAM/FIFO	4%
DSP48E1	1%

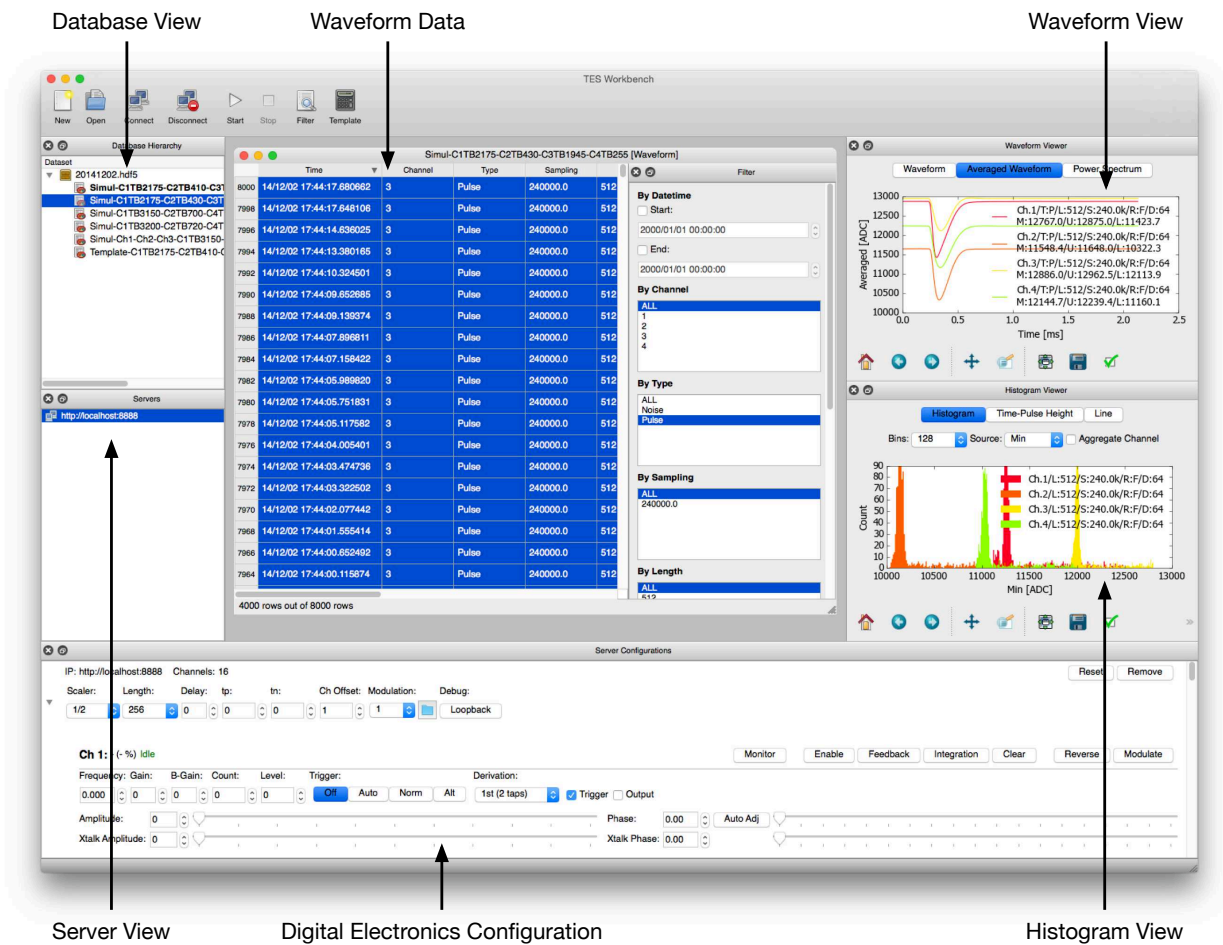


Fig. 4.19 TES Workbench

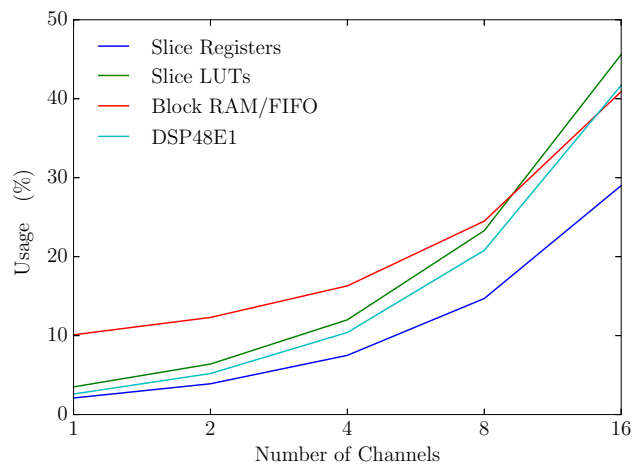


Fig. 4.20 Resource utilization for various number of channels

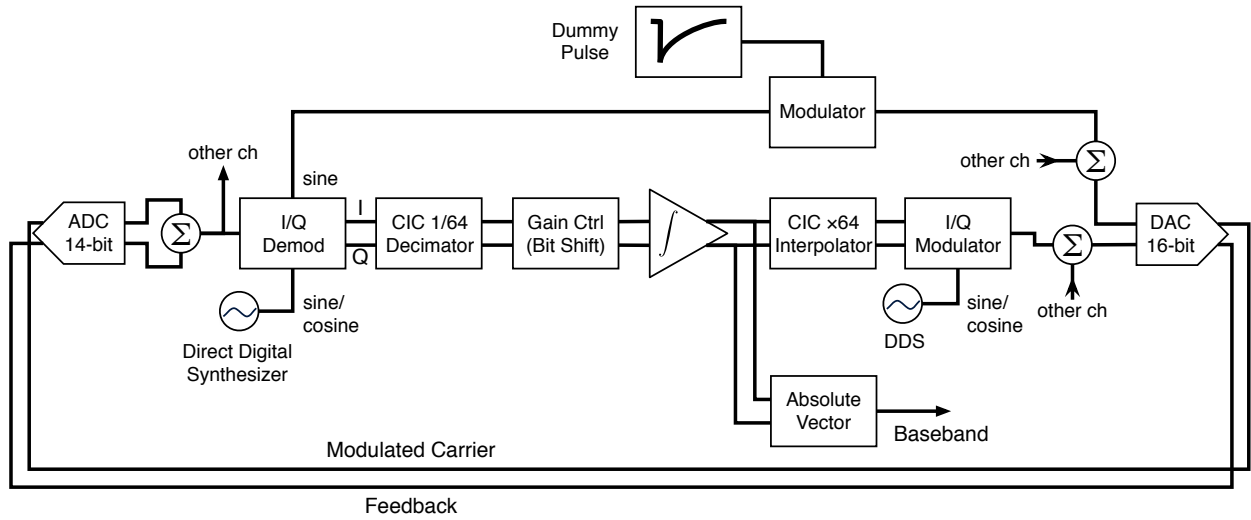


Fig. 4.21 Loopback mode

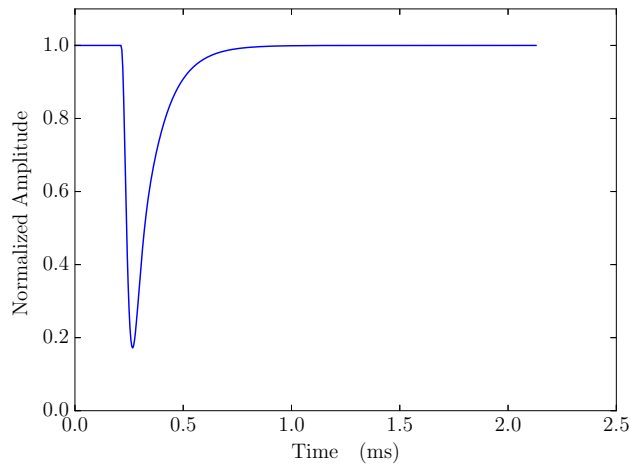


Fig. 4.22 Dummy pulse used to modulate in the loopback test

single FPGA.

## 4.5 Loopback Test

We evaluated the developed digital electronics in a loopback mode (Figure 4.21). In the loopback mode, the DAC outputs are directly connected to the ADC inputs, and the carrier and the feedback are individually sampled by the ADC, then digitally summed.

### 4.5.1 SNR Evaluation

The TES bias for the target channel is modulated by a 2-ms dummy pulse (2  $\mu$ s rise time, 200  $\mu$ s fall time, and 80% modulation) shown in Figure 4.22, while other channels are not modulated. We used carrier frequencies from 5 to 7 MHz with 128 kHz spacing frequency.

The SNR, which is given by  $\Delta PHA/PHA$ , was calculated from the result of optimal filtering with 16,000

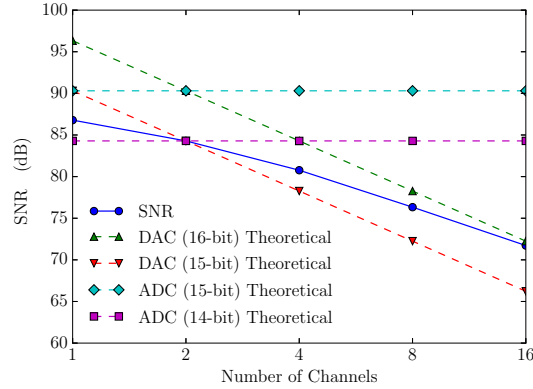


Fig. 4.23 The obtained signal-to-noise ratio in the loopback test

Table 4.7 FMC150 delay caused by the internal interpolation

	Delay ( $\mu\text{s}$ )
No interpolation	0.27
$\times 2$ interpolation	0.40
$\times 4$ interpolation	0.68

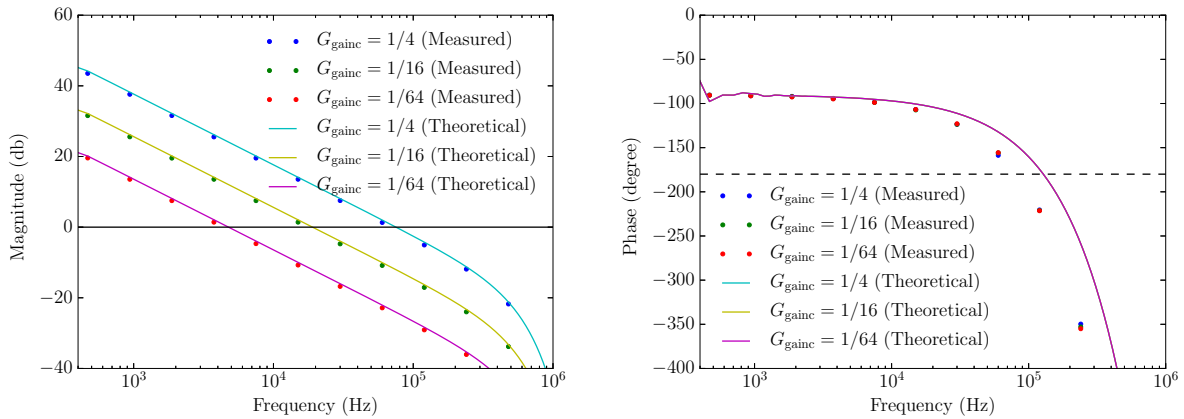


Fig. 4.24 The measured and theoretical frequency responses in the single channel loopback mode for various gain parameters

pulses and noises (Figure 4.23). The obtained SNR for 16-channel multiplexing is  $\sim 72$  dB achieving the required SNR ( $> 60$  dB). Figure 4.23 also shows theoretical SNRs of ADC and DAC, and infers that the system SNR is limited by the DAC SNR for higher-density multiplexing as expected. If a higher SNR is needed, we can increase the number of DAC to decrease the number of channels sharing a single DAC channel to output carriers and feedbacks.

#### 4.5.2 Loopgain Evaluation

We first measured the delay caused by the FMC150. Table 4.7 shows the delay caused by the internal interpolation of the DAC. When  $\times 4$  interpolation is enabled, the delay is almost doubled. As the sampling rate for both ADC and DAC is 245.76 Msps that is much higher than the signal frequency ( $< 10$  MHz), therefore we do not use the interpolation. We then measured the frequency responses (amplitude and phase).

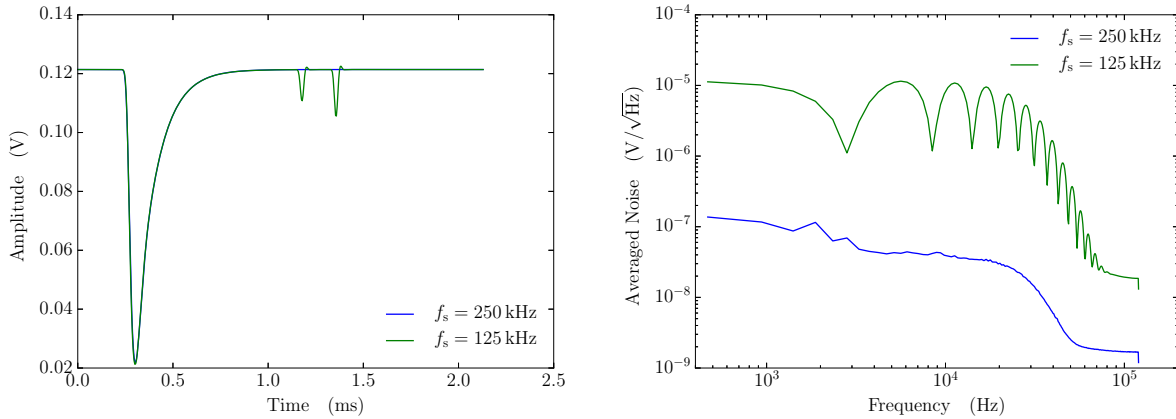


Fig. 4.25 The averaged pulses (left) and the averaged noises (right) for various spacing frequencies

Figure 4.24 shows the measured frequency responses of demodulated signals in the single channel loopback mode for various gain parameters along with the theoretical responses. While they show good agreement in magnitude, the measured phases roll off in smaller frequency than the theoretical phases, meaning that there is further delay in the system. The horizontal dashed line shows where the phase is  $-180^\circ$ , and the gain margins are therefore  $-26.6$  dB,  $-14.6$  dB, and  $-2.6$  dB for  $G_{\text{gainc}} = 1/64$ ,  $1/16$  and  $1/4$  in  $G_{\text{div}} = 1$ , respectively. The unity-gain bandwidths are 4.3 kHz, 17.1 kHz and 66.8 kHz, for  $G_{\text{gainc}} = 1/64$ ,  $1/16$  and  $1/4$ , respectively, while the phase margin is  $\sim 60^\circ$  for all the cases, which still leaves enough room for other delays.

### 4.5.3 Crosstalk Evaluation

In four channel multiplexing mode, we setup three channels with carrier frequencies, 5.25, 5.50, 5.75 MHz, and modulated all the channels with the dummy pulse. We collected pulses and noises for the middle channel, and calculated the averaged pulse. Next we changed the spacing frequency from 250 kHz to 125 kHz, therefore changed the carrier frequencies to 5.375, 5.500, 5.625 MHz, and collected the pulses and noises for the middle channel to calculate the averaged pulse. Figure 4.25 shows the obtained averaged pulses and averaged noises for the spacing frequencies 250 kHz and 125 kHz. We clearly see crosstalk for the averaged pulse with  $f_s = 125$  kHz from the neighbor channels. The average noise of  $f_s = 125$  kHz is also considerably higher. The gain control was set to  $G_{\text{gainc}} = 1/2$  while the signal divider was set to  $G_{\text{div}} = 1/4$ . It makes the equivalent gain to be  $1/8$  in the single channel mode, and the unity-gain bandwidth is therefore  $\sim 35$  kHz. Despite the frequency margin of  $\sim 50$  kHz even for the 125 kHz spacing frequency, the crosstalk is not negligible.

We thus varied the gain control and collected pulses and noises for the  $f_s = 125$  kHz case. Figure 4.26 shows the averaged pulses (left) and the averaged noise (right) for  $G_{\text{gainc}} = 1/2$ ,  $1/4$ ,  $1/8$  and  $1/16$ . Although the crosstalk becomes less noticeable when  $G_{\text{gainc}} \leq 1/4$  for averaged pulse, the noise level for  $G_{\text{gainc}} = 1/4$  is still higher. For  $G_{\text{gainc}} \leq 1/8$ , the noise drops to the usual level.

The crosstalk, of course, happens when more than two photons hit adjoining TES channels almost simultaneously, and it should be very rare in astronomical applications where the typical count rate is very small. However, when the count rate is expected to be very high, the spacing frequency has to be sufficiently large, otherwise the loopgain needs to be undesirably small.

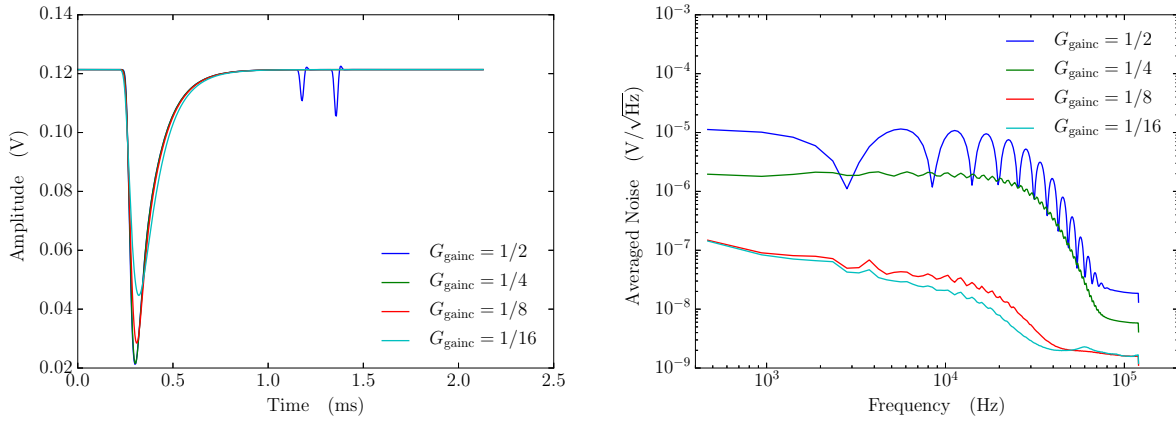


Fig. 4.26 The averaged pulses (left) and the averaged noises (right) for various gain parameters ( $f_s = 125$  kHz,  $G_{\text{div}} = 1/4$ )

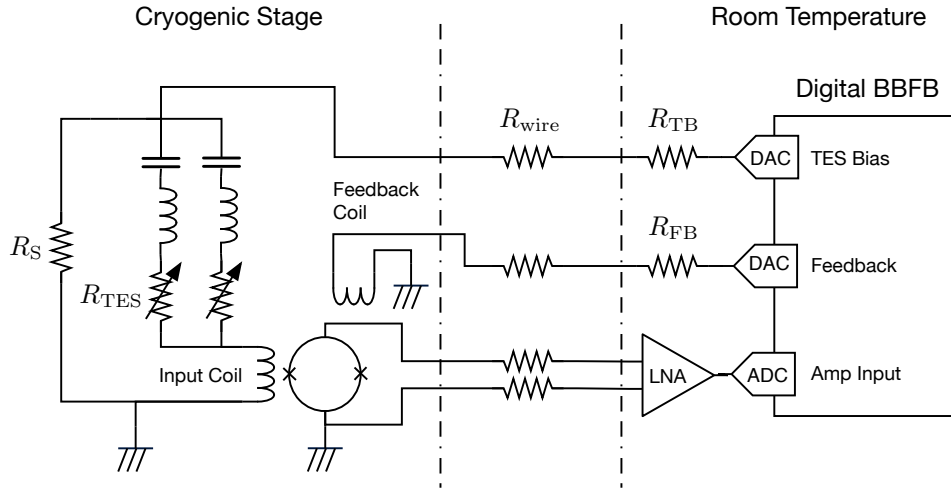


Fig. 4.27 A typical experimental setup for a TES multiplexed readout

## 4.6 Development of Analog Front-End

### 4.6.1 Requirements for Analog Front-End

The output voltage range of the DAC on FMC150,  $1 V_{\text{pp}}$ , is too small to use as a voltage source for TES biasing and the feedback. Figure 4.27 shows a typical experimental setup for a TES readout using the developed digital system. The typical Ti/Au TES operating resistance,  $R_{\text{TES}}$ , is  $\sim 50 \text{ m}\Omega$ , while the TES shunt resistance,  $R_S$ , is  $\sim 5 \text{ m}\Omega$ . This makes the separation ratio of the TES bias current,  $I_{\text{TB}}$ , to be  $I_{\text{TES}} : I_S \approx 1 : 10$ , where  $I_{\text{TES}}$  is the TES current, and  $I_S$  is the shunt current. The typical TES current at the operating point is  $\sim 50 \mu\text{A}_{\text{rms}}$ , meaning that the TES bias current needs to be  $500 \mu\text{A}_{\text{rms}}$  or larger for single channel biasing. Suppose that we multiplex 16 TES signals, then  $I_{\text{TB}}$  can be as large as  $8 \text{ mA}_{\text{rms}}$ . To make such a current flow with the  $1 V_{\text{pp}}$  voltage source, the bias resistance becomes  $\sim 45 \Omega$ , which is smaller than the typical wire resistance,  $\sim 100\text{--}200 \Omega$ , between the cryogenic stage and the room temperature electronics. In other words, the output impedance of the current

Table 4.8 Requirements for analog front-end

Low-Noise Amp	
Gain	46 dB
Bandwidth	DC – 20 MHz
Equivalent input voltage noise	$< 2 \text{ nV}/\sqrt{\text{Hz}}@1 \text{ MHz}$
Input bias current	$< 1 \text{ nA (abs.)}$
Input impedance	$1 \text{ M}\Omega@DC$
Output impedance	$50 \Omega$
V/I Converter	
Output impedance	$> 10 \text{ k}\Omega@1 \text{ MHz}$

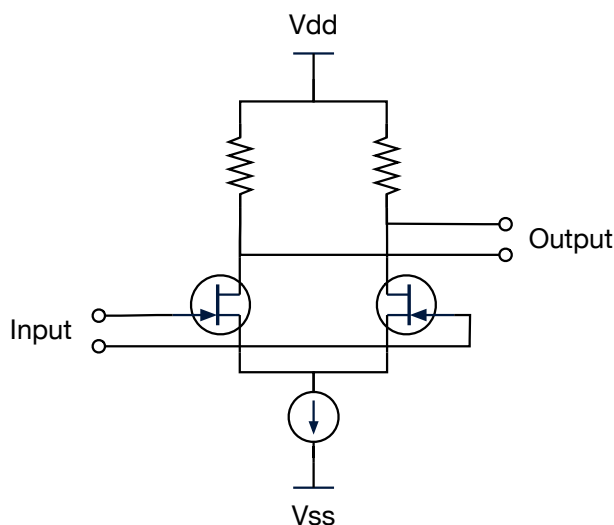


Fig. 4.28 The circuit schematic of typical FET differential amplifier

source is too small.

For a low-noise amp, we have been using ultra-low-noise FET-input differential preamplifier SA-421F5 by NF corporation. It has the very small equivalent input voltage noise of  $0.5 \text{ nV}/\sqrt{\text{Hz}}$  ( $> 100 \text{ kHz}$ ), and the very small equivalent input current noise of  $100 \text{ fA}/\sqrt{\text{Hz}}$ , thus is well suited for SQUID readout. Moreover, it has the very wide bandwidth of 30 to 30 MHz, thus can be used for FDM. However, its input is AC-coupled, and has therefore no sensitivity to very slow signal variations, such as temperature drift.

For those reasons, we started to develop an analog front-end which is inserted in between the cryogenic electronics and the digital system. The requirements for the analog front-end are summarized in Table 4.8. Since our SQUID is biased with a very small current ( $< 20 \mu\text{A}$ ), the input bias current of low-noise amp needs to be as small as possible, preferably less than 1 nA. The typical TES noise,  $20 \text{ pA}/\sqrt{\text{Hz}}$  and the typical SQUID gain,  $100 \text{ V/A}$ , make the SQUID output voltage noise to be  $2 \text{ nV}/\sqrt{\text{Hz}}$ . The equivalent input voltage noise of the analog front-end should be therefore less than  $2 \text{ nV}/\sqrt{\text{Hz}}$ .

#### 4.6.2 Design and Implementation

The complete circuit diagram and PCB layout of the analog front-end are available in Appendix B.

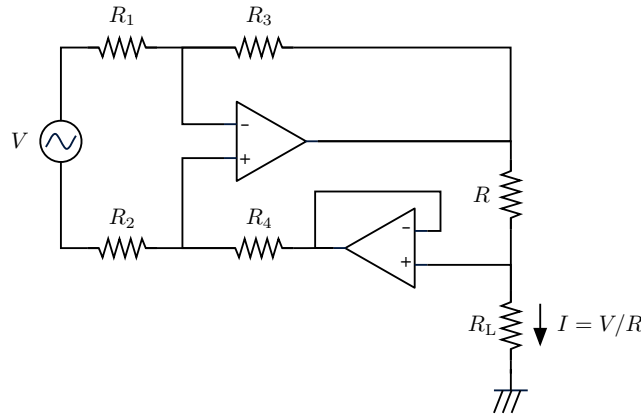


Fig. 4.29 The circuit schematic of the V/I converter based on the op-amp differential amplifier

### Low-Noise Amp (LNA)

To realize a differential amplifier with such a small input bias current, N-channel J-FET is generally used for the input of the first stage. Figure 4.28 shows the circuit schematic of typical FET differential amplifier. For DC amplifier, two FET should be thermally coupled to suppress temperature drift and distortion. Toshiba 2SK389, dual J-FET monolithic N-channel, is historically used for this type of application, although it has been discontinued. Linear Integrated Systems, however, now provides LSK389, which is a drop-in replacement for 2SK389, so we adopted it in this design. The LSK389 (and 2SK389) has a moderate input capacitance of 25 pF, but it can be much larger due to the mirror effect when the gain at this stage is large. We therefore made the gain to be 6 dB.

For the second stage, we adopted a 40 dB op-amp differential amplifier using the AD8099 by Analog Devices Inc. Thanks to its small noise level of  $0.95 \text{ nV}/\sqrt{\text{Hz}}$ , the second stage does not add more noise even though the gain of the first stage is small.

### V/I Converter

Figure 4.29 shows the circuit schematic of typical op-amp V/I converter. When  $R_1 = R_2 = R_3 = R_4$ , the current through the load resistor,  $R_L$ , is only determined by  $V$  and  $R$  and given by  $I = V/R$  regardless to the resistance value at  $R_L$ . When  $R_L$  is zero, the op-amp does not amplify the input. When  $R_L$  is non-zero, the op-amp amplifies the input so that the output voltage of the op-amp,  $V_{\text{out}}$ , becomes

$$V_{\text{out}} = \frac{R + R_L}{R} V. \quad (4.58)$$

Therefore, the op-amp gain in the circuit is given by  $(R + R_L)/R$ , and it limits the maximum load resistance.

In our case, the resistance  $R$  can be as small as  $50 \Omega$ , while the typical wire resistance is  $\sim 200 \Omega$ , which makes the op-amp gain to be 5. The maximum input to the op-amp is  $1 V_{\text{pp}}$ , and the maximum output is therefore  $5 V_{\text{pp}}$  when the gain is 5. As a result, the  $\pm 5 V$  power supply is sufficient.

The output current resolution is generally determined by the input bias current of the op-amp used as a voltage-follower. We selected the Analog Devices' ADA4817-2, which is dual unity-gain stable op-amp with FET inputs. The typical input bias current is 2 pA, which is small enough for our application where the typical current.

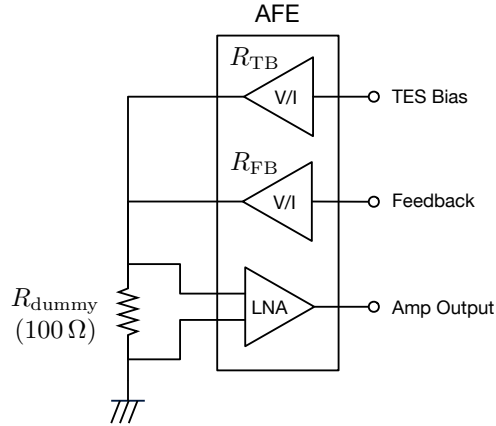


Fig. 4.30 The analog front-end measurement setup

#### Other Features

To suppress the low-frequency signal variation in the SQUID output, the DC FLL circuit is also implemented. For the integrator we adopted the famous Texas Instruments' OPA627, which has very small bias current and voltage offset and is well-suited for a precision integrator. The time constant is set to  $\sim 150 \mu\text{s}$ .

The current source for the SQUID bias is also implemented. It is just a  $51 \text{ k}\Omega$  resistor and a voltage source using DAC.

To control the parameters of DC FLL circuit, the Atmel AVR microcontroller, AT90USB162, is also on board. The parameters can be adjusted from a host computer connected to the front-end circuit by an USB cable. To suppress the noise from the clock, the microcontroller falls into the sleep mode and stops the clock when the USB cable is disconnected. Moreover, a dual channel slow speed ADC is also on board to read the amplified SQUID output for obtaining  $\Phi$ - $V$  characteristics when adjusting the operating point.

#### PCB Layout

The PCB was designed for the four-layered board. Figure C.2 in Appendix C shows the PCB layout of the component side and the solder side. The inner two layers are for  $+5 \text{ V}$  and  $-5 \text{ V}$ .

#### 4.6.3 Measurements

We have measured the gain and the noise of the developed analog front-end. Figure 4.30 shows the measurement setup. The TES bias and the feedback outputs were connected to a  $100 \Omega$  dummy resistor,  $R_{\text{dummy}}$ , which mocks a SQUID with the transimpedance gain of  $100 \text{ V/A}$ .

We first measured the loopgain for the TES bias line. The TES bias resistor,  $R_{\text{TB}}$ , was set to  $100 \Omega$ . During the measurement, the feedback output was disconnected from the dummy resistor. We used the Ojisankoubou APB-3 for the loopgain measurement. Figure 4.31 shows the measured gain (left) and the phase (right). As we used  $100 \Omega$  resistors for both  $R_{\text{TB}}$  and  $R_{\text{dummy}}$ , the gain is only due to the low-noise amplifier, which is  $40 \text{ dB}$  ( $50 \Omega$  terminated). We then measured the loopgain for the feedback line. The feedback resistor,  $R_{\text{FB}}$ , was set to  $1 \text{ k}\Omega$ . The measured gain and the phase are shown in the same figure. Now the feedback resistor is ten times larger than the dummy resistor, the gain becomes ten times smaller  $20 \text{ dB}$ . The cut off frequency for both is  $\sim 20 \text{ MHz}$ , while the gain for the TES bias line shows some kinks for the frequency more than  $10 \text{ MHz}$ , which may be due to the voltage-to-current converter with the large current output as it can not be seen in the feedback

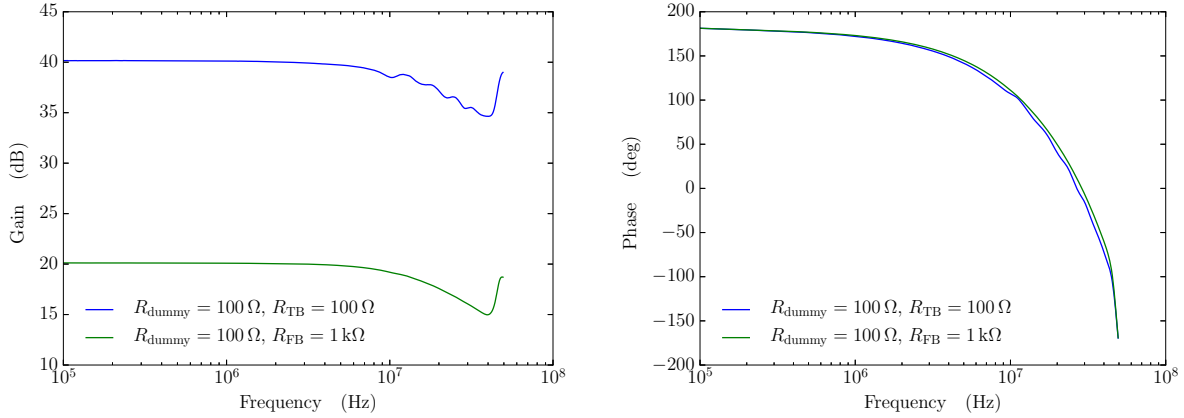


Fig. 4.31 The measured gain (left) and phase (right) of the analog front-end

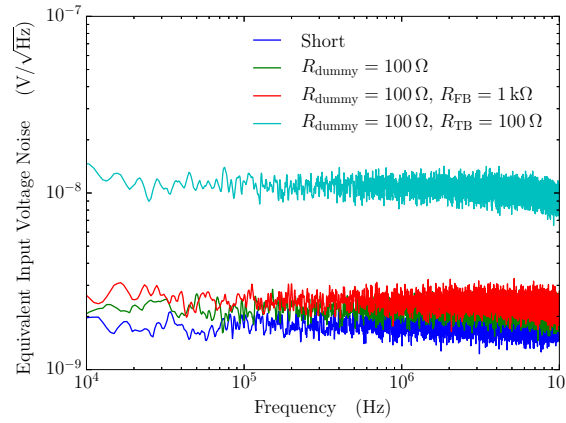


Fig. 4.32 The measured noises for various configurations

line. Since we are not planning to use that frequency range, it should not be an issue.

We then measured the noise with various configurations using the APB-3. We first measured the noise of the low-noise amplifier itself by shortening the inputs. Figure 4.32 shows the result in the frequency range of 10 kHz to 10 MHz. The measured noise is converted to the equivalent input voltage noise by dividing the output by the amplifier gain. It shows a flat frequency response, and the average in this frequency range is  $1.8 \text{ nV}/\sqrt{\text{Hz}}$ , which satisfies the requirement. Next we attached the  $100 \Omega$  dummy resistor to the LNA inputs and measured the noise. The result is shown in the same figure, and the average is  $2.2 \text{ nV}/\sqrt{\text{Hz}}$ , which is consistent with the expected noise level assuming the Johnson-Nyquist noise of the  $100 \Omega$  resistor as  $1.3 \text{ nV}/\sqrt{\text{Hz}}$ . We then connected the feedback output to the dummy resistor and measured the noise. The feedback resistor was set to  $1 \text{ k}\Omega$ , and the feedback input, which is internally  $50 \Omega$  terminated, was left disconnected. The average is  $2.4 \text{ nV}/\sqrt{\text{Hz}}$ . We finally connected the TES bias output (and disconnected the feedback output) and measured the noise. The TES bias resistor was set to  $100 \Omega$ . The average is  $10.3 \text{ nV}/\sqrt{\text{Hz}}$ . This means that the voltage noise (before converted to current) for both the TES bias output and the feedback output is  $10 \text{ nV}/\sqrt{\text{Hz}}$ . As the feedback output is reduced by one tenth, the expected noise when the feedback output is connected to the dummy resistor is  $\sqrt{(2.2 \text{ nV}/\sqrt{\text{Hz}})^2 + (1 \text{ nV}/\sqrt{\text{Hz}})^2} \sim 2.4 \text{ nV}/\sqrt{\text{Hz}}$ , which is consistent with the measured noise. The noise level stayed the same even we connected the DAC outputs to the analog front-end, which means that the V/I converters are the major noise sources. When multiplexing 16 TES channels, the typical TES bias resistance and the feedback

resistance are  $\sim 45 \Omega$  and  $\sim 450 \Omega$ , and the current noise therefore becomes  $\sim 222 \text{ pA}/\sqrt{\text{Hz}}$  and  $\sim 22 \text{ pA}/\sqrt{\text{Hz}}$ , respectively. The TES bias current splits to the TES shunt resistor and the TES with the split ratio of 1:10, and the effective current noise at the TES for the TES bias line becomes  $\sim 22 \text{ pA}/\sqrt{\text{Hz}}$ . These noise levels are comparable to the typical TES current noise. As the multiplexing number of channels decreases, the resistances linearly increases, and the current noises linearly decreases. For example, the current noises become  $\sim 11 \text{ pA}/\sqrt{\text{Hz}}$  when multiplexing 8 channels, which is more preferable for a better energy resolution. For multiplexing more than 16 channels, we may need to decrease the noise of the V/I converters further more.

## 4.7 Summary

In this chapter we have developed the digital FLL electronics using the off-the-shelf FPGA evaluation board and ADC/DAC board. It has the large signal bandwidth of  $> 10 \text{ MHz}$  and can multiplex up to 16 channels with satisfying the required SNR of  $> 60 \text{ dB}$ . The maximum unity-gain bandwidth in FLL is  $76.8 \text{ kHz}$  while having the sufficient phase margin of  $\sim 60^\circ$ , enabling the stable FLL. The data rate is reduced dramatically with the two-step down-sampling to realize the high-density multiplexing without deteriorating the required SNR. The required data amount for a 2-ms waveform is reduced to only 1 kB, which makes the required system data transfer rate a practical number even for thousands of signal multiplexing. We also developed the analog front-end to bridge the low-power SQUID and the digital FLL electronics. It consists of the low-noise amp and the V/I converters. The former is to amplify the SQUID output, and the latter is to convert the voltage outputs of two DACs to the TES bias current and the feedback current keeping the high output impedance. The low-noise amp has the sufficient gain of 46 dB (40 dB when  $50 \Omega$ -terminated) and the low noise characteristic of  $1.8 \text{ nV}/\sqrt{\text{Hz}}$ . The V/I converter has the wide signal bandwidth of  $20 \text{ MHz}$ , while the current noise when multiplexing 16 channels is  $22 \text{ nV}/\sqrt{\text{Hz}}$ , which may need to be reduced further.



## Chapter 5

# Experiment of TES Readout

### 5.1 Objective

As a demonstration experiment of the developed readout system, we have performed an end-to-end test using a real TES array and a X-ray source. The primary objective of this experiment is to see if the developed system is able to 1) bias the TES to its working point, 2) operate the SQUID in FLL, and 3) collect X-ray pulses. We also aimed to clarify any problems that may not be exposed in the unit test for each module

### 5.2 Setups

#### 5.2.1 Refrigerator

For a refrigerator, we used the liquid-helium-free  $^3\text{He}$ - $^4\text{He}$  dilution refrigerator developed by Taiyo Nippon Sanso Corporation (Figure 5.1), which was originally designed for the microcalorimeter spectrometer system mounted on a transmission electron microscope [36, 12, 20]. It has a unique feature that the Gifford-McMahon (GM) cycle cryocooler and the dilution refrigerator are separated to prevent the vibration of GM cryocooler from being transmitted to the cryogenic stage.

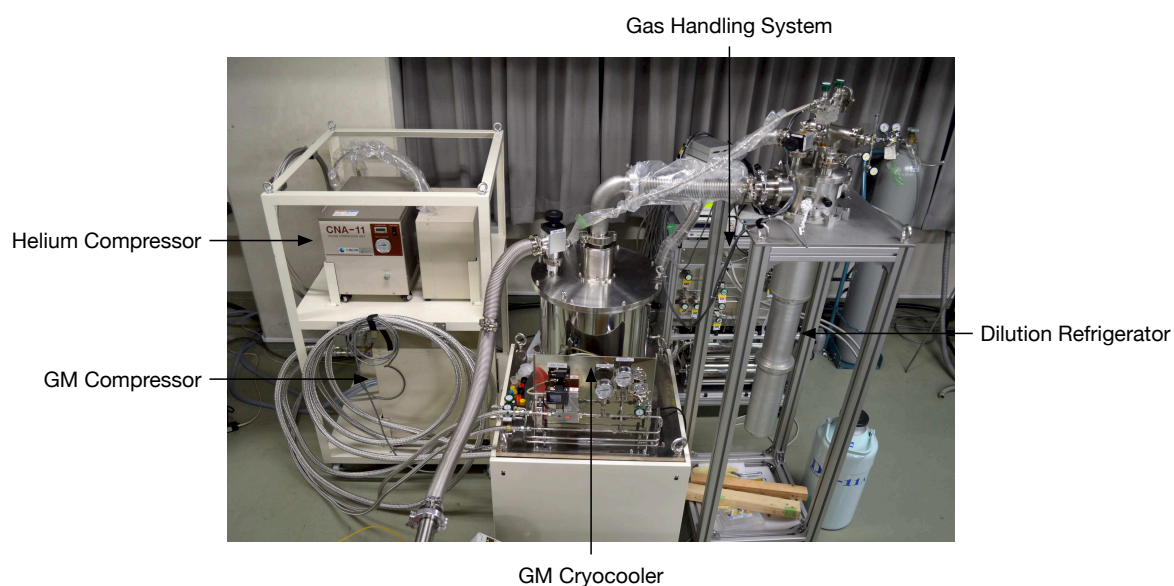


Fig. 5.1 The dry  $^3\text{He}$ - $^4\text{He}$  dilution refrigerator

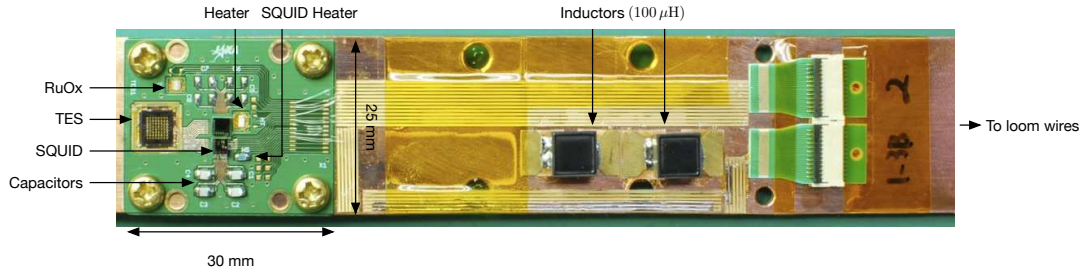


Fig. 5.2 The cryostage setup

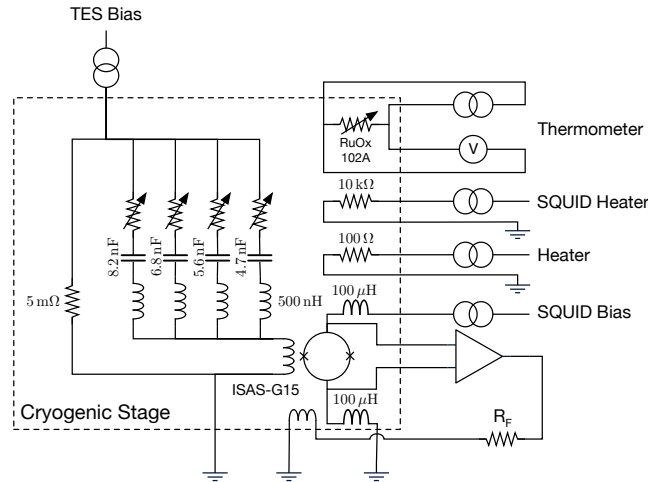


Fig. 5.3 The equivalent circuit for the cryostage setup

Table 5.1 LC filter setups

Channel	TES Address	Inductance (nH)	Capacitance (nF)	Murata Part#	Frequency (MHz)
1	83	470	8.2	GRM2195C1H822JA01D	2.5
2	73		6.8	GRM2195C1H682JA01D	2.8
3	81		5.6	GRM2195C1H562JA01D	3.1
4	72		4.7	GRM2195C1H472JA01D	3.4

## 5.2.2 Cryogenic Stage

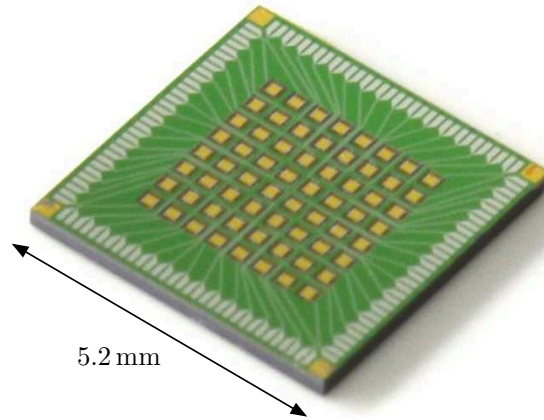
Figure 5.2 shows the cryostage setup and Figure 5.3 shows its equivalent circuit.

### TES

The TES used in this experiment is the Ti/Au-bilayer (40/90 nm)  $8 \times 8$  array developed by our research group (Figure 5.4). The chip size is  $5.2 \times 5.2$  mm. The size of each TES pixel is  $180 \times 180 \mu\text{m}$ , and the Au absorber with  $2.46 \mu\text{m}$  in thickness and  $120 \times 120 \mu\text{m}$  in size is EB-evaporated at the center.

### SQUID and LC Filter

Although we developed the 4-input low-power SQUID with built-in bandpass filters in Chapter 3, we used the 4-input ISAS-G15 SQUID with inductors, and attached capacitors externally, since the resonance frequencies

Fig. 5.4  $8 \times 8$  TES array

of the bandpass filter are higher than designed values. The capacitors are Murata's surface mount (2012/0805) multilayer ceramic capacitors with C0G dielectric. The used capacitors and the designed resonance frequencies are summarized in Table 5.1. The PCB patterns of the TES-SQUID-Capacitor loop are solder-plated for a smaller residual resistance.

#### X-Ray Source

We used a  $^{55}\text{Fe}$  X-ray radiation source. It emits Mn  $K\alpha$  and Mn  $K\beta$  X-rays. The  $K\alpha$  shows a doublet structure,  $K\alpha_1$  and  $K\alpha_2$ , with energies of 5.89875 keV and 5.88765 keV. The energy of the  $K\beta$  is 6.486 keV. The emission ratio of those lines are  $K\alpha_1 : K\alpha_2 : K\beta = 20 : 10 : 3$ .

The source is screw-mounted on top of the TES (Figure 5.5 left).

#### Mounting to the Refrigerator

We first mounted the cryostage to the coldhead of the refrigerator, then mounted the Cryoperm magnetic shielding to shield the entire cryostage from the external magnetic field (Figure 5.5). The electrical wires used in the refrigerator are Nb-Ti twisted-pair woven looms, which is relayed with constantan twisted-pair woven looms halfway through the room temperature connectors.

### 5.2.3 Room-Temperature Front-End

The developed analog front-end was directly mounted to the refrigerator port (Figure 5.6). It is sealed in an aluminum diecast enclosure as a Faraday cage. The front-end and the digital system are connected using short ( $\sim 30$  cm) coax cables. The USB cable is connected to the front-end when we adjust the SQUID to the operating point, but it is disconnected during the measurement to suppress noises from the clock of the microcontroller.

### 5.2.4 SQUID Setup

The SQUID bias current,  $I_{\text{SB}}$ , was set to  $17 \mu\text{A}$  during the measurements. Figure 5.7 shows the  $\Phi$ - $V$  curve at 200 mK and the operating point of the SQUID. The DC feedback was disabled all the time.

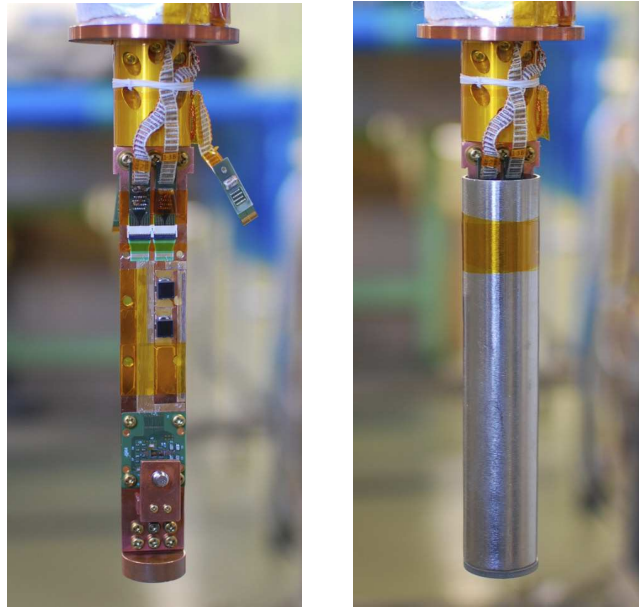


Fig. 5.5 Mounting to the refrigerator: the cryostage mounted to the coldhead of the refrigerator (left) and the cryostage covered by the Cryoperm magnetic shielding (right)

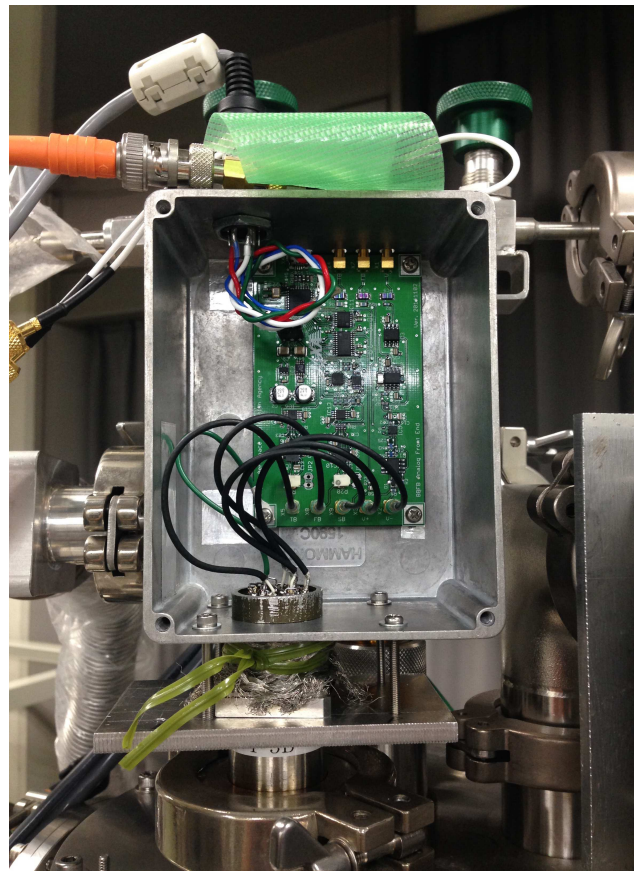


Fig. 5.6 The analog front-end directly mounted to the refrigerator port

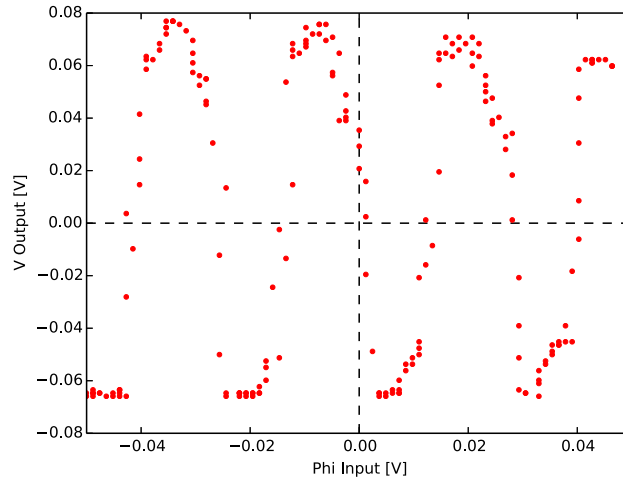


Fig. 5.7 The  $\Phi$ - $V$  curve ( $I_{SB} = 17 \mu\text{A}$ ) at 200 mK and the operating point during the measurements

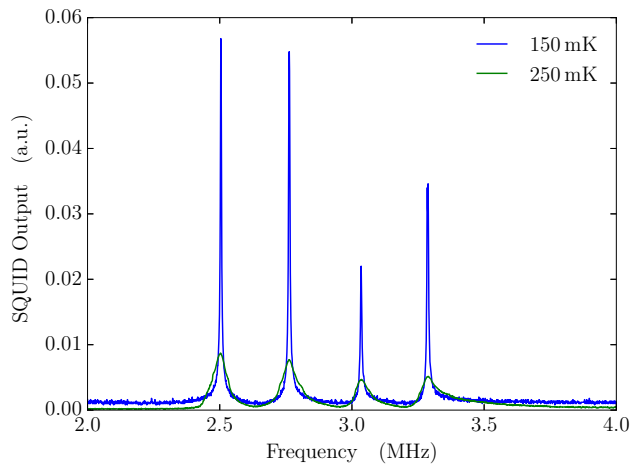


Fig. 5.8 The LC filter characteristics at 150 mK (TES super) and 250 mK (TES normal)

## 5.3 Results

### 5.3.1 LC Filter Characteristics

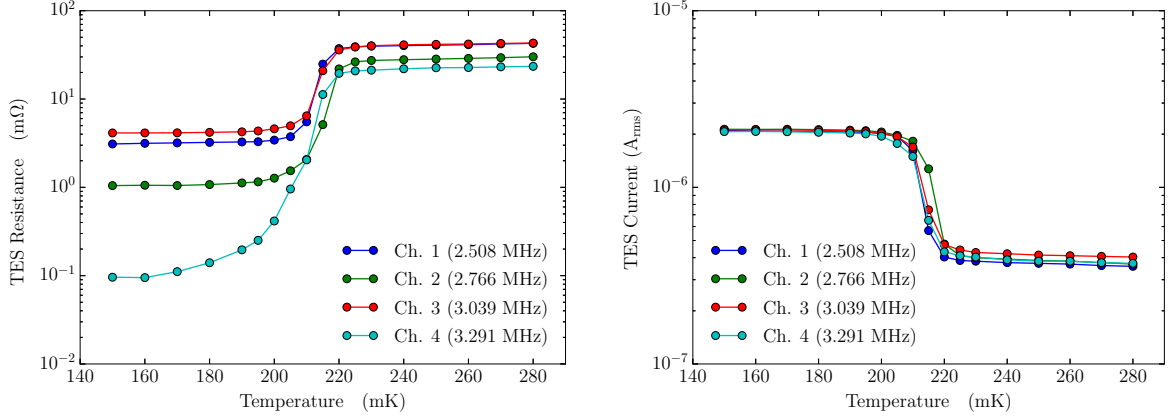
We first measured the LC filter characteristics. The SQUID was used in the open-loop, thus a TES bias current was kept low so that the SQUID output at resonance frequencies is not folded. The frequency of the TES bias current was then swept from 2.0 to 4.0 MHz in 1 kHz steps, and the SQUID output was measured.

Figure 5.8 shows the measured LC filter characteristics at 150 mK (TES super) and 250 mK (TES normal). At 150 mK, we see four resonance frequencies at 2.5, 2.8, 3.0, and 3.3 MHz.

We extracted the resonance frequencies, which the SQUID output becomes the maximum, from the characteristic at 150 mK and summarized in Table 5.2. The resonance frequencies, however, become slightly larger when in FLL due to the nulled self inductance of the SQUID input coil. The resonance frequencies, where the feedback signal becomes the maximum, in FLL are also measured, and summarized in the same table.

Table 5.2 The measured resonance frequencies of the LC filter

Channel	Resonance Frequency (open) (MHz)	Resonance Frequency (FLL) (MHz)
1	2.504	2.508
2	2.763	2.766
3	3.035	3.039
4	3.287	3.291

Fig. 5.9 The measured  $R$ - $T$  characteristics (left) and the TES current during the  $R$ - $T$  measurement (right)

### 5.3.2 $R$ - $T$ Measurements

Figure 5.9 (left) shows the measured  $R$ - $T$  characteristics of each TES channel for temperature from 150 to 280 mK in 5–10 mK steps. During the measurement, the TES bias currents for each channel were fixed to values that the TES currents at 150 mK become  $\sim 2 \mu\text{A}_{\text{rms}}$  to prevent TES from self-heating (Figure 5.9 right). When the SQUID is in FLL, the TES resistance  $R_{\text{TES}}$  is given by

$$R_{\text{TES}} = \left( \frac{I_{\text{TB}}}{I_{\text{TES}}} - 1 \right) R_{\text{S}} \quad (5.1)$$

$$= \left( \frac{V_{\text{TB}}}{V_{\text{FB}}} \frac{R_{\text{FB}}}{R_{\text{TB}}} \frac{M_{\text{in}}}{M_{\text{FB}}} - 1 \right) R_{\text{S}} \quad (5.2)$$

$$= \left( \frac{TB}{FB} \frac{R_{\text{FB}}}{R_{\text{TB}}} \frac{M_{\text{in}}}{M_{\text{FB}}} - 1 \right) R_{\text{S}}, \quad (5.3)$$

where  $I_{\text{TB}}$  is the TES bias current,  $I_{\text{TES}}$  is the TES current,  $R_{\text{S}}$  is the TES shunt resistance, which is 5 mΩ,  $V_{\text{TB}}$  is the TES bias voltage,  $V_{\text{FB}}$  is the feedback voltage,  $R_{\text{FB}}$  is the feedback resistance,  $R_{\text{TB}}$  is the TES bias resistance,  $M_{\text{in}}$  is the mutual inductance of the SQUID input coil, which is 83.26 pH,  $M_{\text{FB}}$  is the mutual inductance of the feedback coil, which is 76.62 pH,  $TB$  is the normalized TES bias value in the digital system, and  $FB$  is the normalized feedback value in the digital system. The TES resistances in Figure 5.9 (left) were calculated using the conversion equation above. The peak-to-peak TES current,  $I_{\text{TES,p-p}}$ , is given by

$$I_{\text{TES,p-p}} = \frac{FB}{R_{\text{FB}}} \frac{M_{\text{FB}}}{M_{\text{in}}} \frac{1}{N}, \quad (5.4)$$

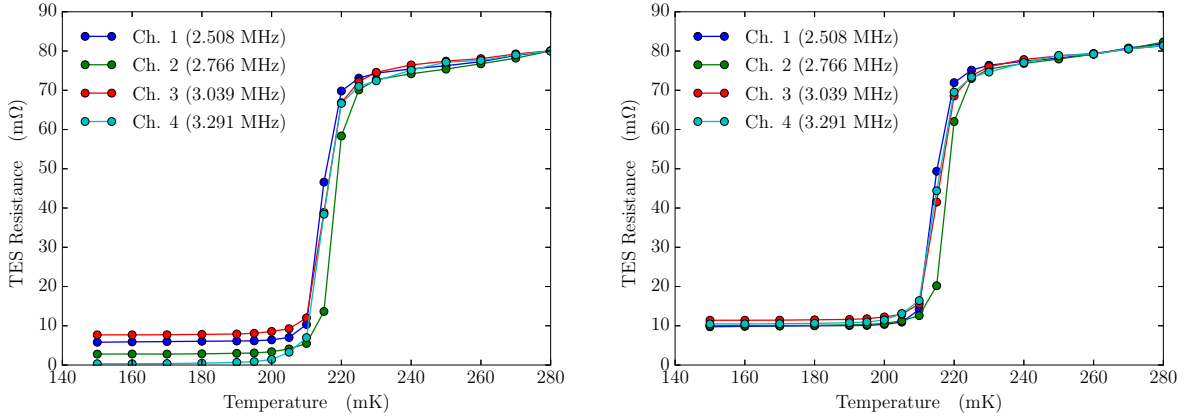


Fig. 5.10 The TES shunt resistor adjusted  $R-T$  (left) and the TES bias level adjusted  $R-T$  (right)

Table 5.3 The obtained correction factors for each channel

Channel	Frequency (MHz)	Correction Factor $\gamma$
1	2.508	1.82
2	2.766	2.49
3	3.039	1.80
4	3.291	3.04

where  $N$  is the output scaler of the digital system. In  $R-T$  measurements,  $R_{TB}$ ,  $R_{FB}$ , and  $N$  were set to  $200.1 \Omega$ ,  $1.011 \text{ k}\Omega$ , and 4, respectively.

In the  $R-T$  result, we see some inconsistencies in resistances among channels, even though the feedback currents are consistent to each other. It indicates that either (or both) the impedance of TES shunt resistor or (and) the impedance of the TES bias is (are) not frequency-independent. Some of TES pixels in this TES array have been measured in a DC setup, and they showed consistent normal resistances,  $\sim 80 \text{ m}\Omega$ . Therefore we adjusted the  $R-T$  by changing 1)  $R_S$ , the TES shunt resistance value, and 2)  $TB$ , the TES bias value, so that the averaged TES resistance over  $250 \text{ mK}$  becomes  $80 \text{ m}\Omega$ . Figure 5.10 shows the  $R-T$  that the TES shunt resistor is adjusted for each channel (left) and the TES bias level is adjusted for each channel (right). While they show good agreement in resistance, the TES bias adjusted  $R-T$  shows the better result. Therefore, we define an adjusted TES bias level,  $TB'$ , as

$$TB' = \gamma TB, \quad (5.5)$$

where  $\gamma$  is a correction factor. The correction factors for each channel in this experiment are summarized in Table 5.3, and we will use adjusted TES bias levels hereafter.

### 5.3.3 Non-multiplexing $I-V$ Measurements

We first individually measured  $I-V$  characteristics for each TES channel. An  $I-V$  characteristic is a relation between a voltage across a TES and a current through the TES under a fixed thermal bath temperature. It can be measured by obtaining the TES current, which is given by (5.4), when sweeping the TES bias current. The TES resistance is then given by (5.3). The voltage across the TES is simply a multiplication of the TES current and the TES resistance. We used the correction factor from the last section when calculating the TES current.

We measured the  $I-V$  characteristics for all channels at the bath temperatures  $150 \text{ mK}$  and  $170 \text{ mK}$ . During

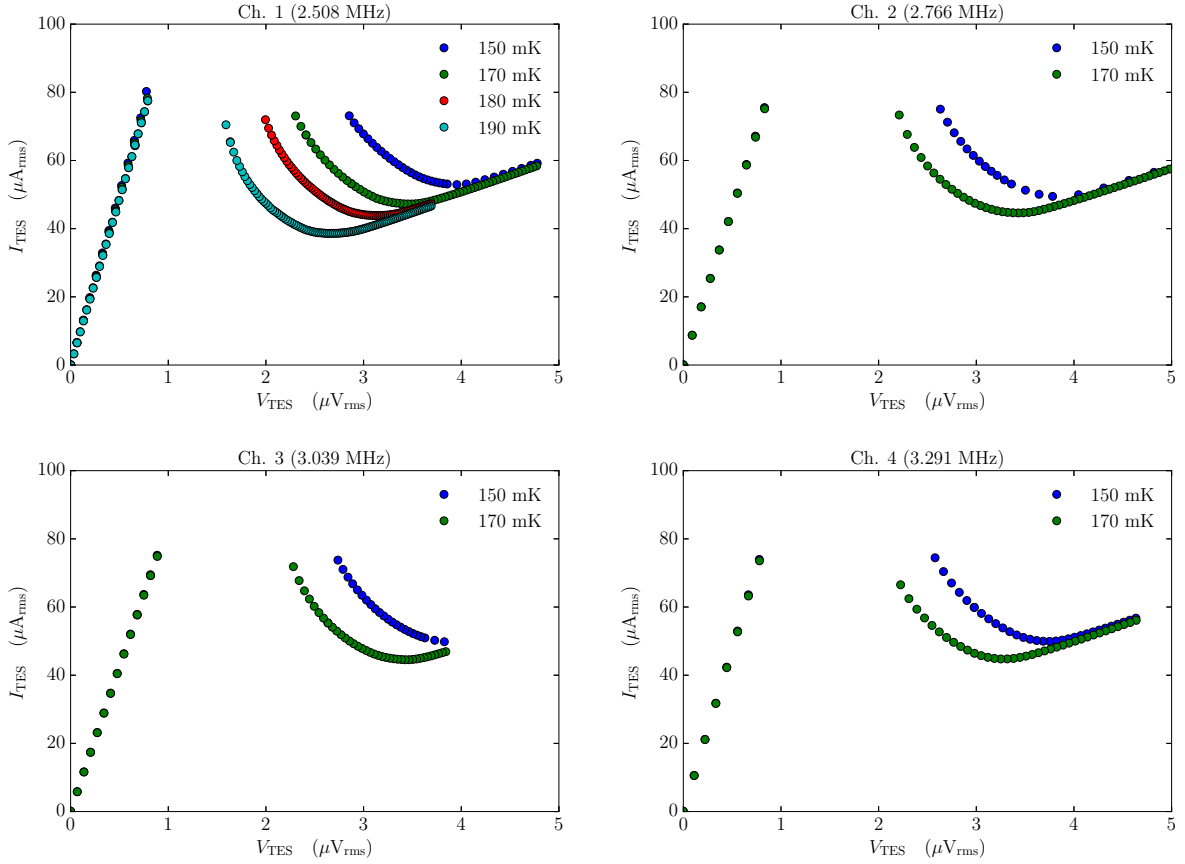


Fig. 5.11 The measured  $I$ - $V$  characteristics of each channel in non-multiplexing

the measurement, the output scaler of the digital system, the TES bias resistance, and the feedback resistance are set to 2,  $200.1\ \Omega$  and  $2.026\ \text{k}\Omega$ , respectively. For channel 1, we further measured the  $I$ - $V$  at the bath temperatures 180 mK and 190 mK. For this measurement, the output scaler of the digital system, the TES bias resistance, and the feedback resistance are set to 4,  $200.1\ \Omega$  and  $1.011\ \text{k}\Omega$ , respectively. Figure 5.11 shows the measured  $I$ - $V$  characteristics.

### 5.3.4 Non-multiplexing Pulse Collections

At first, we collected X-ray pulses in all channels at 170 mK for various TES bias currents. For each TES bias current, we collected 1,000 pulses and noises for each, and performed optimal filterings to obtain the energy resolutions at  $\text{MnK}\alpha$  (5.9 keV). We also applied templates to the noises to obtain the baseline energy resolutions. Figure 5.12 shows the averaged pulses for 2-ms length 1,000 pulses for each TES bias current. The results of optimal filterings are summarized in Table 5.4.

Since the channel 1 showed the better energy resolution, we also collected pulses and noises at the bath temperatures 180 mK and 190 mK. Figure 5.13 shows the averaged pulses for the pulses collected at 180 mK and 190 mK. The results of the optimal filterings are also summarized in Table 5.4. The best energy resolution we have obtained is 37.7 eV FWHM @ 5.9 keV (19.6 eV FWHM baseline) in the channel 1 when the bath temperature is 180 mK and the TES bias current is  $510\ \mu\text{A}_{\text{rms}}$ . Figure 5.14 shows the detailed results of the optimal filtering for the best energy resolution. For the conversion from the pulse height (PHA) to the energy, we used a quadratic

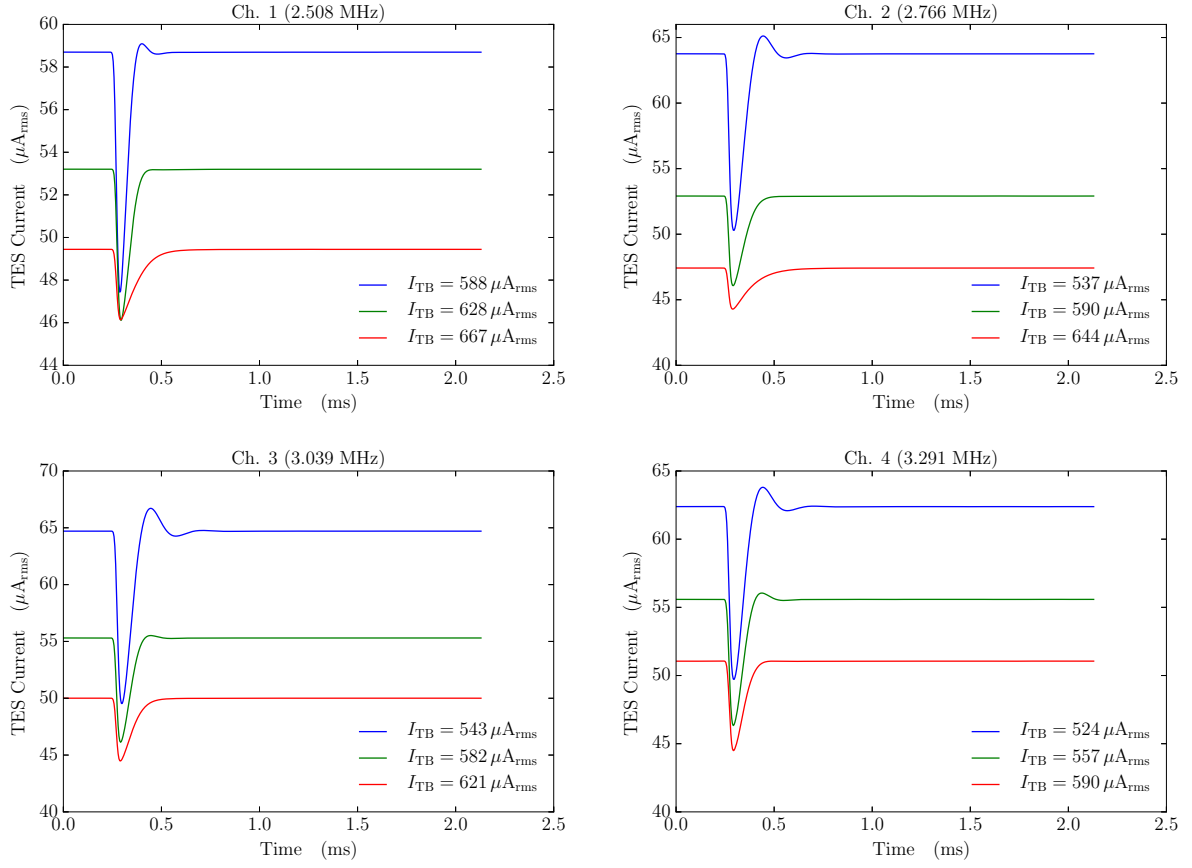


Fig. 5.12 The averaged pulses in each channel at 150 mK for various TES bias currents

Table 5.4 The obtained energy resolutions in non-multiplexing pulse collections

Channel	$T_{\text{bath}}$ (mK)	TES Bias ( $\mu\text{A}_{\text{rms}}$ )	SNR (dB)	Energy Resolution	
				Baseline (eV FWHM)	@ 5.9 keV (eV FWHM)
1	170	588	55.9	22.1	$34.2 \pm 1.3$
		628	54.0	28.2	$47.7 \pm 1.7$
		667	49.9	43.7	$69.7 \pm 2.3$
	180	490	56.1	20.8	$52.2 \pm 2.0$
		510	56.2	19.6	$37.7 \pm 1.4$
		529	56.0	21.4	$41.3 \pm 1.5$
2	170	402	52.9	25.0	$103.8 \pm 3.3$
		537	49.0	35.8	$62.1 \pm 2.7$
		590	45.6	49.3	$70.1 \pm 2.4$
3	170	644	41.5	80.2	$100.8 \pm 3.1$
		543	53.1	30.6	$46.7 \pm 1.7$
		582	51.9	34.4	$51.4 \pm 1.8$
4	170	621	49.3	47.9	$60.6 \pm 2.0$
		524	47.3	49.5	$60.5 \pm 1.9$
		557	45.4	61.5	$82.4 \pm 2.4$
		590	43.5	74.6	$109.1 \pm 3.7$

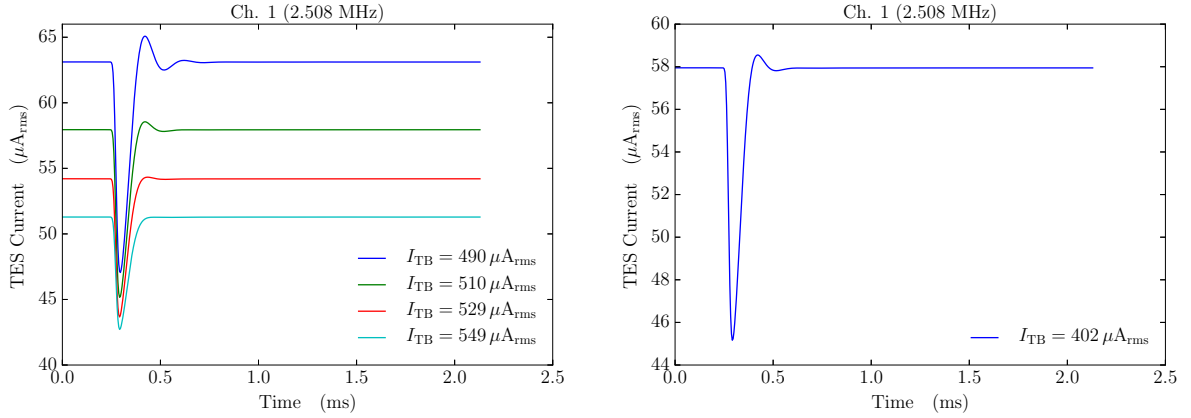


Fig. 5.13 The averaged pulses in channel 1 at 180 mK (left) and 190 mK (right) for various TES bias currents

Table 5.5 The obtained energy resolutions in multiplexing pulse collections for all the channels

Channel	$T_{\text{bath}}$ (mK)	TES Bias ( $\mu\text{A}_{\text{rms}}$ )	SNR (dB)	Energy Resolution	
				Baseline (eV FWHM)	@ 5.9 keV (eV FWHM)
1	170	608	53.4	28.9	$112 \pm 4$
2		641	45.7	75.0	$97 \pm 3$
3		628	47.1	61.3	$87 \pm 3$
4		603	45.4	78.4	$118 \pm 4$

function

$$PHA = aE^2 + bE, \quad (5.6)$$

fitting to the origin, the  $\text{MnK}\alpha$  line and the  $\text{MnK}\beta$  line, and obtained the energy  $E$  as

$$E(PHA) = \frac{-b + \sqrt{b^2 - 4aPHA}}{2a}. \quad (5.7)$$

However, for the baseline energy resolution, we just used a linear function fitting to only the origin and the  $\text{MnK}\alpha$  line since the energy calibration using the quadratic function often underestimates the baseline energy resolution. The obtained noise ( $\sim 250 \text{ pA}/\sqrt{\text{Hz}}$ ) is much larger than the expected noise level ( $\sim 30 \text{ pA}/\sqrt{\text{Hz}}$ ), and we consider that it is the reason for the poor energy resolution. It is further discussed in Section 6.2.

### 5.3.5 Simultaneous $I$ - $V$ Measurements

We also succeeded to measure  $I$ - $V$  simultaneously multiplexing all channels at 170 mK. During the measurement, the output scaler of the digital system, the TES bias resistance, and the feedback resistance are set to 4, 200.1  $\Omega$  and 1.011 k $\Omega$ , respectively. Figure 5.15 shows the measured  $I$ - $V$ .

### 5.3.6 Simultaneous Pulse Collections

We then simultaneously collected pulses in all channels at 170 mK. The output scaler, the TES bias resistance, and the feedback resistance were kept the same from the  $I$ - $V$  measurement. We collected 4-ms 1,000 pulses and noises for each channel, and applied optimal filterings to obtain the energy resolutions. Figure 5.16 shows the averaged pulses for 4-ms length 1,000 pulses. Table 5.5 summarizes the obtained energy resolutions. Figure 5.17

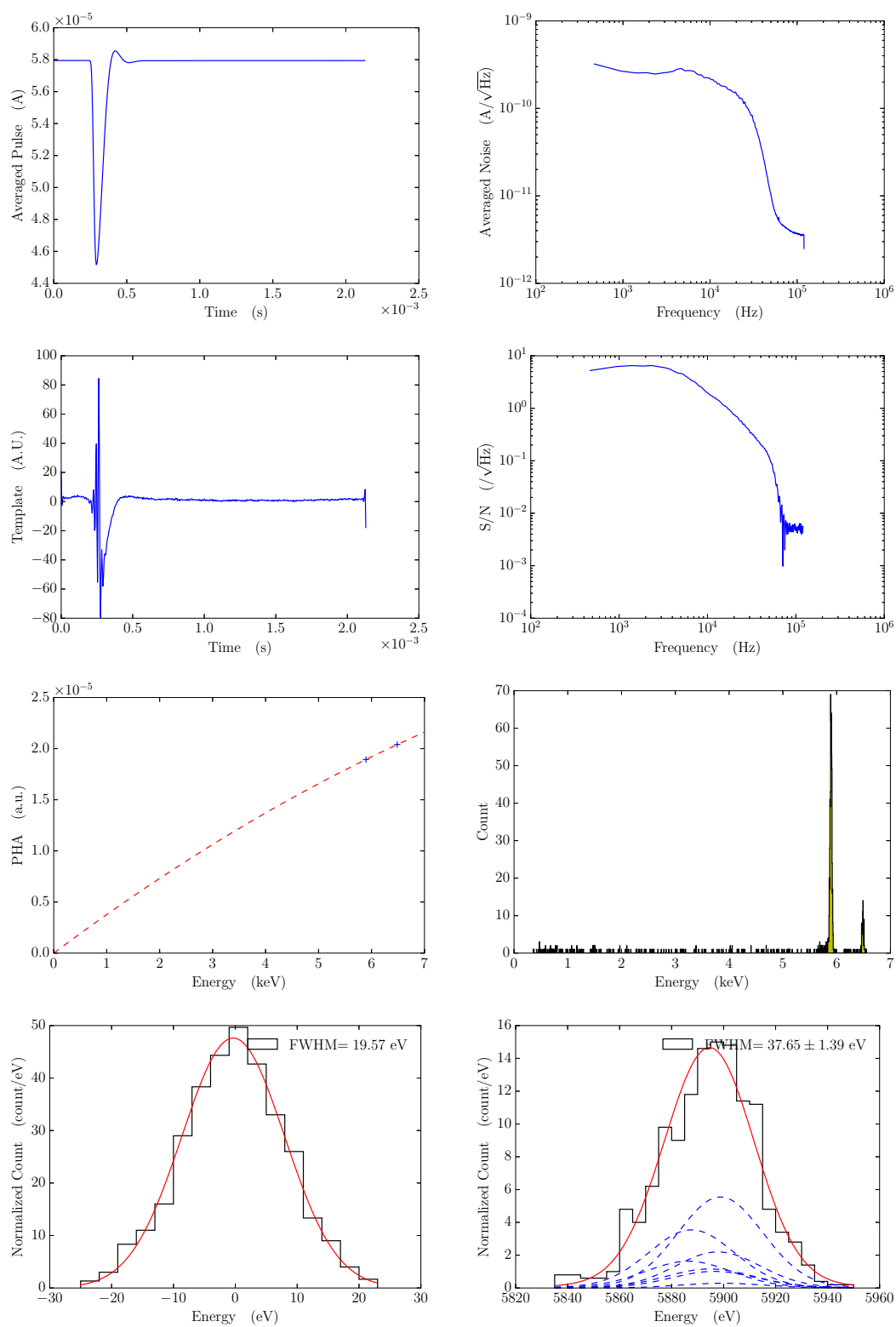


Fig. 5.14 The pulse collection result in channel 1 at 180 mK: the averaged pulse (top left), the averaged noise (top right), the template (2nd top left), the signal-to-noise ratio (2nd top right), the energy calibration curve (2nd bottom left), the energy spectrum (2nd bottom right), the baseline energy resolution (bottom left), and the energy resolution at  $\text{MnK}\alpha$  (5.9 keV).

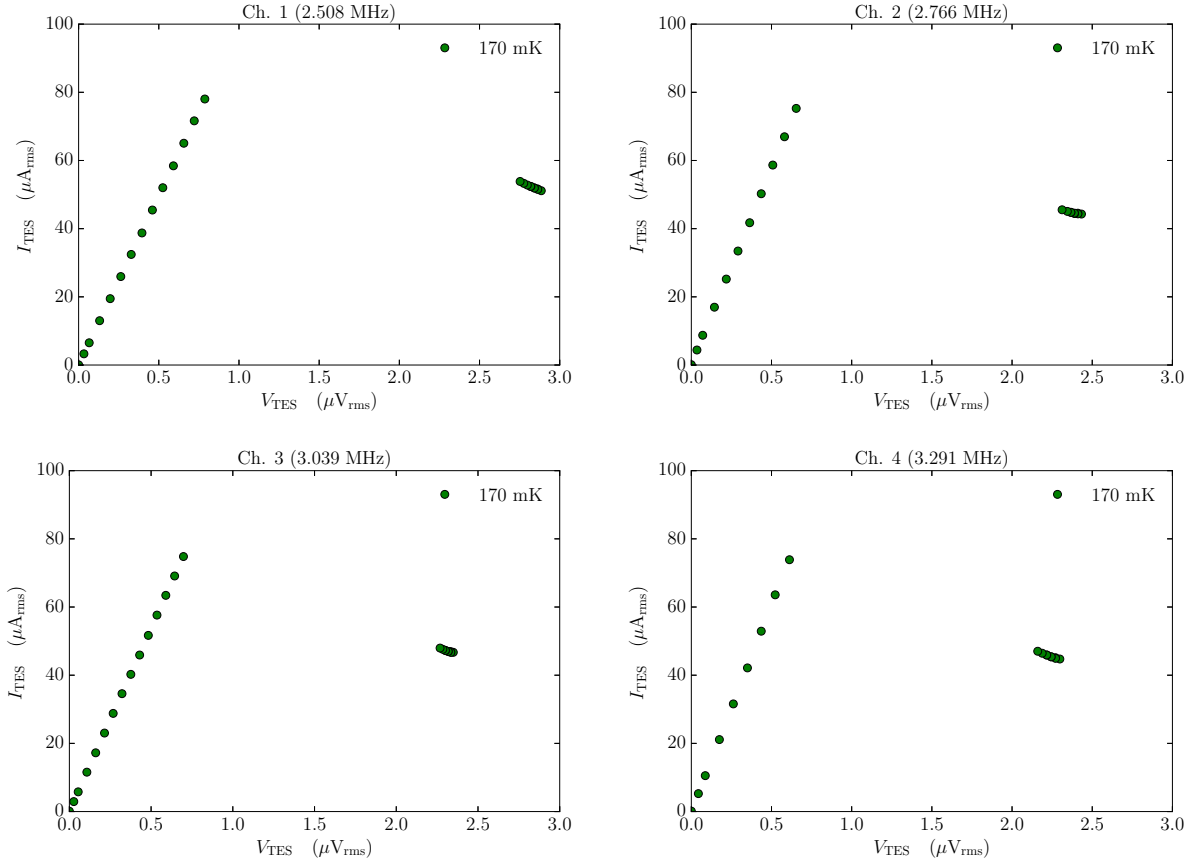


Fig. 5.15 The simultaneously measured  $I$ - $V$  characteristics multiplexing all channels

shows the results of the optimal filtering for the channel 1. While the energy resolutions are all  $\sim 100$  eV FWHM @ 5.9 keV, we succeeded in the 4-channel simultaneous pulse collection in FDM from the single-staged cryogenic setup for the first time. During the collection, we have observed electrical crosstalks (the lines noises seen in the averaged noise in Figure 5.17), which is discussed in Section 6.3, and we consider it the reason why the obtained energy resolutions are much larger than the baseline energy resolutions.

## 5.4 Summary

In this experiment we have tested the developed readout system if it is able to bias the TES to its working point, operate the SQUID in FLL, and collect X-ray pulses. The system successfully passed these tests, and proved its practical use. Meanwhile, the following new issues have been identified: the excess noise and the crosstalk. In the next Chapter, we discuss these issues in details.

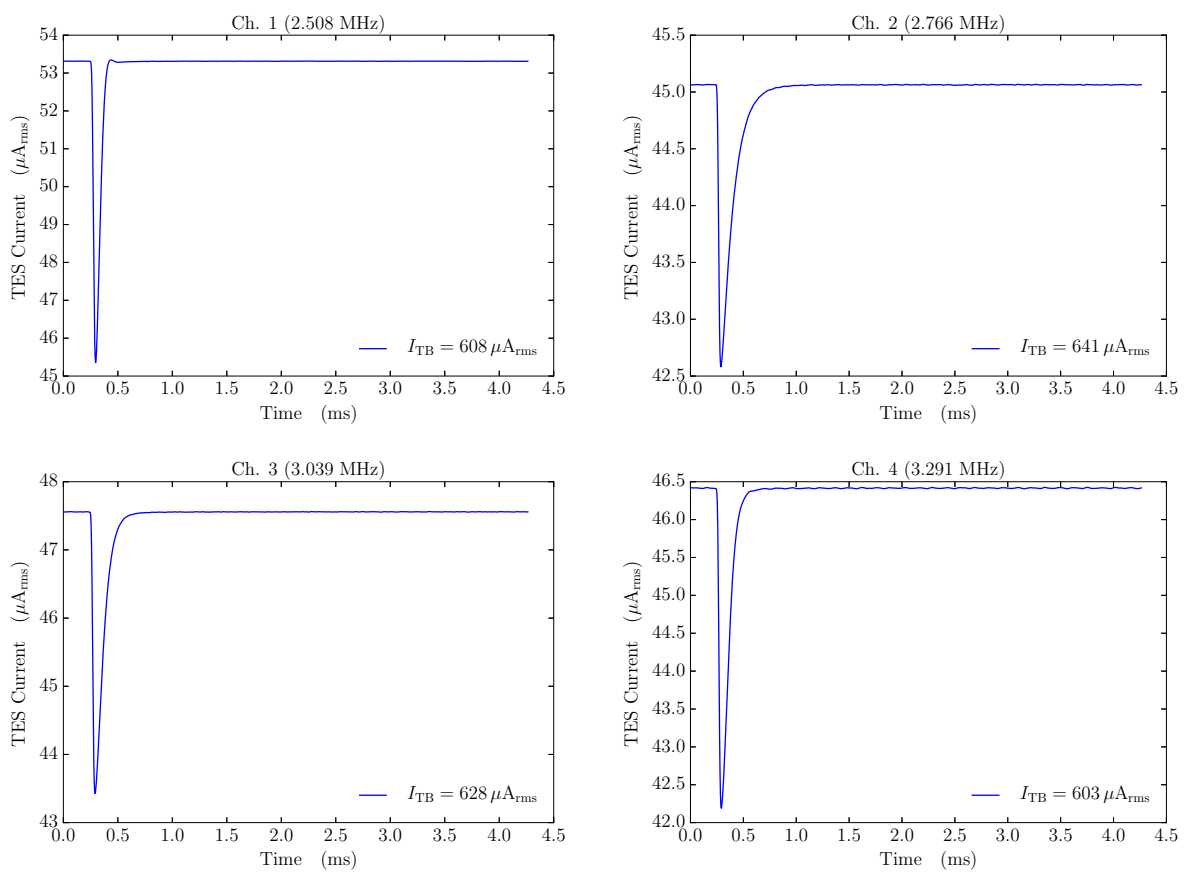


Fig. 5.16 The averaged pulses in each channel at 170 mK for various TES bias currents

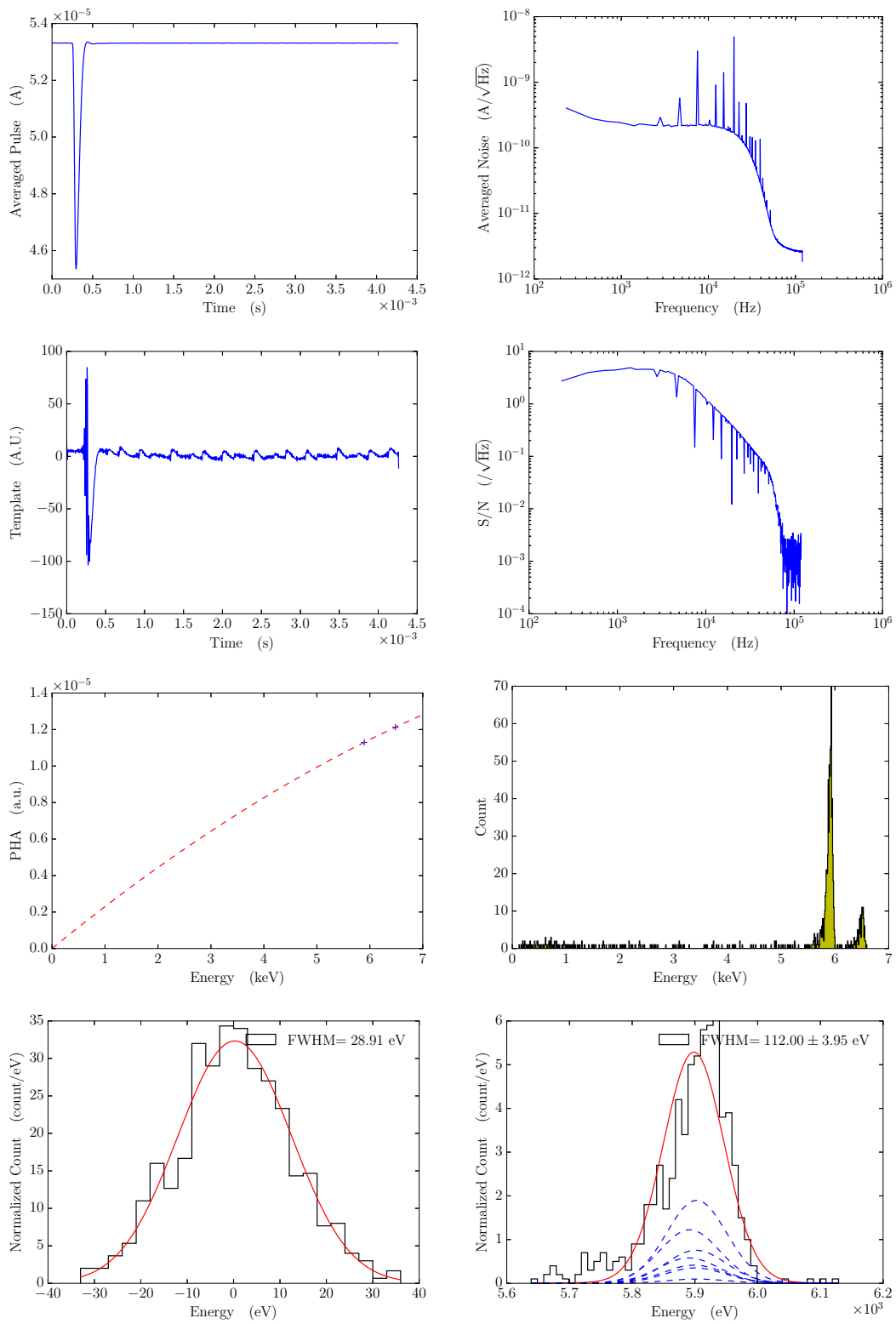


Fig. 5.17 The 4-channel simultaneous pulse collection result in channel 1 at 170 mK: the averaged pulse (top left), the averaged noise (top right), the template (2nd top left), the signal-to-noise ratio (2nd top right), the energy calibration curve (2nd bottom left), the energy spectrum (2nd bottom right), the baseline energy resolution (bottom left), and the energy resolution at  $\text{MnK}\alpha$  (5.9 keV).

## Chapter 6

# Discussion

### 6.1 Energy Resolution Degradation due to Readout System

We here systematically determine the contribution of the developed readout system to the obtained energy resolution. The best baseline energy resolution we obtained in the experiment was  $\sim 20$  eV (@5.9 keV), which is linearly determined by the signal level and noise level. We can therefore estimate the contribution by summing up the noises from the readout system and comparing it to the obtained noise.

Figure 6.1 shows the simplified schematic diagram of the FDM TES readout. The major noise sources of the

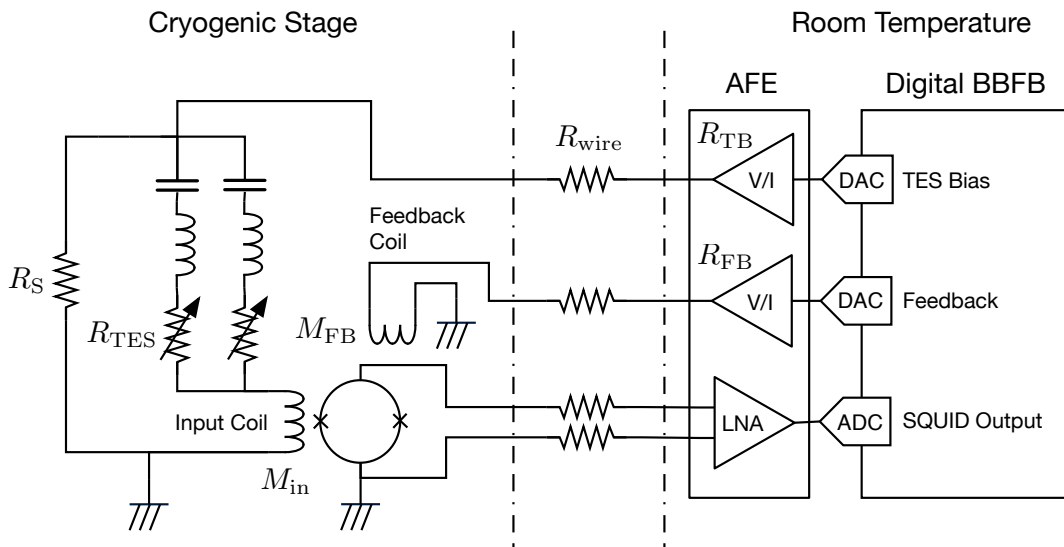


Fig. 6.1 A typical experimental setup for a FDM TES readout

Table 6.1 A readout system noise estimation

Noise Source	Voltage Noise (nV/ $\sqrt{\text{Hz}}$ )	Voltage-to-Current Conversion Factor	Current Noise <sup>†</sup> (pA/ $\sqrt{\text{Hz}}$ )
TES Bias	10	$R_S/R_{TB}(R_S + R_{TES})$	5
Feedback	10	$M_{FB}/M_{in}R_{FB}$	9
SQUID Output	2	$Z_{\text{tran}}$	20
Total	–	–	22

<sup>†</sup> Assumed  $R_S/(R_S + R_{TES}) = 0.1$ ,  $R_{TB} = 200 \Omega$ ,  $R_{FB} = 1 \text{ k}\Omega$ , and  $Z_{\text{tran}} = 100 \text{ V/A}$ .

readout system are the SQUID itself, the low-noise amplifier (LNA), two voltage-to-current (V/I) converters, and two DACs. Let us group them into three: the TES bias line (DAC + V/I with  $R_{\text{TB}}$ ), the feedback line (DAC + V/I with  $R_{\text{FB}}$ ), and the SQUID output line (SQUID + LNA). The voltage noises at the boundary between room temperature and the cryogenic stage for the TES bias line and the feedback line are almost independent to the bias resistors ( $R_{\text{TB}}$  and  $R_{\text{FB}}$ ) and thus nearly identical, which are measured in Section 4.6.3. The current noises at the boundary are then calculated as the voltage noise divided by the bias resistances. Those current noises are then converted to the current noises at the SQUID input. For the TES bias line, it is reduced by  $R_S/(R_S + R_{\text{TES}})$ , where  $R_S$  is the shunt resistance and  $R_{\text{TES}}$  is the TES resistance at the operating point, because of the current divider due to the shunt resistor and the TES. For the feedback line, it is scaled by  $M_{\text{FB}}/M_{\text{in}}$ , where  $M_{\text{FB}}$  is the mutual inductance of the feedback coil and  $M_{\text{in}}$  is the mutual inductance of the input coil, for the conversion. The current noise at the SQUID input for the SQUID output line can be given by the SQUID output voltage noise + the LNA equivalent input voltage noise divided by the SQUID transimpedance gain  $Z_{\text{tran}}$ . The SQUID output voltage noise is typically far smaller than the LNA equivalent input voltage noise, which is also measured in Section 4.6.3, and the LNA noise therefore dominates the current noise. Table 6.1 summarizes the voltage noises as well as the converted current noises for the experiment. The current noise for the TES bias line,  $I_{\text{N,TB}}$ , is given by

$$I_{\text{N,TB}} \sim 5 \left( \frac{V_{\text{N,TB}}}{10 \text{ nV}/\sqrt{\text{Hz}}} \right) \left( \frac{R_{\text{TB}}}{200 \Omega} \right)^{-1} \left( \frac{R_S/(R_S + R_{\text{TES}})}{0.1} \right) \quad [\text{pA}/\sqrt{\text{Hz}}], \quad (6.1)$$

where  $V_{\text{N,TB}}$  is the voltage noise for the TES bias line. For  $R_S/(R_S + R_{\text{TES}})$  we assumed 0.1, as  $R_S$  and  $R_{\text{TES}}$  are  $5 \text{ m}\Omega$  and  $\sim 45 \text{ m}\Omega$ , respectively. The current noise for the feedback line,  $I_{\text{N,FB}}$ , is given by

$$I_{\text{N,FB}} \sim 9 \left( \frac{V_{\text{N,FB}}}{10 \text{ nV}/\sqrt{\text{Hz}}} \right) \left( \frac{M_{\text{FB}}}{76.62 \text{ pH}} \right) \left( \frac{M_{\text{in}}}{83.37 \text{ pH}} \right)^{-1} \left( \frac{R_{\text{FB}}}{1 \text{ k}\Omega} \right)^{-1} \quad [\text{pA}/\sqrt{\text{Hz}}], \quad (6.2)$$

where  $V_{\text{N,FB}}$  is the voltage noise for the feedback line. The current noise for the SQUID output line,  $I_{\text{N,SQ}}$ , is given by

$$I_{\text{N,SQ}} \sim 20 \left( \frac{V_{\text{N,SQ}}}{2 \text{ nV}/\sqrt{\text{Hz}}} \right) \left( \frac{Z_{\text{tran}}}{100 \text{ V/A}} \right)^{-1} \quad [\text{pA}/\sqrt{\text{Hz}}], \quad (6.3)$$

where  $V_{\text{N,SQ}}$  is the voltage noise for the SQUID output line. The total current noise at the SQUID input due to the readout system,  $I_{\text{N,RS}}$ , is finally given by

$$I_{\text{N,RS}} = \sqrt{I_{\text{N,TB}}^2 + I_{\text{N,FB}}^2 + I_{\text{N,SQ}}^2} \sim 22 \text{ pA}/\sqrt{\text{Hz}}.$$

The current noise when we obtained the best baseline energy resolution was  $I_{\text{N}} \sim 250 \text{ pA}/\sqrt{\text{Hz}}$ , while the baseline energy resolution was  $\Delta E \sim 20 \text{ eV}$ , which makes the contribution of the readout system to the resolution,  $\Delta E_{\text{RS}}$ , as

$$\Delta E_{\text{RS}} = \Delta E \left( \frac{I_{\text{N,RS}}}{I_{\text{N}}} \right) \quad (6.4)$$

$$\sim 1.8 \left( \frac{\Delta E}{20 \text{ eV}} \right) \left( \frac{I_{\text{N,RS}}}{22 \text{ pA}/\sqrt{\text{Hz}}} \right) \left( \frac{I_{\text{N}}}{250 \text{ pA}/\sqrt{\text{Hz}}} \right)^{-1} \quad [\text{eV}]. \quad (6.5)$$

The total current noise due to the readout system and the contribution to the energy resolution are depend on the bias resistances,  $R_{\text{TB}}$  and  $R_{\text{FB}}$ , or the number of multiplexing channels. Figure 6.2 shows the total current noise along with the each components and the energy resolution contribution for various number of multiplexing channels. In the figure we assumed that the bias resistances are linearly scaled by the inverse of the number of

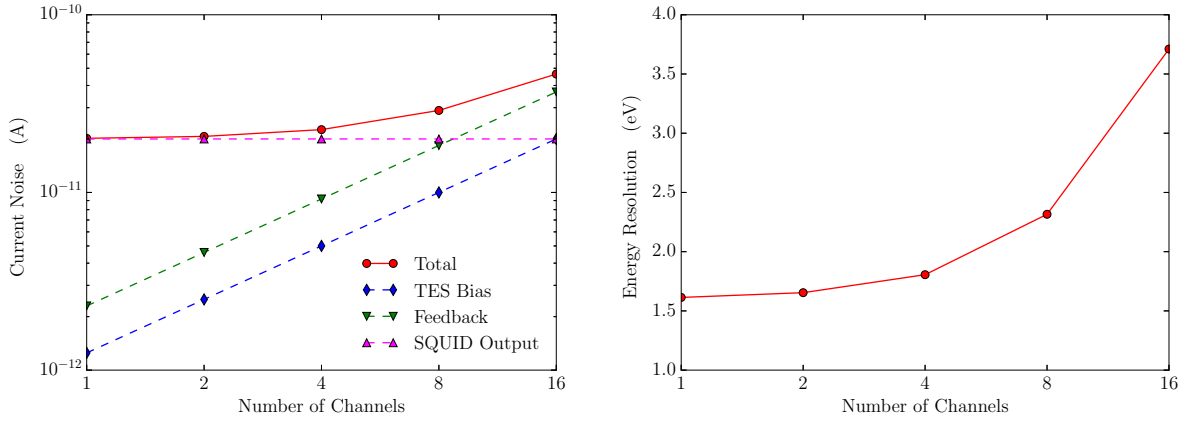


Fig. 6.2 The current noise due to the readout system (left) and the contribution to the energy resolution (right) for various number of multiplexing channels

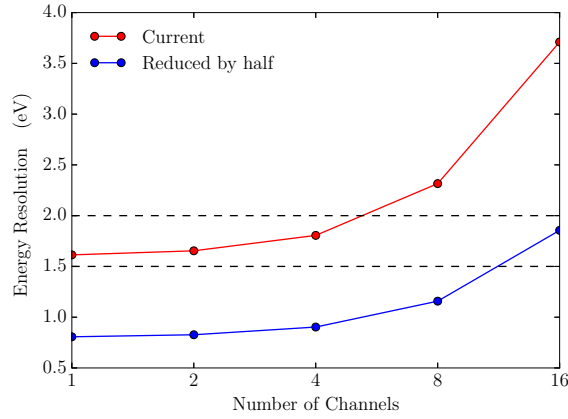


Fig. 6.3 The contribution of the readout system to the energy resolution when the system noise is reduced by half

channels.

The requirement to the energy resolution for DIOS is 2 eV FWHM @ 2 keV, which is equivalent to 5.9 eV FWHM @ 5.9 keV, and the calculated contribution is small enough even for 16-channel multiplexing assuming the TES energy resolution to be 4 eV FWHM @ 5.9 keV. The developed readout system is thus ready already for DIOS.

On the other hand, the requirement to the energy resolution for ATHENA is 2.5 eV FWHM @ 5.9 keV. Even if we have a TES with its energy resolution as good as 2.0 eV FWHM @ 5.9 keV, the allowed contribution from the readout system is < 1.5 eV FWHM @ 5.9 keV, which is too small for the developed readout system. To achieve the required energy resolution in 40-channel multiplexing, we need to make noises smaller and signal power larger. In the developed system, the LNA equivalent input voltage noise is  $\sim 2 \text{ nV}/\sqrt{\text{Hz}}$  and it dominates when the number of multiplexing channels is less than 8. It is possible to lower it by nearly half,  $\sim 1 \text{ nV}/\sqrt{\text{Hz}}$ , with comparative ease. When the number of channels exceeds more than 8, the noise from the feedback and TES bias lines starts dominating. The voltage noise at those lines are currently  $\sim 10 \text{ nV}/\sqrt{\text{Hz}}$ , which is mostly caused by the voltage-to-current converter. It may be also possible to lower it by half,  $\sim 5 \text{ nV}/\sqrt{\text{Hz}}$ . Figure 6.3 shows the contribution to the energy resolution when the readout system noise is reduced by half. The dashed line at 1.5 eV shows the upper limit for the requirement assuming the TES energy resolution to be 2.0 eV FWHM @ 5.9 keV,

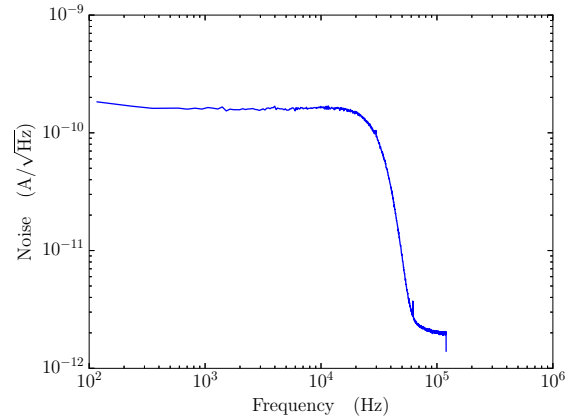


Fig. 6.4 The current noise when the TES is in the normal state at 240 mK

and the dashed line at 2.0 eV shows the upper limit assuming the TES energy resolution to be 1.5 eV FWHM @ 5.9 keV. For the latter case, the developed readout system satisfies the requirement to the energy resolution when the number of multiplexing channels is less than or equal to 16. The requirement to the multiplexing channel is, however, 40 for ATHENA, and to satisfy both the energy resolution and the multiplexing channel, we may need to lower the readout system noise further more as well as to increase the signal power.

## 6.2 Excess Noise

The current noise level (Figure 5.14) when we obtained the best energy resolution was  $\sim 250 \text{ pA}/\sqrt{\text{Hz}}$ , which is considerably high. The noise at the TES working point can be decomposed to the TES phonon noise, the TES Johnson noise, and the readout system noise. However, the observed noise can not generally be explained only by those components, and we typically call the unknown component as an excess noise. Figure 6.4 shows the current noise when the TES is in the normal state at 240 mK. When TES is in the normal state, the phonon noise becomes negligible, and the observed noise consists of the TES Johnson noise, the readout system noise, and the excess noise. The TES resistance at the normal state is  $\sim 80 \text{ m}\Omega$  according to the  $R$ - $T$  characteristics, and the current noise is therefore  $\sim 13 \text{ pA}/\sqrt{\text{Hz}}$ . The readout system noise is  $\sim 22 \text{ pA}/\sqrt{\text{Hz}}$  from the last section, which makes the total noise except the excess noise to be  $\sim 25 \text{ pA}/\sqrt{\text{Hz}}$ . The current noise level in Figure 6.4 is  $\sim 160 \text{ pA}/\sqrt{\text{Hz}}$ , and the calculated excess noise is therefore  $\sim 158 \text{ pA}/\sqrt{\text{Hz}}$ . The root cause of the excess noise is still unknown and is under investigation.

## 6.3 Crosstalks

Figure 6.5 shows the observed current noises for the channel that we obtained the best energy resolution for various TES states. The blue line in the plot is the current noise when the TES is in the normal state, which is identical to the noise spectrum in the last section. The green line in the plot is when the TES is in the working point for the non-multiplexing pulse collection. When the TES is in the working point, the phonon noise is also added to the total noise. The phonon noise level at the working point ( $T_{\text{bath}} = 180 \text{ mK}$ ,  $R_{\text{TES}} \sim 45 \text{ m}\Omega$ ) is  $\sim 30 \text{ pA}/\sqrt{\text{Hz}}$ , which is obtained from a DC measurement, and the total current noise should be therefore  $\sim 163 \text{ pA}/\sqrt{\text{Hz}}$ , which is however far smaller than the observed noise level,  $\sim 250 \text{ pA}/\sqrt{\text{Hz}}$ . The excess is therefore  $\sim 190 \text{ pA}/\sqrt{\text{Hz}}$ . The red line in the plot is when the TES is in the working point for the 4-channel simultaneous pulse collection. The baseline level is almost identical to the noise when the non-multiplexing collection, but it exhibits several line

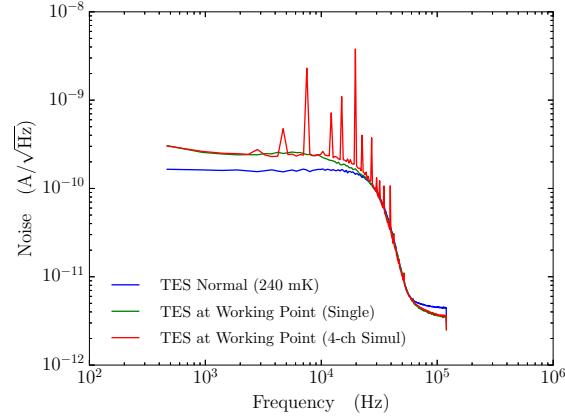


Fig. 6.5 The current noises for various TES states

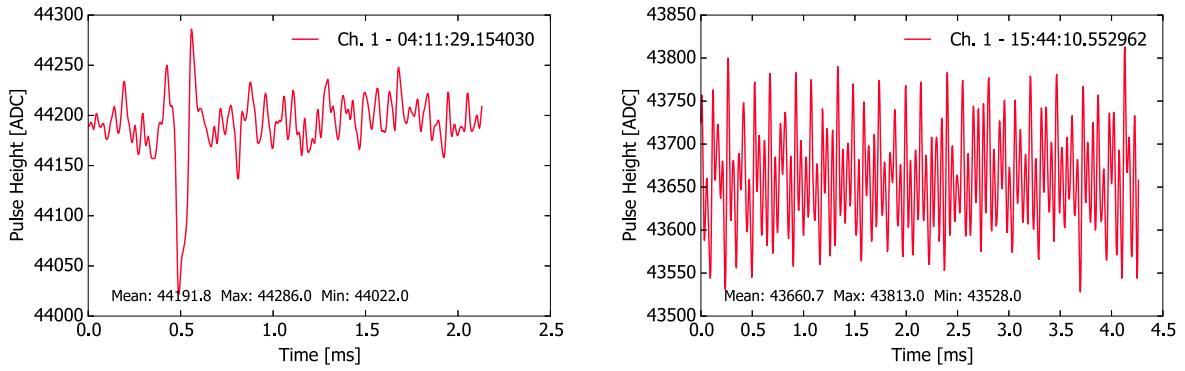


Fig. 6.6 The observed crosstalks: the possible thermal crosstalk in the non-multiplexing pulse collection (left) and the electrical crosstalk in the 4-channel simultaneous pulse collection (right)

noises.

The excess noise and the line noises when the TES is in the working point are possibly caused by crosstalks. Figure 6.6 shows the observed crosstalks. The left plot shows a possible thermal crosstalk seen in the noise waveform in the non-multiplexing pulse collection. As the shape resembles in a X-ray pulse, it may be a thermal input to the TES pixel from other TES pixels or wirings. The power spectrum of a thermal crosstalk shows an identical frequency response to a X-ray pulse, as it is an input to the TES. The noise spectrum when the TES is in the working point shows a pole at  $\sim 5$  kHz, which can be also seen in the averaged pulse power spectrum, while the noise spectrum when the TES is in normal shows the flat spectrum. It indicates that the excess noise is due to the thermal input. The thermal crosstalk occurs within the TES, and it is therefore beyond the scope of this thesis, but it can be typically avoided by having a collimeter on top of the TES and a non-superconducting conductive layer (such as AU) at the back side of the TES for a better thermal conductance. The right plot in Figure 6.6 shows an electrical crosstalk seen in the noise waveform in the 4-channel simultaneous pulse collection. It exhibits several periodic waveforms and these are the line noises seen in the noise spectrum. As it can be seen only when multiplexing and the waveforms are periodic, we consider that it is carriers of other channels appeared as the crosstalk. As it could not be seen in the crosstalk evaluation in the loopback test (Section 4.5.3), we consider that the root cause exists in the cryogenic stage, or the wirings between room temperature and the cryogenic stage.

## 6.4 Summary

In this chapter we discussed the contribution of the developed readout system to the energy resolution as well as the two new issues arisen in the TES readout experiment. The primary source of degradation of the energy resolution is the excess noise and crosstalks, which dominates more than 90% of the measured noise. The contribution of the readout system to the energy resolution during the experiment was  $\sim 1.8$  eV FWHM @ 5.9 keV for 4-channel multiplexing, and the calculated contribution when 16-channel multiplexing is  $\sim 3.6$  eV FWHM @ 5.9 keV. Suppose the excess noise and the crosstalks are successfully suppressed and we use a TES array that intrinsic energy resolution is 2.0 eV FWHM @ 5.9 keV, the final energy resolution that we can obtain using the developed readout system become  $\sim 2.7$  eV FWHM @ 5.9 keV and  $\sim 4.1$  eV FWHM @ 5.9 keV for 4-channel multiplexing and 16-channel multiplexing, respectively. These are equivalent to  $\sim 0.9$  eV FWHM @ 2 keV and  $\sim 1.4$  eV FWHM @ 2 keV, which already satisfy the DIOS requirement. Those are, however, still too large for the ATHENA requirement, and the noises at the analog front-end need to be reduced at least by half to satisfy the requirement.

## Chapter 7

# Summary

### 7.1 Summary

In this thesis, we have freshly developed the entire FDM readout system for large-format TES microcalorimeter arrays toward the future space missions. The developed system consists of the low-power multi-input SQUID with built-in bandpass filters, the high-frequency digital FLL electronics, and the analog front-end optimized for bridging the low-power SQUID and the digital electronics. The cold electronics are optimized for the simple single-staged configuration, and the warm electronics are optimized for the high-density signal multiplexing to support the simple cryogenic setup.

The unique feature of the developed SQUID is its very low heat dissipation,  $\sim 20$  nW, while having the sufficient gain,  $> 100$  V/A. It also has the very low noise characteristic,  $< 10$  pA/ $\sqrt{\text{Hz}}$  @ 4K. With these features, the SQUID can suffice to be the only amplifier in the cold electronics even though it can be placed at the cryogenic stage below 100 mK. Using the developed low-power SQUID, we also developed the multi-input SQUID chip with built-in bandpass filters. Within the size of  $2.5 \times 2.5$  mm, it carries the low-power SQUID, the TES shunt resistor, and the LC bandpass filters for four channels. We also developed the same-size extension chip that consists of the bandpass filters for four other channels, and it can be attached to the multi-input SQUID chip with only two bonding wires. With these chips, the cryogenic stage setup is dramatically simplified, and the feasibility of the large-format TES array is demonstrated.

The digital FLL electronics consists of the fast FPGA and the fast ADC/DAC module. It has the large signal bandwidth,  $> 10$  MHz, and can multiplex up to 16 channels without deteriorating the required SNR,  $> 60$  dB. The maximum unity-gain bandwidth in FLL is 76.8 kHz while having the sufficient phase margin of  $\sim 60^\circ$ , which enables the stable FLL. To realize the high-density multiplexing with the limited amount of system resource in satellites, the data rate needs to be greatly reduced without deteriorating the required SNR. In order to do that, waveforms are first triggered and extracted in the high sampling-rate at  $\sim 4$  MHz, and then aligned and down-sampled to 240 ksps. With this method, the required data amount for a 2-ms waveform is reduced to only 1 kB, keeping the required system data transfer rate to a practical number even for thousands of signal multiplexing.

To bridge the low-power SQUID and the digital FLL electronics, the analog front-end is also developed. It mainly consists of the low-noise amp to amplify the SQUID output, and the V/I converters to convert the voltage outputs of two DACs to the TES bias current and the feedback current keeping the high output impedance. The low-noise amp has the sufficient gain, 46 dB (40 dB when 50  $\Omega$ -terminated), and the low noise characteristic,  $< 2$  nV/ $\sqrt{\text{Hz}}$  @ 10 kHz. The V/I converter has the wide signal bandwidth of  $\sim 20$  MHz, while the current noise when multiplexing 16 channels is 22 nV/ $\sqrt{\text{Hz}}$ , which may need to be reduced further.

Finally, we performed the TES readout experiment to demonstrate the developed readout system, and successfully multiplexed four TES for the first time. Although the energy resolution suffered from the two new issues,

the excess noise and the crosstalk, the contribution of the developed readout system to the energy resolution is  $< 2$  eV FWHM @ 5.9 keV for 4-channel multiplexing, which satisfies the DIOS requirement to realize not only the 4-channel multiplexing but also the 8- to 16-channel multiplexing with the energy resolution 2 eV FWHM @ 2 keV. This demonstrates the feasibility of the large-format TES arrays with 256 to 400 pixels for the DIOS missions, as well as the possibility of the extra-large-format over-thousand-pixel TES arrays for future X-ray space missions.

A

# CRAVITY

## A.1 AIST Nb Standard Process (STD3)

All the SQUIDS we developed were fabricated in the Clean Room for Analog & Digital superconductiVITY (CRAVITY) at National Institute of Advanced Industrial Science and Technology (AIST), in accordance with the SRL Nb Standard Process (STD3). Figure A.1 shows the device structure of STD3. There are four conductive layers, GP, BAS, COU and CTL, but we only used three layers except GP. Table A.1 shows the detailed layer structure of STD3. The AU layer and the PL layer are optional. We used AU pads. The resistor layer uses molybdenum in standard, however, it can not be used below 1 K. We therefore used palladium-gold (Pd/Au) for the resistor layer.

The standard design rule in the STD3 follows:

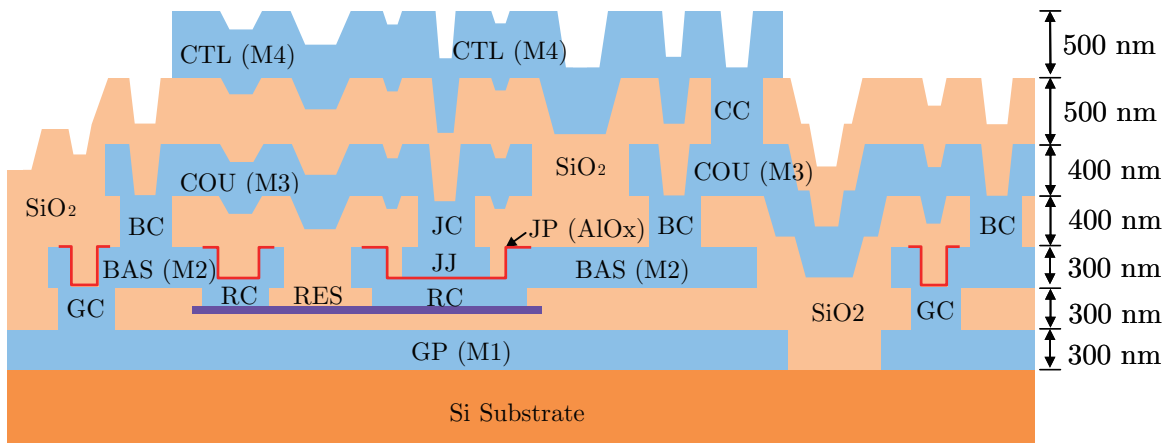


Fig. A.1 The device structure of SRL Nb Standard Process (STD3) [23]

Table A.1 The layer structure of SRL Nb Standard Process (STD3) [23]

Layer	Function	Material	Thickness (nm)
GP	Ground	Nb	300
	Insulating layer	SiO <sub>2</sub>	150
RES	Resistor	Mo	35
	Insulating layout	SiO <sub>2</sub>	150
RC	Contact between RES and BAS		
GC	Contact between GP and BAS		
BAS	Conductive layer	Nb	300
JP	JJ protection	Al, AlO <sub>x</sub>	
JJ	Josephson junction	Nb	150
	JJ protection (anodic oxidation)	Nb <sub>2</sub> O <sub>5</sub>	(20)
	Insulating layout	SiO <sub>2</sub>	400
BC	Contact between BAS and COU		
JC	Contact between JJ and COU		
COU	Conductive layer	Nb	400
	Insulating layout	SiO <sub>2</sub>	500
CC	Contact between COU and CTL		
CTL	Conductive layer	Nb	500
AU	Pad (sputtering)	Au	300
PL	Pad (plating)	Au	3000

- Minimum line width  $1.5 \mu\text{m}$
- Minimum spacing  $1.0 \mu\text{m}$
- Minimum junction size  $1.1 \mu\text{m}$  ( $1.0 \mu\text{m}$  after shrink)
- Shrink size of junctions  $0.1 \mu\text{m}$  ( $< 0.3 \mu\text{m}$  for junctions less than  $1.0 \mu\text{m}^2$ )
- Critical current density of junctions  $10 \text{ kA}/\text{cm}^2$
- Sheet resistance for RES  $2.4 \Omega$
- Minimum contact size  $1.0 \mu\text{m}$  ( $0.7 \mu\text{m}$  for JC)
- Alignment margin  $0.5 \mu\text{m}$  ( $0.25 \mu\text{m}$  for some layers)
- Shrink size for BAS  $0.2 \mu\text{m}$
- Shrink size for COU and CTL 0
- Shrink size for RES 0

The critical current density of junctions in standard,  $10 \text{ kA}/\text{cm}^2$ , is too large for our SQUIDS, so we used  $1 \text{ kA}/\text{cm}^2$ .

Finally, alignment margins, minimum spacing between layers, minimum line width in the STD3 are summarized from Table A.2 to Table A.4, respectively.

Table A.2 STD3 alignment margins (unit: $\mu\text{m}$ ) [23]

	GP	RES	GC	RC	JJ	JP	BAS	JC	BC	COU	CC	CTL
GP	...	×	×	×	×	×	×	×				
RES	×	...	×	0.50	1.00							
GC	×	×	...	×	×	0.25	0.50	×				
RC	×	0.50	×	...	0.50	0.25	0.50					
JJ	×	1.00	×	0.50	...	0.50		0.25				
JP	×		0.25	0.25	0.50	...						
BAS	×		0.50	0.50			...		0.50			
JC	×		×		0.25			...	×	0.50		
BC							0.50	×	...	0.50		
COU								0.50	0.50	...	0.50	
CC										0.50	...	0.50
CTL											0.50	...

×: No overlap.

Table A.3 STD3 minimum spacing between layers (unit: $\mu\text{m}$ ) [23]

	GP	RES	GC	RC	JJ	JP	BAS	JC	BC	COU	CC	CTL
GP	1.0	1.0			1.0		0.45					
RES	1.0	1.0	1.0									
GC		1.0	1.0		1.0							
RC				1.0								
JJ	1.0		1.0		1.0							
JP						1.0						
BAS	0.45						1.0					
JC								1.0				
BC									1.0			
COU										1.0		
CC											1.0	
CTL												1.0

Table A.4 STD3 minimum line width (unit: $\mu\text{m}$ ) [23]

	GP	RES	GC	RC	JJ	JP	BAS	JC	BC	COU	CC	CTL
Minimum width	1.0	1.5	1.0	1.0	1.1	1.5	1.5	0.7	1.0	1.5	1.0	1.5



B

## Hardware Registers and Addresses for Digital Electronics

Address	Hex	Register Name	Signal Name	R/W	Data	Description
7	00	Version	Signature	RO	31 * * * * *	0xBFB
6	00		Revision	RO	30 * * * * *	Unsigned
5	00		Number of Channels	RO	29 * * * * *	Unsigned
4	00		Reset	WO	28 * * * * *	1: Reset
3	00	Device Ch1	RO Enabled	RW	27 * * * * *	0: Disabled 1: Enabled
2	00		Loopback	RW	26 * * * * *	0: Disabled 1: Enabled
1	00		No Output Scaling	RW	25 * * * * *	0: Disabled 1: Enabled
0	00		Output Scaler (1:0)	RW	24 * * * * *	0: 2 1: 4 2: 8 3: 16
			Record Length (1:0)	RW	23 * * * * *	0: 256 1: 512 2: 1024 3: 2048
			Trigger Delay (7:0)	RW	22 * * * * *	Unsigned
			Mod Write Ch (3:0)	RW	21 * * * * *	Unsigned
			Reserved		20 * * * * *	
08	00	Device Stats	Reserved	RO	19 * * * * *	Unsigned
			FIFO Counts	RO	18 * * * * *	Unsigned / Big-endian
00	01	Data FIFO	Data	RO	17 * * * * *	Unsigned / Big-endian
00	10	Modulation Data	Data	RW	16 * * * * *	Unsigned
00	11	Reserved	Previous Trigger (15:0)	RW	15 * * * * *	Unsigned
00	14	Reserved	Next Trigger (15:0)	RW	14 * * * * *	Unsigned
00	18	Trigger Threshold			13 * * * * *	
00	19				12 * * * * *	
00	1A				11 * * * * *	
00	1B				10 * * * * *	
00	1C	Reserved			9 * * * * *	
00	1D				8 * * * * *	
00	1E				7 * * * * *	
00	1F				6 * * * * *	
00	20				5 * * * * *	
00	21				4 * * * * *	
00	22				3 * * * * *	
00	23				2 * * * * *	
00	24				1 * * * * *	
00	25				0 * * * * *	
00	26					
00	27					
00	28					
00	29					
00	2A					
00	2B					
00	2C					
00	2D					
00	2E					
00	2F					
00	30					
00	31					
00	32					
00	33					
00	34					
00	35					
00	36					
00	37					
00	38					
00	39					
00	3A					
00	3B					
00	3C					
00	3D					
00	3E					
00	3F					
00	40	Channel Stats (Ch 1)	Idle	RO	31 * * * * *	0: Idle 1: Running
			Reserved	RO	30 * * * * *	
			Triggered Count	RO	29 * * * * *	Unsigned
00	41				28 * * * * *	
00	42				27 * * * * *	
00	43				26 * * * * *	
00	44	Channel Stats (Ch 2)			25 * * * * *	
00	45				24 * * * * *	
00	46				23 * * * * *	
00	47				22 * * * * *	
00	48	Channel Stats (Ch 3)			21 * * * * *	
00	49				20 * * * * *	
00	4A	Channel Stats (Ch 4)			19 * * * * *	
00	4B				18 * * * * *	
00	4C	Channel Stats (Ch 5)			17 * * * * *	
00	4D				16 * * * * *	
00	4E	Channel Stats (Ch 6)			15 * * * * *	
00	4F				14 * * * * *	
00	50	Channel Stats (Ch 7)			13 * * * * *	
00	51				12 * * * * *	
00	52	Channel Stats (Ch 8)			11 * * * * *	
00	53				10 * * * * *	
00	54	Channel Stats (Ch 9)			9 * * * * *	
00	55				8 * * * * *	
00	56	Channel Stats (Ch 10)			7 * * * * *	
00	57				6 * * * * *	
00	58	Channel Stats (Ch 11)			5 * * * * *	
00	59				4 * * * * *	
00	5A	Channel Stats (Ch 12)			3 * * * * *	
00	5B				2 * * * * *	
00	5C	Channel Stats (Ch 13)			1 * * * * *	
00	5D				0 * * * * *	
00	5E	Channel Stats (Ch 14)				
00	5F					
00	60	Channel Stats (Ch 15)				
00	61					
00	62	Channel Stats (Ch 16)				
00	63					
00	64					
00	65					
00	66					
00	67					
00	68					
00	69					
00	6A					
00	6B					
00	6C					
00	6D					
00	6E					
00	6F					
00	70					
00	71					
00	72					
00	73					
00	74					
00	75					
00	76					
00	77					
00	78					
00	79					
00	7A					
00	7B					
00	7C					

Fig. B.1 The hardware registers and addresses for configuration parameters of the digital electronics (part 1 of 2)

Address				Register Name	Signal Name	R/W	Data																Description																							
7	6	5	4	3	2	1	0	Hex				31	30	29	28	27	26	25	24	23	22	21	20	19	18	17	16	15	14	13	12	11	10	9	8	7	6	5	4	3	2	1	0			
1	0	0	0	0	0	0	-	80	Channel Ctrl (Ch 1)	Enable	RW	*																																		0: Disabled 1: Enabled
										Clear	RW																																			0: Ready 1: Clear
										Feedback En	RW																																			0: Disabled 1: Enabled
										Integrator En	RW																																			0: Disabled 1: Enabled
										Trigger Level/Count Sel	RW																																			0: Level 1: Count
										Frequency/Phase Sel	RW																																			0: Frequency 1: Phase
										Baseband Gain (1:0)	RW																																			Unsigned
										Modulation En	RW																																			0: Disabled 1: Enabled
										Reserved	RW																																		Reserved	
										Derivation Mode (1:0)	RW																																		See Trigger Mode	
										Trigger Mode (3:0)	RW																																		See Trigger Mode	
										Reverse	RW																																		0: Disabled 1: Enabled	
										Gain (2:0)	RW																																		Signed (-4 to +3)	
										Amplitude (11:0)	RW																																		Unsigned (0 to 4095)	
1	0	0	0	0	0	1	-	B4		Frequency/Phase (15:0)	RW	*																																	Unsigned	
										Trigger Level/Count (15:0)	RW																																			Unsigned
1	0	0	0	1	0	-	-	88	Channel Ctrl (Ch 2)																																					
1	0	0	0	1	1	-	-	8C	Channel Ctrl (Ch 3)																																					
1	0	0	0	1	0	-	-	90	Channel Ctrl (Ch 3)																																					
1	0	0	0	1	0	1	-	94	Channel Ctrl (Ch 4)																																					
1	0	0	0	1	0	1	-	98	Channel Ctrl (Ch 4)																																					
1	0	0	0	1	1	-	-	9C	Channel Ctrl (Ch 5)																																					
1	0	0	0	1	0	0	-	A0	Channel Ctrl (Ch 5)																																					
1	0	0	0	1	0	1	-	A4	Channel Ctrl (Ch 6)																																					
1	0	0	0	1	0	1	-	A8	Channel Ctrl (Ch 6)																																					
1	0	0	0	1	1	-	-	AC	Channel Ctrl (Ch 7)																																					
1	0	0	0	1	0	0	-	B0	Channel Ctrl (Ch 7)																																					
1	0	0	0	1	0	1	-	B4	Channel Ctrl (Ch 8)																																					
1	0	0	0	1	1	1	-	B8	Channel Ctrl (Ch 8)																																					
1	0	0	0	1	1	1	-	BC	Channel Ctrl (Ch 9)																																					
1	0	0	0	1	0	0	-	C0	Channel Ctrl (Ch 9)																																					
1	0	0	0	1	0	1	-	C4	Channel Ctrl (Ch 10)																																					
1	0	0	0	1	0	0	-	C8	Channel Ctrl (Ch 10)																																					
1	0	0	0	1	0	1	-	CC	Channel Ctrl (Ch 11)																																					
1	0	0	0	1	0	0	-	D0	Channel Ctrl (Ch 11)																																					
1	0	0	0	1	0	1	-	D4	Channel Ctrl (Ch 12)																																					
1	0	0	0	1	0	1	-	D8	Channel Ctrl (Ch 12)																																					
1	0	0	0	1	1	1	-	DC	Channel Ctrl (Ch 13)																																					
1	0	0	0	1	1	0	-	E0	Channel Ctrl (Ch 13)																																					
1	0	0	0	1	1	0	1	-	E4	Channel Ctrl (Ch 14)																																				
1	0	0	0	1	1	1	-	EC	Channel Ctrl (Ch 14)																																					
1	0	0	0	1	1	0	1	-	EC	Channel Ctrl (Ch 14)																																				
1	0	0	0	1	1	1	0	-	F0	Channel Ctrl (Ch 15)																																				
1	0	0	0	1	1	0	1	-	F4	Channel Ctrl (Ch 15)																																				
1	0	0	0	1	1	1	0	-	F8	Channel Ctrl (Ch 16)																																				
1	0	0	0	1	1	1	1	-	FC	Channel Ctrl (Ch 16)																																				

Fig. B.2 The hardware registers and addresses for configuration parameters of the digital electronics (part 2 of 2)



C

Design of Analog Front-End

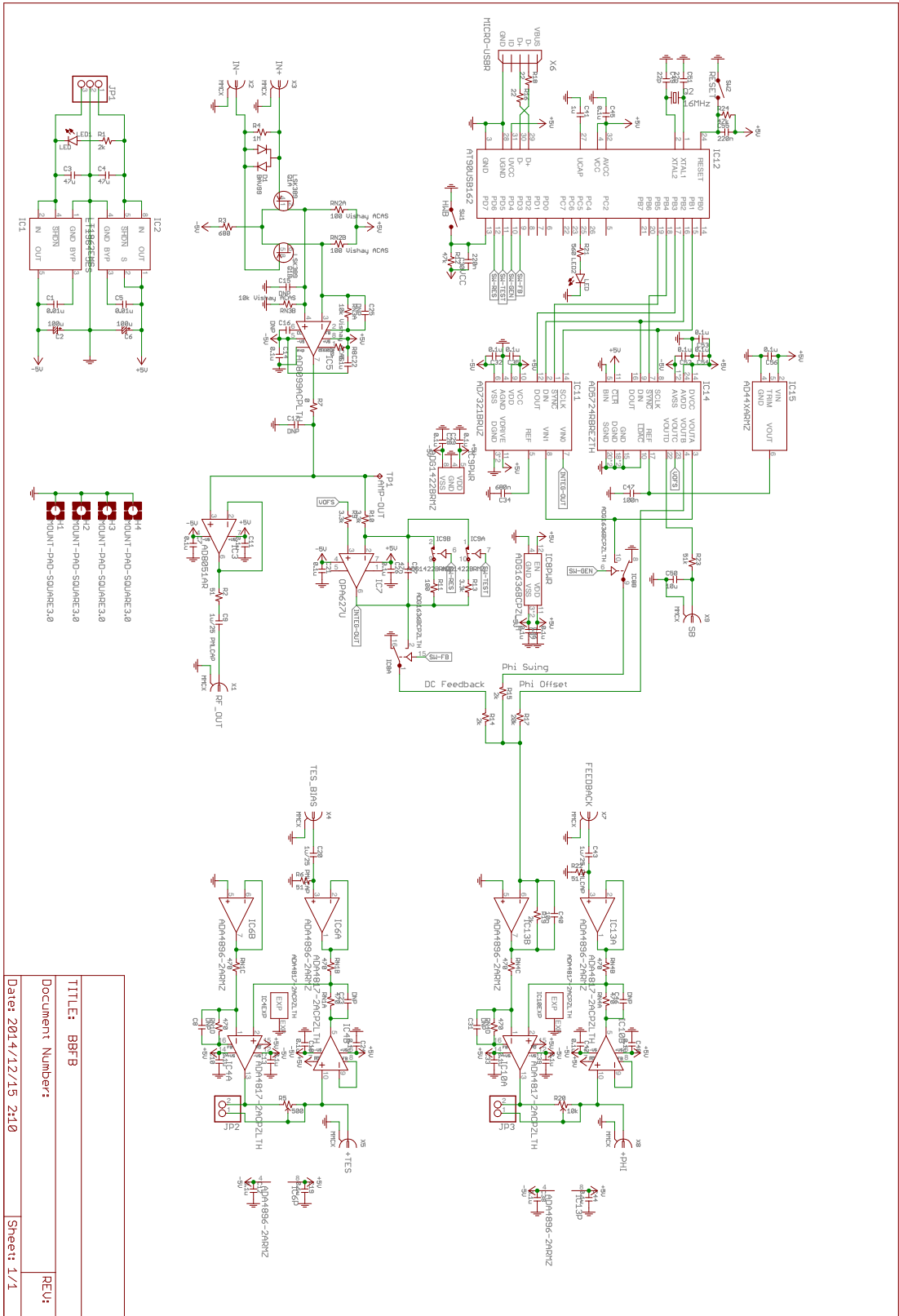


Fig. C.1 The circuit schematic of BBFB analog front-end

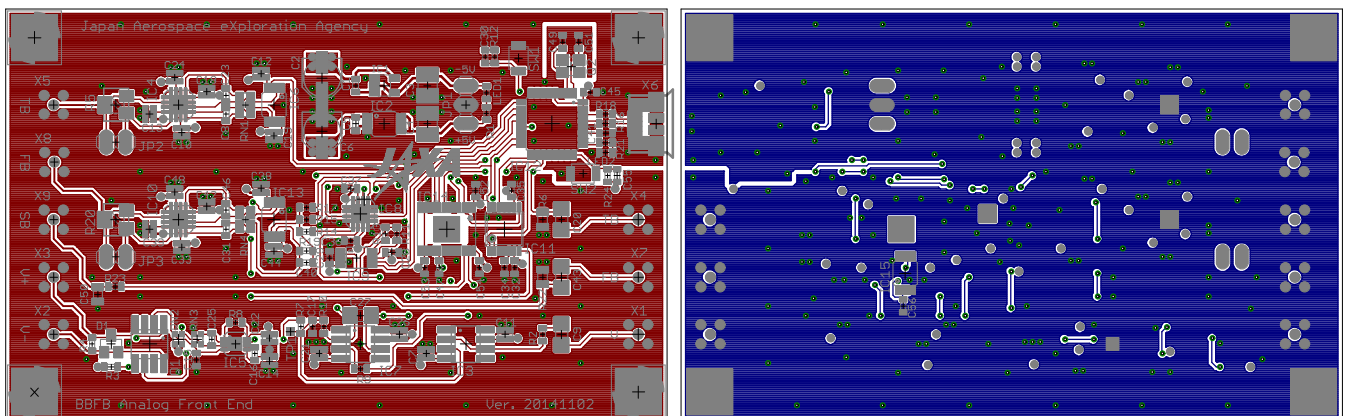


Fig. C.2 Full-scale PCB layouts of BBFB analog front-end: the component side (left) and the solder side (right)



# Bibliography

- [1] H. Akamatsu, Y. Abe, K. Ishikawa, Y. Ishisaki, Y. Ezoe, T. Ohashi, Y. Takei, N Y Yamasaki, K Mitsuda, and R. Maeda. Impedance measurement and excess-noise behavior of a Ti/Au bilayer TES calorimeter. In *THE THIRTEENTH INTERNATIONAL WORKSHOP ON LOW TEMPERATURE DETECTORS-LTD13. AIP Conference Proceedings*, pages 195–198. Department of Physics, Tokyo Metropolitan University, 1-1 Minami-Osawa, Hachioji, Tokyo 192-0397, Japan, December 2009.
- [2] Joel N Bregman. The Search for the Missing Baryons at Low Redshift. *Annual Review of Astronomy & Astrophysics*, 45(1):221–259, September 2007.
- [3] Renyue Cen and Jeremiah P Ostriker. Where Are the Baryons? *The Astrophysical Journal*, 514(1):1–6, March 1999.
- [4] J Clarke. Advances in SQUID magnetometers. *Electron Devices, IEEE Transactions on*, 27(10):1896–1908, 1980.
- [5] J Clarke. Principles and applications of SQUIDS. *Proceedings of the IEEE*, 77(8):1208–1223, 1989.
- [6] John Clarke and Alex I. Braginski, editors. *The SQUID Handbook: Fundamentals and Technology of SQUIDS and SQUID Systems*. Wiley-VCH, 1 edition, August 2004.
- [7] M F Cunningham, J N Ullom, T Miyazaki, S E Labov, John Clarke, T M Lanting, Adrian T Lee, P L Richards, Jongsoo Yoon, and H Spieler. High-resolution operation of frequency-multiplexed transition-edge photon sensors. *Applied Physics Letters*, 81(1):159–161, July 2002.
- [8] M. Dobbs, F. Aubin, T. de Haan, S. Hanany, N. Harrington, W. Holzapfel, J. Hubmayr, A. Lee, M. Lueker, K. Macdermid, and G. Smecher. Digital Frequency Multiplexer for TES Detectors—Path to Flight. *Journal of Low Temperature Physics*, 167(5):568–574, June 2012.
- [9] K Enpuku, H Doi, G Tokita, and T Maruo. Method for improving voltage modulation depth of high Tc DC SQUID with large inductance. *Applied Superconductivity, IEEE Transactions on*, 5(2):2762–2765, 1995.
- [10] K Enpuku, G Tokita, T Maruo, and T Minotani. Parameter dependencies of characteristics of a high-Tc dc superconducting quantum interference device. *Journal of Applied Physics*, 78(5):3498–3503, September 1995.
- [11] J W Fowler, W B Doriese, G Hilton, K Irwin, D Schmidt, G Stiehl, D Swetz, J N Ullom, and L Vale. Optimization and Analysis of Code-Division Multiplexed TES Microcalorimeters. *Journal of Low Temperature Physics*, 167(5):713–720, June 2012.
- [12] T Hara, K Tanaka, K Maehata, K Mitsuda, N Y Yamasaki, M Ohsaki, K Watanabe, X Yu, T Ito, and Y Yamanaka. Microcalorimeter-type energy dispersive X-ray spectrometer for a transmission electron microscope. *Journal of Electron Microscopy*, 59(1):17–26, February 2010.
- [13] Kaori Hattori, Kam Arnold, Darcy Barron, Matt Dobbs, Tijmen de Haan, Nicholas Harrington, Masaya Hasegawa, Masashi Hazumi, William L Holzapfel, Brian Keating, Adrian T Lee, Hideki Morii, Michael J Myers, Graeme Smecher, Aritoki Suzuki, and Takayuki Tomaru. Adaptation of frequency-domain readout for Transition Edge Sensor bolometers for the POLARBEAR-2 Cosmic Microwave Background experiment. *Nuclear Instruments and Methods in Physics Research Section A: Accelerators, Spectrometers, Detectors and Associated Equipment*, 732:299–302, December 2013.

- [14] R A Hijmering, R H den Hartog, A J van der Linden, M Ridder, M P Bruijn, J van der Kuur, B J van Leeuwen, P van Winden, and B Jackson. The 160 TES bolometer read-out using FDM for SAFARI. In Wayne S Holland and Jonas Zmuidzinas, editors, *Proceedings of the SPIE*, pages 91531E–91531E–12. Netherlands Institute for Space Research (Netherlands), SPIE, July 2014.
- [15] E Hogenauer. An economical class of digital filters for decimation and interpolation. *IEEE Transactions on Acoustics, Speech, and Signal Processing*, 29(2):155–162, April 1981.
- [16] K. D. Irwin and G. C. Hilton. Transition-Edge Sensors. *Cryogenic Particle Detection*, 9:63, 2005.
- [17] Kent D. Irwin. *Phonon-mediated particle detection using superconducting tungsten transition-edge sensors*. PhD thesis, Stanford University, 1995.
- [18] Kent D Irwin, Michael D Audley, James A Beall, Jörn Beyer, Steve Deiker, William Doriese, William Duncan, Gene C Hilton, Wayne Holland, Carl D Reintsema, Joel N Ullom, Leila R Vale, and Yizi Xu. In-focal-plane SQUID multiplexer. *Nuclear Instruments and Methods in Physics Research Section A: Accelerators, Spectrometers, Detectors and Associated Equipment*, 520(1-3):544–547, March 2004.
- [19] J Jaycox and M Ketchen. Planar coupling scheme for ultra low noise DC SQUIDS. *Magnetics, IEEE Transactions on*, 17(1):400–403, 1981.
- [20] K Maehata, T Hara, T Ito, Y Yamanaka, K Tanaka, K Mitsuda, and N Y Yamasaki. A dry  $^3\text{He}$ - $^4\text{He}$  dilution refrigerator for a transition edge sensor microcalorimeter spectrometer system mounted on a transmission electron microscope. *Cryogenics*, 61:86–91, May 2014.
- [21] John C. Mather. Bolometer noise: nonequilibrium theory. *Applied Optics*, 21(6):1125–1129, March 1982.
- [22] S H Moseley, J. C. Mather, and D McCammon. Thermal detectors as x-ray spectrometers. *Journal of Applied Physics*, 56(5):1257–1262, September 1984.
- [23] Shuichi Nagasawa. SRL 10kA/cm<sup>2</sup> Nb 標準プロセス (STD3) の設計仕様, February 2010.
- [24] Kirpal Nandra, Didier Barret, Xavier Barcons, Andy Fabian, Jan Willem den Herder, Luigi Piro, Mike Watson, Christophe Adami, James Aird, Jose Manuel Afonso, Dave Alexander, Costanza Argiroffi, Lorenzo Amati, Monique Arnaud, Jean-Luc Atteia, Marc Audard, Carles Badenes, Jean Ballet, Lucia Ballo, Aya Bamba, Anil Bhardwaj, Elia Stefano Battistelli, Werner Becker, Michaël De Becker, Ehud Behar, Stefano Bianchi, Veronica Biffi, Laura Birzan, Fabrizio Bocchino, Slavko Bogdanov, Laurence Boirin, Thomas Boller, Stefano Borgani, Katharina Borm, Nicolas Bouché, Hervé Bourdin, Richard Bower, Valentina Braitto, Enzo Branchini, Graziella Branduardi-Raymont, Joel Bregman, Laura Brenneman, Murray Brightman, Marcus Brüggem, Johannes Buchner, Esra Bulbul, Marcella Brusa, Michal Bursa, Alessandro Caccianiga, Ed Cackett, Sergio Campana, Nico Cappelluti, Massimo Cappi, Francisco Carrera, Maite Ceballos, Finn Christensen, You-Hua Chu, Eugene Churazov, Nicolas Clerc, Stephane Corbel, Amalia Corral, Andrea Comastri, Elisa Costantini, Judith Croston, Mauro Dadina, Antonino D’Ai, Anne Decourchelle, Roberto Della Ceca, Konrad Dennerl, Klaus Dolag, Chris Done, Michal Dovciak, Jeremy Drake, Dominique Eckert, Alastair Edge, Stefano Etti, Yuichiro Ezoe, Eric Feigelson, Rob Fender, Chiara Feruglio, Alexis Finoguenov, Fabrizio Fiore, Massimiliano Galeazzi, Sarah Gallagher, Poshak Gandhi, Massimo Gaspari, Fabio Gastaldello, Antonis Georgakakis, Ioannis Georgantopoulos, Marat Gilfanov, Myriam Gitti, Randy Gladstone, Rene Goosmann, Eric Gosset, Nicolas Grosso, Manuel Guedel, Martin Guerrero, Frank Haberl, Martin Hardcastle, Sebastian Heinz, Almudena Alonso Herrero, Anthony Hervé, Mats Holmstrom, Kazushi Iwasawa, Peter Jonker, Jelle Kaastra, Erin Kara, Vladimir Karas, Joel Kastner, Andrew King, Daria Kosenko, Dimita Koutroumpa, Ralph Kraft, Ingo Kreykenbohm, Rosine Lallement, Giorgio Lanzuisi, J Lee, Marianne Lemoine-Goumard, Andrew Lobban, Giuseppe Lodato, Lorenzo Lovisari, Simone Lotti, Ian McCharthy, Brian McNamara, Antonio Maggio, Roberto Maiolino, Barbara De Marco, Domitilla de Martino, Silvia Mateos, Giorgio Matt, Ben Maughan, Pasquale Mazzotta, Mariano Mendez, Andrea Merloni, Giuseppina Micela, Marco Miceli, Robert Mignani, Jon Miller, Giovanni Miniutti, Silvano Molendi, Rodolfo Montez, Alberto Moretti, Christian Motch, Yaël

- Nazé, Jukka Nevalainen, Fabrizio Nicastro, Paul Nulsen, Takaya Ohashi, Paul O'Brien, Julian Osborne, Lida Oskinova, Florian Pacaud, Frederik Paerels, Mat Page, Iossif Papadakis, Giovanni Pareschi, Robert Petre, Pierre-Olivier Petrucci, Enrico Piconcelli, Ignazio Pillitteri, C Pinto, Jelle de Plaa, Etienne Pointecouteau, Trevor Ponman, Gabriele Ponti, Delphine Porquet, Ken Pounds, Gabriel Pratt, Peter Predehl, Daniel Proga, Dimitrios Psaltis, David Rafferty, Miriam Ramos-Ceja, Piero Ranalli, Elena Rasia, Arne Rau, Gregor Rauw, Nanda Rea, Andy Read, James Reeves, Thomas Reiprich, Matthieu Renaud, Chris Reynolds, Guido Risaliti, Jerome Rodriguez, Paola Rodriguez Hidalgo, Mauro Roncarelli, David Rosario, Mariachiara Rossetti, Agata Rozanska, Emmanouil Rovilos, Ruben Salvaterra, Mara Salvato, Tiziana Di Salvo, Jeremy Sanders, Jorge Sanz-Forcada, Kevin Schawinski, Joop Schaye, Axel Schwobe, Salvatore Sciortino, Paola Severgnini, Francesco Shankar, Debora Sijacki, Stuart Sim, Christian Schmid, Randall Smith, Andrew Steiner, Beate Stelzer, Gordon Stewart, Tod Strohmayer, Lothar Strüder, Ming Sun, Yoh Takei, V Tatischeff, Andreas Tiengo, Francesco Tombesi, Ginevra Trinchieri, T G Tsuru, Asif Ud-Doula, Eugenio Ursino, Lynne Valencic, Eros Vanzella, Simon Vaughan, Cristian Vignali, Jacco Vink, Fabio Vito, Marta Volonteri, Daniel Wang, Natalie Webb, Richard Willingale, Joern Wilms, Michael Wise, Diana Worrall, Andrew Young, and Za... The Hot and Energetic Universe: A White Paper presenting the science theme motivating the Athena+ mission. *arXiv.org*, page 2307, June 2013.
- [25] T. Ohashi, Y. Ishisaki, Y. Ezoe, S. Sasaki, H. Kawahara, K Mitsuda, N Y Yamasaki, Y. Takei, M. Ishida, Y. Tawara, I. Sakurai, A. Furuzawa, Y. Suto, K. Yoshikawa, N. Kawai, R. Fujimoto, T. G. Tsuru, K. Matsushita, and T. Kitayama. DIOS: the diffuse intergalactic oxygen surveyor: status and prospects. *Space Telescopes and Instrumentation 2010: Ultraviolet to Gamma Ray*, edited by Monique Arnaud, Stephen S. Murray, Tadayuki Takahashi, *Proc. of SPIE*, 7732:54, July 2010.
- [26] Laurent Ravera, Didier Barret, Jan Willem den Herder, Luigi Piro, Rodolphe Clédassou, Etienne Pointecouteau, Philippe Peille, Francois Pajot, Monique Arnaud, Claude Pigot, Lionel Duband, Christophe Cara, Roland H den Hartog, Luciano Gottardi, Hiroki Akamatsu, Jan van der Kuur, Henk J van Weers, Jelle de Plaa, Claudia Macculi, Simone Lotti, Guido Torrioli, Flavio Gatti, Luca Valenziano, Marco Barbera, Xavier Barcons, María Teresa Ceballos, Lourdes Fàbrega, José Miguel Mas-Hesse, Mathew J Page, Phillip R Guttridge, Richard Willingale, Stéphane Paltani, Ludovic Genolet, Enrico Bozzo, Gregor Rauw, Etienne Renotte, Jörn Wilms, and Christian Schmid. The X-ray Integral Field Unit (X-IFU) for Athena. In Tadayuki Takahashi, Jan-Willem A den Herder, and Mark Bautz, editors, *Proceedings of the SPIE*, pages 91442L–91442L–13. Observatoire Midi-Pyrénées, IRAP, CNRS, Univ. de Toulouse (France), SPIE, July 2014.
- [27] Laurent Ravera, Christophe Cara, María Teresa Ceballos, Xavier Barcons, Didier Barret, Rodolphe Clédassou, Antoine Clénet, Beatriz Cobo, Eric Doumayrou, Roland H den Hartog, Bert-Joost van Leeuwen, Dennis van Loon, José Miguel Mas-Hesse, Claude Pigot, and Etienne Pointecouteau. The DRE: the digital readout electronics for ATHENA X-IFU. In Tadayuki Takahashi, Jan-Willem A den Herder, and Mark Bautz, editors, *Proceedings of the SPIE*, pages 91445T–91445T–8. Observatoire Midi-Pyrénées, IRAP, CNRS, Univ. de Toulouse (France), SPIE, July 2014.
- [28] Tapani Ryhänen, Heikki Seppä, Risto Ilmoniemi, and Jukka Knuutila. SQUID magnetometers for low-frequency applications. *Journal of Low Temperature Physics*, 76(5):287–386, September 1989.
- [29] K Sakai, Y Takei, R Yamamoto, N Y Yamasaki, K Mitsuda, M Hidaka, S Nagasawa, S Kohjiro, and T Miyazaki. Baseband Feedback Frequency-Division Multiplexing with Low-Power dc-SQUIDS and Digital Electronics for TES X-Ray Microcalorimeters. *Journal of Low Temperature Physics*, 176(3-4):400–407, January 2014.
- [30] J Michael Shull, Britton D Smith, and Charles W Danforth. The Baryon Census in a Multiphase Intergalactic Medium: 30Baryons May Still be Missing. *The Astrophysical Journal*, 759(1):23, November 2012.

- [31] Y. Takei, N Y Yamasaki, W. Hirakoso, S Kimura, and K Mitsuda. SQUID multiplexing using baseband feedback for space application of transition-edge sensor microcalorimeters. *Superconductor Science & Technology*, 22(1):4008, November 2009.
- [32] Claudia D. Tesche and John Clarke. dc SQUID: Noise and optimization. *Journal of Low Temperature Physics*, 29(3):301–331, November 1977.
- [33] J van der Kuur, J Beyer, D Boersma, M Bruin, L Gottardi, R den Hartog, H Hoevers, R Hou, M Kiviranta, P J de Korte, and B J van Leeuwen. Progress on Frequency-Domain Multiplexing Development for High Count rate X-ray Microcalorimeters. In *THE THIRTEENTH INTERNATIONAL WORKSHOP ON LOW TEMPERATURE DETECTORS-LTD13. AIP Conference Proceedings*, pages 245–248. SRON Netherlands Institute for Space Research, Sorbonnelaan 2, Utrecht 3584 CA, the Netherlands, AIP, December 2009.
- [34] H Weinstock, editor. *SQUID Sensors: Fundamentals, Fabrication and Applications (NATO Science Series E: Applied Sciences)*, volume 329. Springer, 1 edition, November 1996.
- [35] R Yamamoto, K Sakai, Y Takei, N Y Yamasaki, and K Mitsuda. Performance of Frequency Division Multiplexing Readout System for AC-Biased Transition-Edge Sensor X-ray Microcalorimeters. *Journal of Low Temperature Physics*, 176(3):453–458, August 2014.
- [36] Y Yamanaka, T Ito, T Umeno, Y Suzuki, S Yoshida, Y Kamioka, and K Maehata. Development of GM cryocooler separate type liquid-helium-free  $^3\text{He}$ - $^4\text{He}$  dilution refrigerator system. *Journal of Physics: Conference Series*, 150(1):012055, February 2009.
- [37] Kohji Yoshikawa, Klaus Dolag, Yasushi Suto, Shin Sasaki, Noriko Y Yamasaki, Takaya Ohashi, Kazuhisa Mitsuda, Yuzuru Tawara, Ryuichi Fujimoto, Tae Furusho, Akihiro Furuzawa, Manabu Ishida, Yoshitaka Ishisaki, and Yoh Takei. Locating the Warm–Hot Intergalactic Medium in the Simulated Local Universe. *Publications of the Astronomical Society of Japan*, 56:939–957, December 2004.